A NOVEL PROCESS FOR GeSi THIN FILM SYNTHESIS

Khalid Hossain, B.Sc. Eng., M. Eng.

Dissertation Prepared for the Degree of

DOCTOR OF PHILOSOPHY

UNIVERSITY OF NORTH TEXAS

December 2007

APPROVED:

Floyd D. McDaniel, Major Professor and Chair
of the Department of Physics
Orin Wayne Holland, Committee Member
Jerome L. Duggan, Committee Member
Duncan L. Weathers, Committee Member and
Departmental Program Coordinator
Terry D. Golding, Committee Member
Sandra L. Terrell, Dean of the Robert B.
Toulouse School of Graduate Studies

Hossain, Khalid. *A Novel Process for GeSi Thin Film Synthesis*, Doctor of Philosophy (Physics), December 2007, 118 pp, 71 figures, 3 tables, chapter references.

A unique process of fabricating a strained layer Ge_xSi_{1-x} on insulator is demonstrated. Such strained heterostructures are useful in the fabrication of high-mobility transistors. This technique incorporates well-established silicon processing technology e.g., ion implantation and thermal oxidation. A dilute GeSi layer is initially formed by implanting Ge^+ into a silicon-on-insulator (SOI) substrate. Thermal oxidation segregates the Ge at the growing oxide interface to form a distinct Ge_xSi_{1-x} thin-film with a composition that can be tailored by controlling the oxidation parameters (e.g. temperature and oxidation ambient). In addition, the film thickness can be controlled by implantation fluence, which is important since the film forms pseudomorphically below 2×10^{16} Ge/cm^2. Continued oxidation consumes the underlying Si leaving the strained GeSi film encapsulated by the two oxide layers, i.e. the top thermal oxide and the buried oxide. Removal of the thermal oxide by a dilute HF etch completes the process. Strain relaxation can be achieved by either of two methods. One involves vacancy injection by ion implantation to introduce sufficient open-volume within the film to compensate for the compressive strain. The other depends upon the formation of GeO_2. If Ge is oxidized in the absence of Si, it evaporates as GeO(g) resulting in spontaneous relaxation within the strained film. Conditions under which this occurs have been discussed along with elaborated results of oxidation kinetics of Ge-ion implanted silicon. Rutherford backscattering spectrometry (RBS), ion channeling, Raman spectroscopy and scanning electron microscopy (SEM) were used as the characterization techniques.

ACKNOWLEDGEMENT

In the name of God, I express my humbleness to the Almighty and gratitude for His blessings. Also, my heartfelt appreciation goes to the most important women in my life, my Mom and my Wife, whose continuous support helped me pursue and complete this work.

I am extremely thankful to Dr. Floyd Del McDaniel for accepting me as his graduate student and allowing me to be a part of the Ion Beam Modification and Analysis Laboratory (IBMAL) family, and guiding me during the course of this work.

Special thanks and gratitude goes to Dr. Jerome L. Duggan for his continuous guidance and encouragement. Without his mentoring and caring attitude, I could not have achieved my research goals.

My heartfelt appreciation goes to Dr. O. W. Holland, who is the mastermind behind this research. I am so lucky to have had such a good mentor to instruct me in ion beam materials modification and characterization techniques.

I wish to acknowledge Dr. D. L. Weathers, who made my graduate studentship easier by advising me in every aspects of my student life.

I wish to especially thank my committee, including Dr. T. D. Golding, for their kind and helpful comments. I also received tremendous help from my research group, which includes Dr. L. Mitchell, and Dr. F. Naab. Lastly, I acknowledge my appreciation for the help and encouragement from others graduate students including Eric Smith, Amir Mohammadizia, Venkata Kummari, Lucas Phinney, Mangal Dhaubadel, Prakash Poudel, Swayambhu Behera, Vali Ahmadi, and Nader Elmarhoumi.

I like to acknowledge Dr. Michael Santos and Dr. Tetsuya Mishima of the University of Oklahoma for their collaboration and assistance on microscopy.

I also wish to acknowledge the financial support of the Robert A. Welch Foundation, the National Science Foundation and Texas Instruments. Partial support is acknowledged for this work from Amethyst Research Inc. under contract no. W91NF-06-C-0074 with the Army Research Office.

TABLE OF CONTENTS

Page

LIST OF TABLES

Page

LIST OF FIGURES

Page

CHAPTER 1

INTRODUCTION

1.1 Introduction

It has been said that, "God gifted silicon to mankind but the Devil gave it an indirect band gap". A consequence of the "Devil's work" is that Si, the standard material for microelectronic fabrication, is unsuitable for optoelectronic applications since direct optical transitions of electronically excited states are forbidden. Although integrated circuits (ICs) are typically fabricated using a bulk Si wafer, high performance radio frequency (RF) devices, as well as optical detectors/sensors, require the use of optically-active materials, such as group III-V or II-VI semiconductors (e.g. GaAs and HgCdTe). Unfortunately, these materials differ from Si in both their lattice parameter and thermal properties, making monolithic integration of electro-optical functionality on Si problematic. While silicon-based heterostructures have been targeted as a means of providing such monolithic integration, the large lattice mismatch between the different materials makes it difficult to grow such heterostructures without compromising material quality and/or device performance. The use of a compliant substrate to accommodate the mismatch strain has been proposed to facilitate the integration of III-V's and/or II-VI's on a single Si-based platform. One promising method of forming a compliant template involves the use of a very thin-film GeSi on oxide. The use of a very thin film (< 5 nm), coupled with the viscoelastic property of vitreous oxide, can potentially provide the desired compliancy. In addition, pseudomorphic Si:$Si_{1-x}Ge_x$ (x = 0.1–0.2) heterostructures have been shown to exhibit very useful electrical properties such as a carrier mobility increasing with biaxial compressive-strain. Pseudomorphic growth, i.e., growth in which the lattice mismatched film adopts the

lattice parameter of the substrate, occurs over a certain thickness that depends upon the degree of mismatch, as will be discussed later. Strain energy increases with the thickness of the grown layer until, at a critical thickness, the buildup of strain energy leads to plastic deformation of the film.

There are different methods of forming a SiGe:Si heterostructure for use in either bandgap-engineering or materials integration. One method is chemical vapor deposition (CVD), which has been used to deposit a compositionally-graded SiGe film on silicon [Dohrman *et al.*, 2006] using an appropriate chemical mixture of SiH_4 and GeH_4 to achieve the desired SiGe concentration. Another deposition technique involves molecular beam epitaxy (MBE). However, the difference in the thermal expansion coefficient (TEC) between Si and Ge is a limiting factor in growing a Ge-rich virtual substrate on silicon by each of these techniques. Also, since the lattice constant of Ge is ~ 4.2 % larger than that of Si, the composition of SiGe must be varied gradually during growth on silicon substrate to avoid abrupt changes in the lattice constant and associated stress. The poor thermal conductivity of the resulting thick film may limit its use in high-power devices [Isaacson *et al.*, 2006].

Since both CVD and MBE involve epitaxial growth on a crystalline substrate, it is not possible to grow single-crystal SiGe directly on a vitreous insulator, as required to form the growth substrate. To overcome the difficulties there have been a number of attempts to form SiGe on insulator by techniques that do not involve growth. Separation-by-implanted-oxygen (SIMOX) is one of them. This method has long been used for making SOI wafers (a cross sectional illustration of which is given with Figure 1.1), and involves oxygen implantation on a silicon substrate followed by thermal annealing to form a buried oxide (BOX) layer below a silicon surface layer. A similar technique is used to make a SiGe:SiO_2 heterostructure (i.e.,

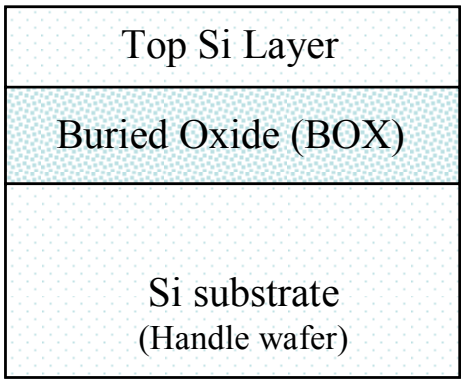

Fig. 1.1: Schematic illustration of the cross section of an SOI wafer.

SiGe-on-insulator (SGOI)) by implanting oxygen into a thick $Si_{1-x}Ge_x$ film grown on a Si substrate [Tang *et al.*, 1990 and Ishikawa *et al.*, 1999]. In both cases the Ge concentration in the SiGe alloy layer was low. Similarly, SiGe-SIMOX techniques of fabricating SGOI by Tang *et al.* [1990] and also by Fukatsu *et al.* [1998] are summarized as follows: a step-graded relaxed buffer layer of $Si_{1-x}Ge_x$ was grown with composition grading from $x = 0$ to $x = 0.18$. O^+-ions (ion energies of 25 keV and 200 keV were chosen by Fukatsu *et al.* [1998] and Tang *et al.* [1990] respectively) were then implanted with high doses (10^{17} to 10^{18} ions/cm^2). Since the 1250 °C annealing temperatures required forming a continuous buried oxide layer which is much larger than the melting point of Ge (~940 °C) the fabrication of SGOI by SIMOX cannot be used with a SiGe film with a Ge concentration more than 30%. Several research groups have adopted an alternate approach to overcome the limitation mentioned above. The basic idea involves Ge enrichment of the SiGe film by thermal oxidation for the formation of the SGOI structure [Tezuka *et al.*, 2001] or even GOI [Nakaharai *et al.*, 2003].

In the present work, a unique technique of fabricating SiGe-on-insulation (SGOI), as well as Ge-on-insulator (GOI), is investigated. This technique incorporates well-established silicon processing technology including ion implantation and thermal oxidation. Previously, it has been shown that Ge is totally rejected during thermal oxidation of Ge^+-implanted Si [Holland *et al.*, 1987 and Fathy *et al.*, 1987]. The rejection or segregation of Ge produces a 'snow-plow' effect that causes Ge to accumulate in front of the growing oxide interface to form a SiO_2:Ge_xSi_{1-x}:Si

heterostructure. The segregated GeSi layer has been shown to be distinct and epitaxially oriented on the underlying Si substrate. The composition of the Ge-rich layer is determined by the kinetic competition between the segregation effect during oxidation and interdiffusion of the Ge-rich layer with the underlying Si substrate, which are controlled by process parameters such as oxidation temperature and ambient. Furthermore, it has been demonstrated by Holland *et al.* [1987] that the oxidation kinetics are enhanced by Ge segregation under certain conditions, i.e., during wet (H_2O) rather than dry (O_2) oxidation.

A variation of the basic process described above is required to form a thin-film GeSi: SiO_2 heterostructure. In particular, an SOI rather than a bulk Si wafer must be used as the starting substrate. The process involves Ge-ion implantation of the superficial Si layer of an SOI wafer to form a dilute GeSi mixture. This GeSi layer is subsequently enriched by thermal oxidation, a reaction that consumes Si in the layer. Thermal oxidation is continued until the GeSi film is encapsulated by the thermal oxide on top and the BOX below. The thickness/composition of the encapsulated layer can be adjusted by appropriate oxidation conditions. Finally, the process is completed by chemical etching of the thermal oxide by a dilute HF solution to yield the desired structure, i.e., GeSi:BOX:Si. Details of this process are described in subsequent chapters, as well as the characterization of the various process steps including detailed morphological and microstructural analysis of the GeSi film.

In addition, a detailed investigation of the oxidation kinetics of Ge^+-implanted silicon is described in this thesis; this investigation was done to better understand the effect of Ge segregation on the oxidation behavior of Si. This phenomenon is interesting not only on its own merit, but also because it is a critical element in the Ge_xSi_{1-x} thin film fabrication process. The kinetics were determined under a variety of oxidation conditions including both wet and dry

ambient, as well as at different temperatures and implantation doses. The results of the kinetic data were utilized to properly control the composition and thickness of the segregated GeSi layer, which is necessary since the film remains pseudomorphic only below a critical thickness given approximately by the equilibrium value predicted by Matthews and Blakeslee [1974]. Compositional and morphological properties as well as the crystallinity of the Ge_xSi_{1-x} thin films grown in a silicon-on-insulator (SOI) wafer and in bulk Si have been investigated.

The thesis is organized as follows: first, the introduction of different properties of the SiGe alloy and SiGe:Si heterostructure and associated strain is given, followed by a description of the ion beam materials modification and characterization techniques used in the present work. Thereafter, the kinetic study of thermal oxidation, and the efforts towards synthesizing pseudomorphic and strain-relaxed Ge_xSi_{1-x} thin film are discussed. Some additional literature and characterization techniques are blended with the discussion.

1.2 References

Dohrman, C.L, Chilukuri, K., Isaacson, D. M, Lee, M.L., Fitzgerald, A., Mats. Sci. and Eng. B **135** (2006) 235

Fathy, D., Holland, O.W., White, C.W., Appl. Phys. Lett. **51** (1987) 1337

Fukatsu, S., Ishikawa, Y., Saito, T., Shibata, N., Appl. Phys. Lett. 72 (1998) 3485

Holland, O.W., White, C.W., Fathy, D., Appl. Phys. Lett. **57** (1987) 520

Isaacson, D.M., Tarachi, G., Pitera, A.J., Ariel, N., Langdon d, T.A., Fitzgerald, E.A., J. Electrochem. Soc., **153** (2006) G134

Ishikawa, Y., Shibata, N., Fukatsu, S., Appl. Phys.Lett. 75 (1999) 983

Matthews, J. W., Blakeslee, A. E., *J. Cryst. Growth,* **27** (1974) 118

Nakaharai, S., Tezuka, T., Sugiyama, N., Moriyama, Y., Takagi, S., Appl. Phys. Lett. **83** (2003) 3516

Tang Y. S., Zhang, J., Hemment, P.L.F., Sealy, B.J., Liu, H., Castle, J.E., Newstead, S.M., Powell, A.R., Whall, T.E., Parker, E.H.C., J. Appl. Phys. **67** (1990) 7151

Tezuka, T., Sugiyama, N., S. Takagi, Appl. Phys. Lett. **79** (2001) 1798

CHAPTER 2

BACKGROUND STUDY ON GeSi

A review of the physical and electrical properties of Group IV semiconductors, Si and Ge, and their alloys is given in this chapter. A successful development of a suitable GeSi thin-film template growth depends upon a thorough understanding of this binary alloy.

2.1 Crystal Structure

Silicon (Si) and germanium (Ge) are elemental semiconductors from Group IV that are commonly used in digital microelectronics. They both crystallize with a diamond structure with the space group of Fd3m. The cubic unit cell, as illustrated with Figure 2.1, comprises eight atoms per unit cell with a coordination number 4 (the number of nearest neighbor atoms). The loosely-bonded diamond structure has an atomic packing factor of 0.34 (i.e., only 34 % of the space is occupied by the atoms).

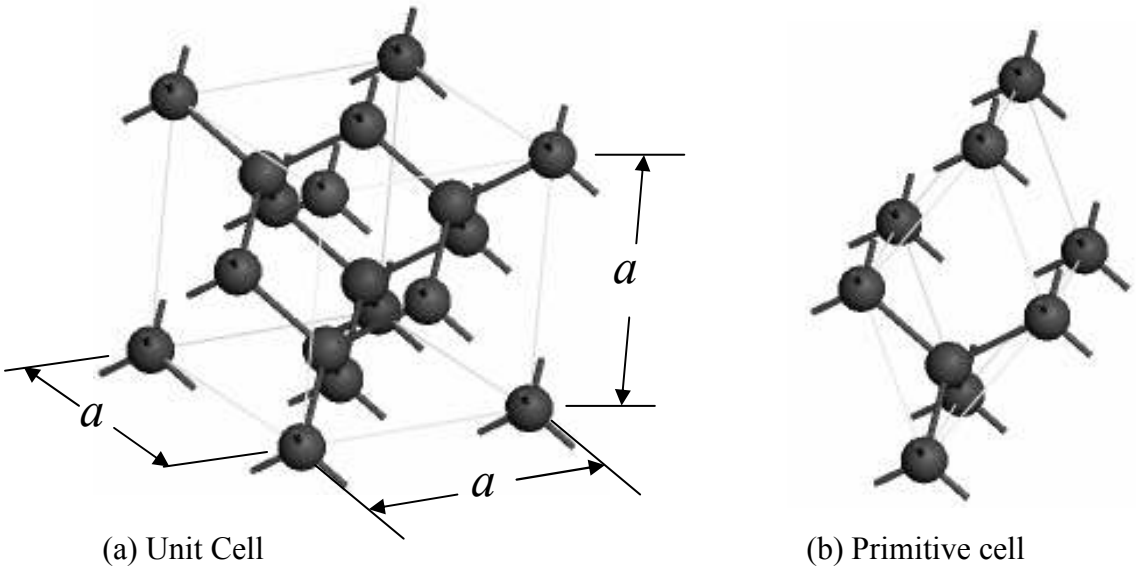

(a) Unit Cell (b) Primitive cell

Fig. 2.1 Diamond cubic structure of Si and Ge crystals.

2.2 Lattice Parameter

The lattice constants of Si and Ge are a_{Si} = 5.431 Å and a_{Ge} = 5.658 Å, respectively [Dismukes *et al.*, 1964]. The lattice parameters of SiGe alloys are functions of composition and are empirically given by,

$$a_{Si_{1-x}Ge_x} = 5.431 + 0.20x + 0.027x^2 \text{ (Å)} \ldots\ldots\ldots (2.1)$$

which is represented graphically in Figure 2.2.

A simpler approximation method, known as Vegard's law, assumes a simple compositional scaling of the lattice parameter [Denton and Ashcroft, 1991] as follows,

$$a_{Si_{1-x}Ge_x} = a_{Si}(1-x) + a_{Ge}x \ldots\ldots\ldots (2.2)$$

An associated lattice mismatch with Si is given by

$$f = (a_{Si_{1-x}Ge_x} - a_{Si}) / a_{Si} = 0.042x \ldots\ldots\ldots (2.3)$$

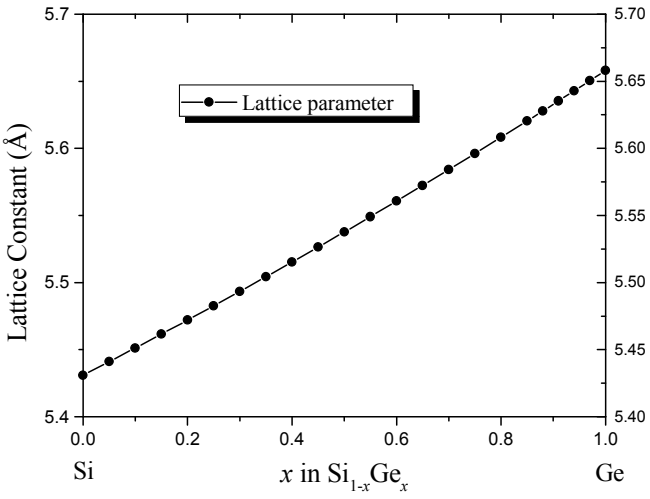

Fig. 2.2: Measured change in lattice constant with respect to germanium content in SiGe. Note the almost linear dependence on composition.

2.3 Band Structure

Better understanding of the physical structure of thin-film SiGe and Si:$Si_{1-x}Ge_x$ heterostructures is needed if the technology is to be developed as a growth template for lattice

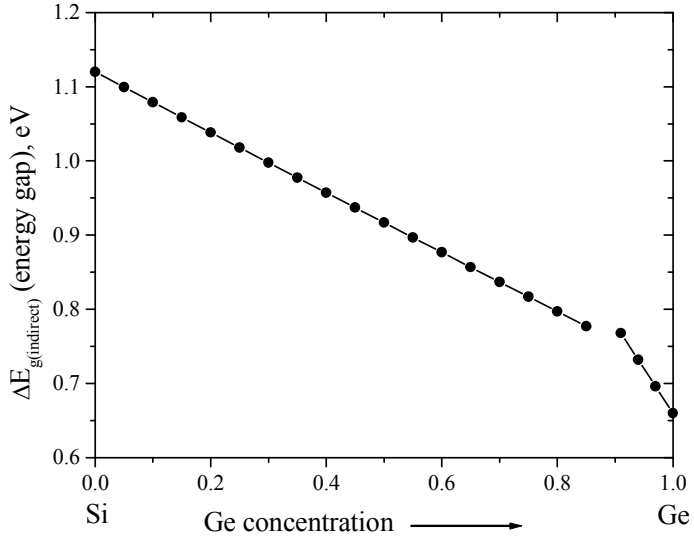

Fig. 2.3: Change in band gap with respect to germanium content in $Si_{1-x}Ge_x$

mismatched films. Si and Ge are both indirect bandgap semiconductors with band gap minima of 1.12 eV and 0.66 eV, respectively. The composition-dependent energy gaps of the alloys can be expressed [Krishnamurthy *et al.*, 1985, Kustov *et al.*, 1983] as:

$$\Delta E_{g(indirect)} (Si_{1-x}Ge_x) \approx (1.12 - 0.41x + 0.008x^2) \text{ eV}, x < 0.85 \ldots \ldots \ldots (2.4)$$

$$\Delta E_{g(indirect)} (Si_{1-x}Ge_x) \approx (1.86 - 1.2x) \text{ eV}, x > 0.85 \ldots \ldots \ldots (2.5)$$

(represented graphically in Figure 2.3). Interestingly, an abrupt change in behavior can be seen to occur near a Ge concentration of 85 %. This is associated with the transition between the band structure near the band edges, which becomes more Ge-like at this critical concentration [Wang and Zheng, 1995]. The conduction band edges in Ge are located at equivalent L points in

the Brillouin zone with a spherodial energy surface oriented along equivalent <111> direction. In silicon, the conduction band edges are spheroids oriented along equivalent <100> directions in the Brillouin zone [Kittel, 1976].

A pseudomorphic GeSi thin film on Si produces a heterojunction with valence and conduction-band discontinuities due to band offsets, which are affected by a number of factors including mismatch strain and interfacial properties. Conduction band offset is negligible compared to that of the valance band. Valance band discontinuity, ΔE_V, is responsible mostly for the band offset and is related to the germanium concentration as follows:

$$\Delta E_v = 0.74x \text{ (eV)} \ldots \ldots \ldots (2.5)$$

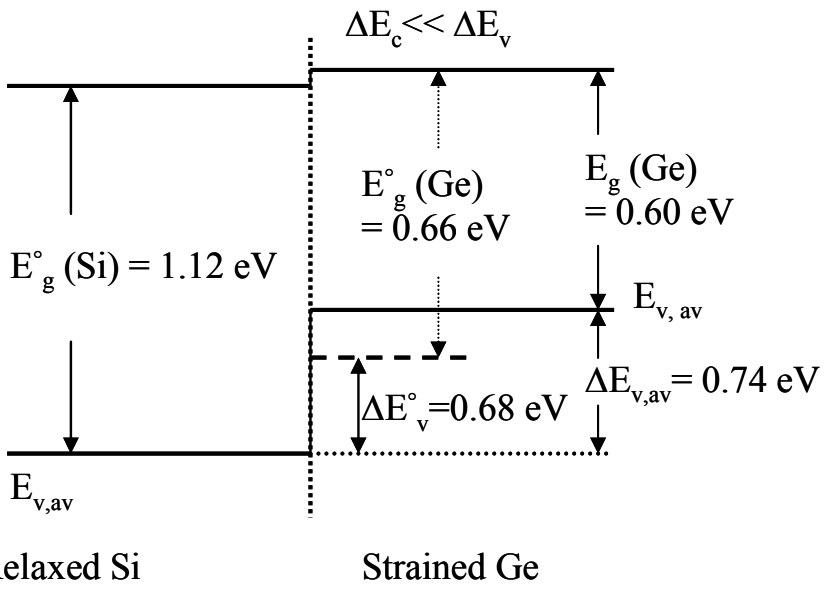

Fig. 2.4: Band alignment of GeSi heterostructure; E°_g and ΔE°_v represent the relaxed materials.

Figure 2.4 illustrates the valence band line-up of pseudomorphically grown Ge on Si. The average valance band positions in silicon and in germanium are $E_{v,av,si}$= −7.03 eV and $E_{v,av,Ge}$= −

6.35 eV, respectively. The strain related valance band offset can be expressed as [Van de Walle, 1995]:

$$\Delta E_{v,av} = a_v \frac{\Delta V}{V} = a_v \left(2\varepsilon_{\parallel} + \varepsilon_{\perp}\right) \ldots\ldots\ldots (2.6)$$

where a_v is the deformation, $\varepsilon_{\parallel}$ is in-plane strain, and $\varepsilon_{\perp}$ is out-of-plane strain. Therefore, it is evident that the band alignment of SiGe heterostructure is influenced by lattice strain.

2.4 Metallurgical Properties

The binary SiGe system is completely soluble over the entire compositional range as indicated by the phase diagram (shown in Figure 2.5). Solidus and liquidus lines are related as a function of germanium concentration as given below [Stohr and Klemm, 1954)];

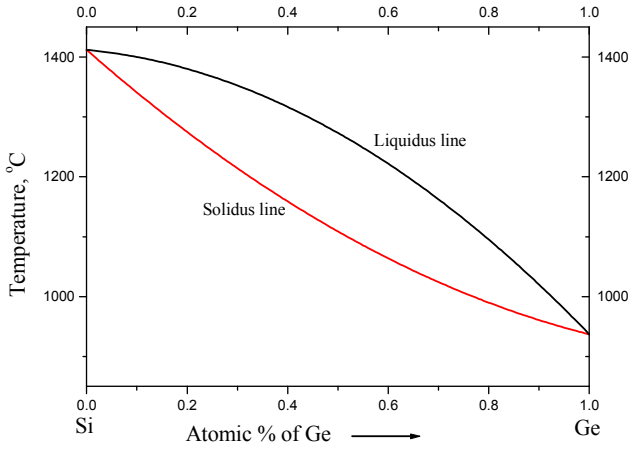

Fig. 2.5: Solidus-liquidus curve for $Si_{1-x}Ge_x$ system.

Solidus Temperature:

$$T_s \approx (1412 - 738x + 263x^2)\ ^{\circ}C \ldots (2.7)$$

Liquidus Temperature:

$$T_l \approx (1412 - 80x - 395x^2)\ ^{\circ}C \ldots (2.8)$$

where the melting points of Si and Ge are 1412 °C and 937 °C, respectively. The lower melting point of Ge restricts temperatures used in thermal processing of samples with high germanium concentrations.

2.5 Thermal Expansion Coefficients

Similar to the lattice parameter, matching of thermal expansion is very important in heterostructural thin film synthesis. The room temperature linear thermal expansion coefficient (TEC), α, of $Si_{1-x}Ge_x$ alloy varies with composition as follows [Zhdanova *et al.*, 1967]:

$$\alpha = (2.6 + 2.55x) \times 10^{-6}\ K^{-1} \quad \text{for } x < 0.85 \ldots\ldots\ldots (2.9)$$

$$\alpha = (7.53 - 0.89x) \times 10^{-6}\ K^{-1} \quad \text{for } x > 0.85 \ldots\ldots\ldots (2.10)$$

which is represented graphically in Figure 2.6. The abrupt change in the trend around 85 % germanium concentrations is similar to the behavior of the energy bang gap, and is also believed to be due to the transition of $Si_{1-x}Ge_x$ alloy from Si-like to Ge-like [Wang and Zheng, 1995].

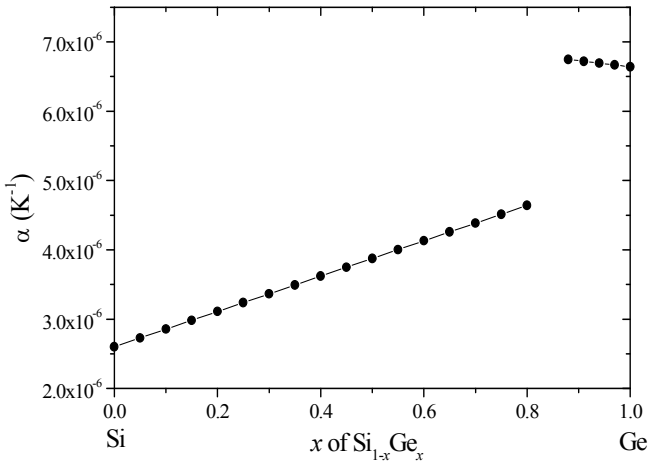

Fig. 2.6: Thermal expansion co-efficient of $Si_{1-x}Ge_x$

The temperature dependence of the TECs of $Si_{1-x}Ge_x$ and HgCdTe are superimposed with the help of Nader Elmarhoumi of UNT (personal communication) in Figure 2.7 to compare the compatibility of these two materials. The TEC of HgCdTe is seen to increase sharply with temperature between 130 K to 200 K, afterwhich its temperature dependence is very weak [Rogalski, 2005]. The TEC of pure silicon is well below that of HgCdTe throughout the temperature range, making it unsuitable for HgCdTe growth despite the attempts of different

groups. On the bright side, the TEC of $Si_{1-x}Ge_x$ alloy with the higher Ge concentrations falls in close proximity to that of HgCdTe, which might make Ge_xSi_{1-x} a better substrate for hetero-epitaxial device integration.

Stress associated with the lattice mismatch can lead to the formation and propagation of dislocations in heterostructures. It also changes the band alignments. Such dislocations can be electrically active within the heterostructure, resulting in degradation of its properties.

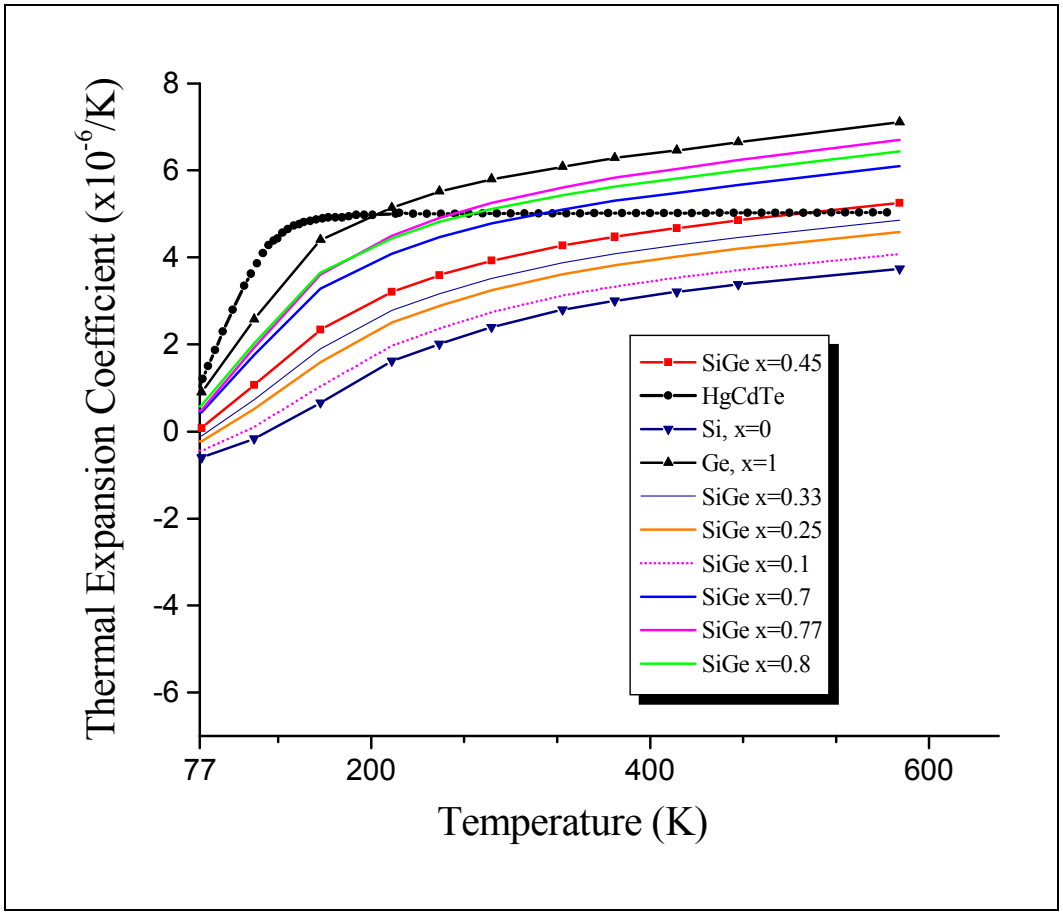

Fig. 2.7: Temperature dependent thermal expansion coefficients of Si_xGe_{1-x} and HgCdTe.

2.6 Strained-layer Semiconductor

2.6.1 Introduction

The strain associate with the lattice mismatch is usually accommodated elastically below

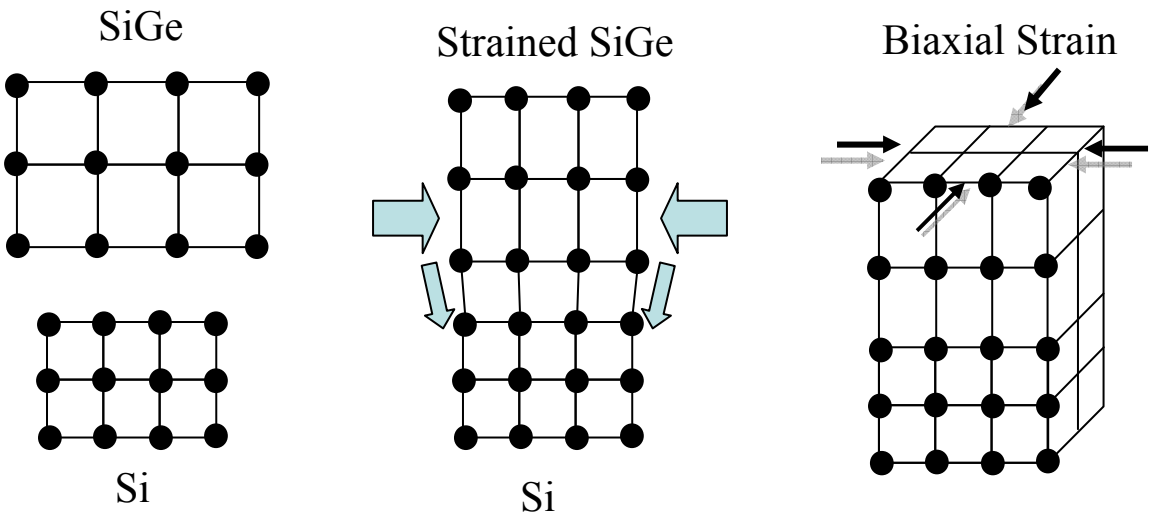

Fig. 2.8: Schematic illustration of strain associated with lattice parameter mismatch in Si:SiGe heterostructure.

a critical thickness by biaxial strain within the layer [Dodson and Tsao, 1989], as is schematically illustrated with Figure 2.8. Beyond the critical thickness, the strain energy is sufficient to promote plastic relaxation through production of misfit dislocations as illustrated in Figure 2.9. Such misfits can generate threading dislocations that penetrate through the entire film. Such defects will generally deleteriously affect the operation of any electro-optical devices fabricated within the heterostructure. The control of this mechanism of strain relaxation, i.e., dislocation formation, is crucial to the integration of dissimilar materials, and is the object of the present study.

Matthews and Blakeslee [1974] established a model describing the mechanism of misfit dislocation development to attain stability or equilibrium between lattice mismatched layers.

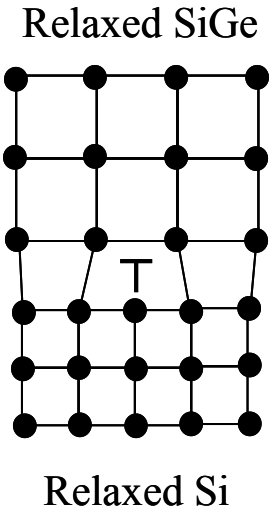

Fig. 2.9: Schematic of misfit dislocation.

The model predicts a critical thickness for a strained film that marks the thermodynamic onset of misfit dislocation formation. The critical thickness given by Matthews and Blakeslee [1974] is considered carefully during the course of this dissertation especially in experimental design and relaxation study.

2.6.2 Critical Thickness for Strained-layer Stability

If the film cannot provide enough energy for the formation of misfit dislocations then the lattice mismatch between the film and substrate is accommodated within the film by elastic strain by either biaxial tension or compression. The associated critical thickness, relating to the maximum elastic stress that can be thermodynamically accommodated within the film, is derived according to Matthew and Blakeslee [1974] as follows. First, it is a function of lattice mismatch and can be calculated by considering strain relaxation by dislocation formation only as described by Dodson and Tsao [1989]. If the crystals forming both film and substrate are isotropic with equal elastic constants, the force exerted by misfit strain is given by [Hull, 1995]:

$$F_s = \frac{2G(1+\nu)}{(1-\nu)} bh\varepsilon \cos\lambda \quad \ldots\ldots\ldots (2.11)$$

Furthermore, the tension in the dislocation line is given by [Hull, 1995]:

$$F_d = \frac{Gb^2}{4\pi(1-\nu)}\left(1-\nu\cos^2\alpha\right)\left(1+\ln\frac{b}{h}\right) \quad \ldots\ldots\ldots (2.12)$$

where G is the shear modulus, ν is Poisson's ratio, b is the size of the Burgers vector, h is the thickness of the strained layer, λ is the angle between the slip direction and the direction perpendicular to the film plane, α is the angle between the Burgers vector and the dislocation direction, and ε is the strain. The strain is maximum when it equals half of the lattice mismatch f. This gives the stability condition for determining the elastic limit of a strained film and is expressed as follows [Paul, 2004]:

$$F_d \leq \frac{F_{e(\max)}}{2} \quad \ldots\ldots\ldots (2.13)$$

which corresponds to the critical thickness [Paul, 2004],

$$h_c = \frac{b}{2\pi f}\frac{(1-\nu\cos^2\alpha)}{(1+\nu\cos\lambda)}\left(1+\ln\frac{h_c}{b}\right) \quad \ldots\ldots\ldots (2.14)$$

This critical thickness for stable and relaxed $Si_{1-x}Ge_x$ layers on silicon is graphically represented in Figure 2.10 as a function of germanium concentration. The Burgers vector (the slip distance of one side compared to other side after completing dislocation movement) magnitude, b, is taken as $a/\sqrt{2}$ where a is the lattice parameter of silicon; f is the lattice mismatch given by $0.042x$; and $\alpha = \lambda = 60°$. In Figure 2.10, the solid black line represents the equilibrium values of the Matthews and Blakeslee [1974] model for the critical thickness as a function of germanium concentration for a Ge_xSi_{1-x}/Si heterostructure (graphical representation of Equation 2.14). The red line (and symbols) represents the experimental observations by Douglas J. Paul [2004] during molecular beam epitaxy (MBE) growth of Ge_xSi_{1-x} on Si (100) at 550 ˚C. The superimposed graph (Figure 2.10) is generated to demonstrate that pseudomorphic layers could be grown well above the equilibrium critical thickness predicted by Matthews and Blakeslee [1974] as demonstrated by different research groups [Hull, 1995, Paul, 2004]. Robert Hull

[1995] related the discrepancy between theory and low temperature experimental observation of critical thickness to the kinetic barrier associated with the relaxation process. The regime between the theoretically calculated thickness and the experimental observations is usually known as the *metastable* regime. Due to the initial sluggishness of relaxation, a strained layer can be grown slightly thicker than the critical value without onset of dislocation formation as demonstrated by different research groups [Paul, 2004, Dodson and Tsao, 1989]. It is evident from the plot (in Figure 2.10) that a 1.8 nm Ge strained layer is stable but can grow pseudomorphically below 5 nm. Our study will be limited to the metastable range where films are pseudomorphic.

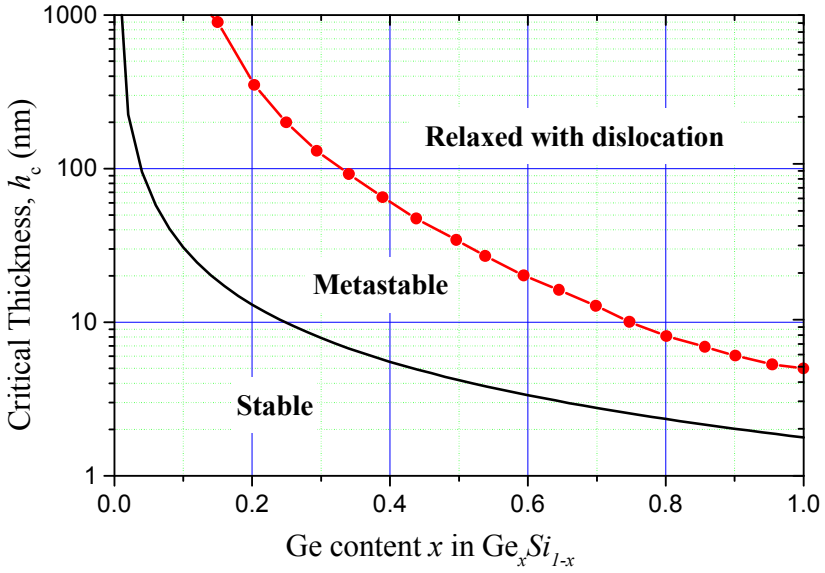

Fig. 2.10: Graphical representation of Matthews and Blakeslee [1974] critical thickness of pseudomorphic $Si_{1-x}Ge_x$ layers as a function of germanium fraction (solid black line) comparing to experimental values of Douglas J. Paul [Paul, 2004] (given by red line and symbols) .

2.7 References

Denton, A.R., Ashcroft, N.W., Phys. Rev. A **43** (1991) 3161

Dismukes, J.P., L. Ekstrom, E.F. Steigmeier, I. Kudman, D.S. Beers, *J. Appl. Phys.* **35** (1964) 2899

Dodson, B. W., Tsao, J. Y., Annu. Rev. Mater. Sci.. 19 (1989) 419

Hull, R., Section 1.2, 1.3 in *Properties of Strained and Relaxed Silicon Germanium*, Edited by Eric Kasper, INSPEC, Germany (1995)

Kittel, C., *Introduction to Solid State Physics*, John Wiley & Sons Inc., New York, (1976)

Krishnamurthy, S., Sher, A., Chen, A., Appl. Phys. Lett. **47** (1985) 160

Kustov, E.F., Mel'nikov, E.A., Sutchenkov, A.A., Levadnii, A.I., Filikov, V.A. *Sov. Phys. Semicond.* **17** (1983) 481

Matthews, J. W., Blakeslee, A. E., *J. Cryst. Growth,* **27** (1974) 118

Paul, D.J., Semicond. Sci. Technol. **19** (2004) R75

Rogalski, A, Reports on Progress in Physics **68** (2005) 2267

Stohr, H., Klemm, W., Z. Anorg. Allgem. Chem. **241(**1954) 305

Van de Walle, C.G., in *Properies of Strained and Relaxed Silicon Germanium*, Edited by E.Kasper, INSPEC, Germany (1995)

Wang, K.L., Zheng, X., in *Properies of Strained and Relaxed Silicon Germanium*, Edited by E.Kasper, INSPEC, Germany (1995)

Zhdanova, V.V., M.G. Kakna, T.Z. Samadashvili, *Izv. Akad. Nauk. SSSR Neorg. Mater.* **3** (1967) 1263

CHAPTER 3

TECHNIQUES FOR MATERIALS MODIFICATION AND CHARACTERIZATION

3.1 Ion Beam Characterization and Materials Modification

As discussed in Chapter 1, the growth of bulk SiGe [Usami *et al.,* 2002] and heteroepitaxial SiGe thin films on silicon is technically very challenging. Alternatively, a novel approach of forming thin GeSi films on Si is reported in this thesis. In this work Ge-ions were implanted into either bulk Si or SOI followed by thermal oxidation. Since this method is not a growth technique, per say, it does not involve island formation and therefore yields a very uniform and smooth GeSi film. A parametric study was done using different ion fluences, as well as oxidation conditions to segregate the Ge. Different processing and characterization techniques were used in this study, which will be discussed in this chapter.

3.1.1 Ion Implantation

Ion implantation involves uniformly irradiating a solid sample with either elemental or molecular ions to introduce lattice defects or impurities. As such, it is a rather easy and precise way of doping semiconductors [Franssila, 2004] and is also applied as a surface treatment technique in enhancing corrosion resistance and other metallurgical processes [Hirvonen and Clayton, 1983]. The basic implantation process in crystalline materials is shown schematically in Figure 3.1[Williams and Poate, 1984]. The bombarding ion goes through a series of collisions involving both nuclear and electronic interactions until it finally comes to a rest within the solid.

The affected volume within the solid in which atomic displacements and mixing occur is known as the collision cascade. The projected ion range and cascade size, and therefore damage and impurity profiles, are functions of ion energy/species, as well as the density and composition of the target. The temperature of the target increases during irradiation unless it is actively cooled. Implantation of heavy ions (e.g., Bi^+ or Ge^+) into silicon leads to a crystalline-to-amorphous transition at low or moderate fluence below 300 ˚C. Therefore, it is important to control the sample temperature during implantation if the ion-induced damage morphology must be controlled. The schematic diagram of the implantation beam-line is shown in Figure 3.2.

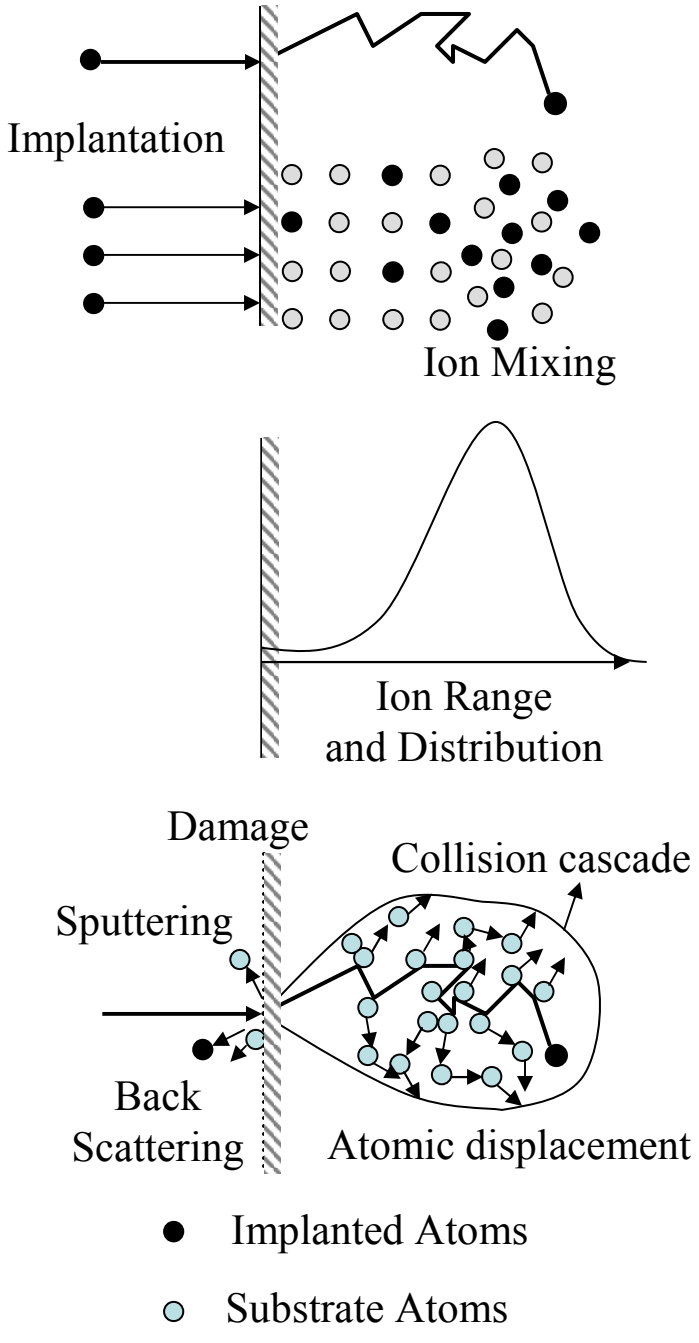

Fig. 3.1: Schematic illustration of ion implantation basics.

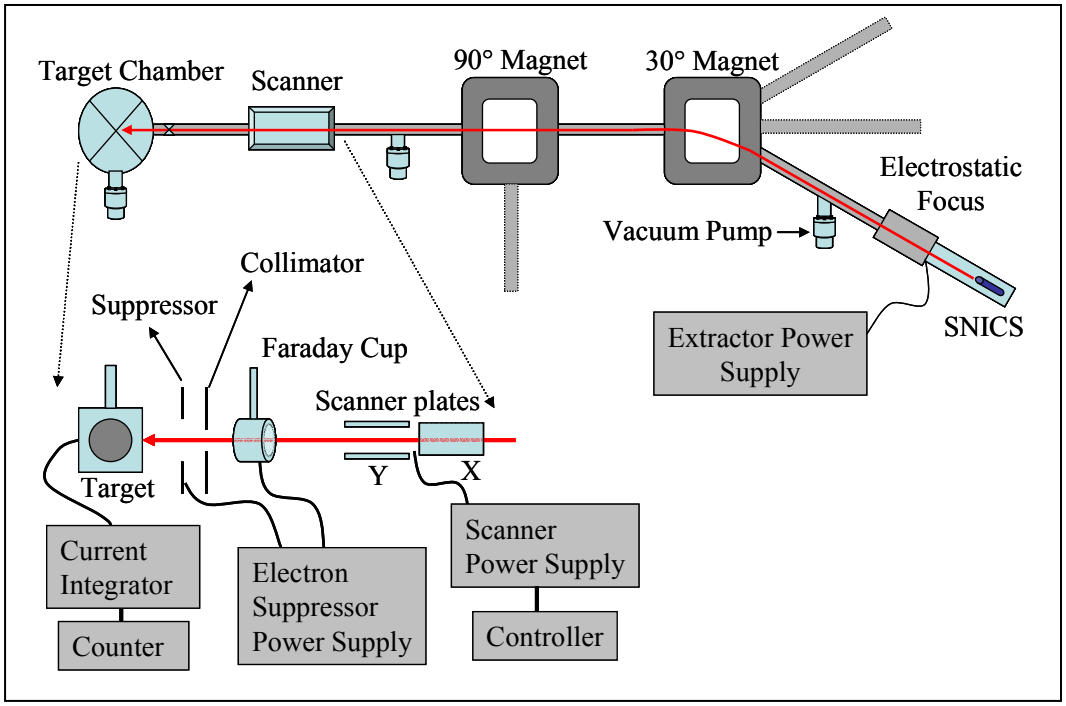

Fig. 3.2: Schematic diagram of low energy implant line.

The accelerator laboratory in the Physics Department at the University of North Texas has three ion implantation beam-lines. The low-energy beamline, shown above in Figure 3.2, is used for implantation of ions over an energy range of 10 to 70 keV, which is suitable for the present application. A source of negative ions by cesium sputtering (SNICS) was used, which can generate negative ions of virtually any element having a substantial electron affinity. The steps in developing an ion beam begin with making the source cathode from either a pure element of the desired ion or a closely related compound. The details of the choice of materials and helpful parameters can be found in the National Electrostatic Corporation's (NEC) SNICS owner's manual and the Negative Ion Cookbook [Middleton, 1989]. A germanium cathode was made from commercially-available, pure germanium. According to the Cookbook and the NEC owner's manual, a reasonable current, as high as 100 μA, can be extracted from the SNICS.

After extraction from the ion source, the ions are momentum/charge selected using the 30° magnet with an appropriate power setting, as shown in Figure 3.2. Subsequently, a high-voltage electrostatic X-Y scanner is used to scan the ions across the sample to achieve uniform exposure. Dosimetry is achieved using a simple current integration technique. A positive bias voltage is applied to the sample holder during current integration to ensure collection of secondary emissions, i.e. negatively-charged sputtered ions and electrons. A positively biased Faraday Cup is also used for beam setup. This integration scheme yields the implant fluence, *D* (ions/cm^2), according to the equation 3.1

$$D = \frac{I \times t}{A} \times \frac{1}{q \times C} \quad \ldots\ldots\ldots\ldots\ldots (3.1)$$

where, *I* is current in amperes, *t* is time in seconds, *A* is area in cm^2, *q* is the charge state, and *C* is charge of an electron, i.e., 1.6×10^{-19} coulombs.

Implantation fluences generally ranged from 3×10^{14} to 3×10^{16} ions/cm^2 in the present study, although exact fluence requirements were determined in certain cases. A Monte-Carlo computer simulation code, the Stopping and Range of Ions in Matter (SRIM)/TRIM (Transport of Ion in Matter) [Ziegler *et al.*, 1985], was used to estimate parameters such as implantation energy, projected ion range and vacancy formation during the process (a separate section 7.1.1, Ion Irradiation, is provided for elaboration). A low current density (less than 1 μA/cm^2) is maintained during ion implantation to limit sample heating, calculated using the following equation:

Beam Heating: *P(Watts)* = *I* (current in milliamps) × *V* (beam energy in keV).

3.1.2 Stopping and Range of Ions in Matter

The Stopping and Range of Ions in Matter (SRIM) is a computer code developed by Ziegler *et al.* [1985] for simulating the penetration of energetic particles in materials through a quantum mechanical treatment of the ion-atom interaction. This Monte-Carlo simulation provides a very good method of estimating ion implantation parameters. The moving atom is by convention considered an "*ion*" (whether it is charged or neutral) and the target an "*atom*". The software simulates the slowing down and scattering of an energetic ion through interactions with the target atoms. Details about the software can be found in the SRIM user manual [Ziegler and Biersack, 2003] (also available online at www.srim.org). The collision cascade simulation is achieved by following the ions, which after penetration into the target suffer multiple nuclear and electronic collisions. The program follows one ion at a time until the associated stopping power slows the ion to some pre-determined velocity. The equation for stopping power i.e., the energy loss per unit path length is [Feldman and Mayer, 1986]:

$$\frac{d\mathrm{E}}{dx} = -\frac{2\pi Z_1^2 e^4 N Z_2}{E}\left(\frac{M_1}{m}\right)\ln\frac{2mv^2}{I} \quad \ldots\ldots\ldots (3.2)$$

where, Z_1 and Z_2 are the atomic number of the ions and target atoms respectively, M_1 and m are the masses of the ions and atom electrons respectively, and v is the ion velocity, I is the excitation energy (~$10Z_2$ in eV for most elements), N is atomic density in the stopping medium in cm^{-3}, E is ion energy in eV and e is electron charge, which in combination gives stopping power in eV/cm or more commonly MeV·cm^2/gm.

This simulation program provides information with range table as well as graphical representation of ion penetration, collision cascade and range distribution. Ion-induced damage is represented by the vacancy distribution. Since atomic displacement involve the formation of a Frenkel defect [Kittel, 2005], i.e., an interstitial-vacancy pair, it is important to realize that the

vacancy distribution is highly correlated to the interstitial profile. Also, it is important to understand that SRIM is a simulation routine that only considers ion-atom interactions and does not include any thermal effects such as defect interactions such as recombination, clustering, etc. Therefore, residual ion-induced damage in implanted samples can differ substantial from SRIM simulations. Some of the calculated results are shown graphically in Figure 3.3

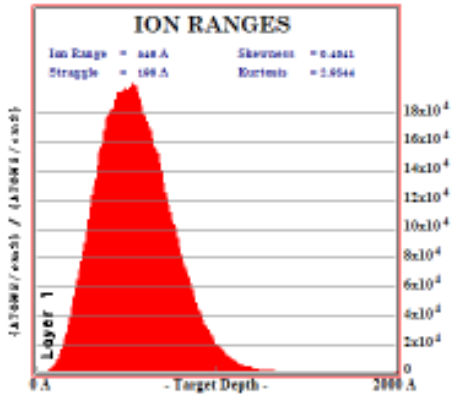

(a) Distribution of 70 keV Ge-ion in Si

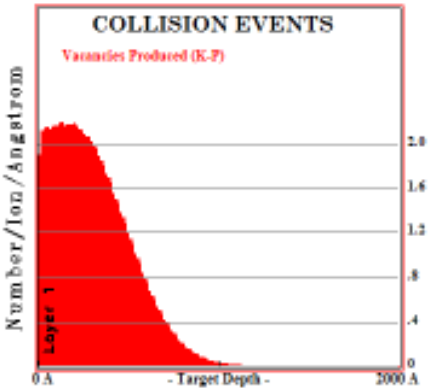

(b) Vacancy distribution

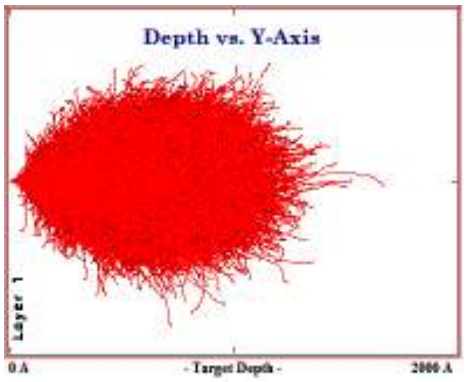

(c) Lateral straggling

Fig. 3.3: SRIM/TRIM simulation of 70 keV Ge-ion implantation of silicon showing (a) ion distribution, (b) vacancy distribution, and (c) lateral ion straggling.

Ion ranges are described here by considering the final ion distribution to be cylindrically symmetric. The Projected Range is the first moment of the ion distribution, and Straggle, Skewness and Kurtosis are the second, third and forth moments, respectively. The terms are defined as follows [Ziegler and Biersack, 2003]:

$$\left.\begin{aligned} &\text{Mean Projected Range, } R_p = < x > = \sum_i x_i / N \\ &\text{Straggle, } \sigma = < (\Delta x_i)^2 >^{1/2} \\ &\text{Skewness, } \gamma = < \Delta x^3 > / < \Delta x^2 >^{3/2} \\ &\text{Kurtosis, } \beta = < \Delta x^4 > / < \Delta x^2 >^2 \end{aligned}\right\} \quad \ldots\ldots (3.3)$$

where x_i is the projected range along x axis and is identical for lateral and radial directions.

3.2 Ion Beam Materials Characterization

3.2.1 Rutherford Backscattering Spectrometry (RBS)

At every stage of sample preparation and materials processing, ion beam characterization was used, especially Rutherford backscattering/channeling spectrometry for measuring the thickness of the oxide layers, as well as the composition and strain of the Ge_xSi_{1-x} films. Spectral simulation using a standard computer code, SIMNRA [Mayer, 1997], was used to determine parameters such as composition of the Ge_xSi_{1-x} layers and the oxide thickness from the parameters used in the simulated spectra to achieve the best fit to the experimental spectra.

Rutherford backscattering spectrometry (RBS) is a nondestructive analytical technique used in materials characterization [Feldman and Mayer, 1986]. It is a consequence of the seminal experiment involving scattering of high-energy alphas from a gold foil performed by Ernest Lord Rutherford in 1911, and, as such, bears his name. Rutherford concluded that alpha particles are backscattered from a thin gold foil by interaction with the positively-charged nucleus of a gold atom. Rutherford correctly described the atom as consisting of a tiny positive nucleus orderly surrounded by negatively charged electrons in contrast to the plum pudding model of the atom as proposed by J. J Thompson [1904].

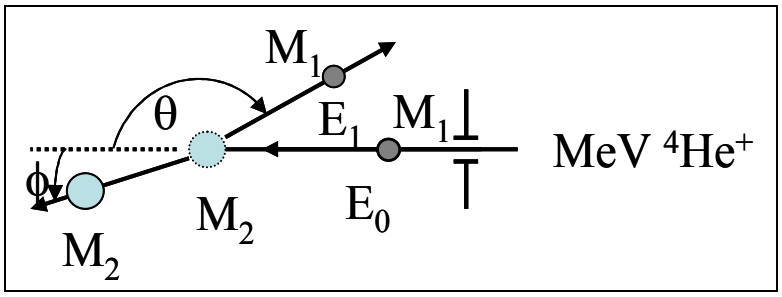

Fig. 3.4: Schematics of elastic collision between an ion and a target atom.

With the development of particle accelerators, RBS became a popular technique for thin film characterization, where the energy spectrum of elastically backscattered ions is used to determine the film's parameters, i.e., composition and thickness. The schematic representation of an elastic collision is provided in Figure 3.4. The energy of a backscattered ion is determined by a standard solid-state, surface-barrier detector, which is integrated with standard pulse processing modules to yield a histogram of the backscattering events.

Both the intensity and energy of the backscattered ions provide information about the near surface (up to ~0.5 μm depth for $^4He^+$ beam) of materials. The energy of the backscattered beam is proportional to the incident energy within a proportionality constant, the kinematic factor, which is characteristic of the target and ion mass. Using conservation of momentum before and after collision and solving the two-particle central force problem in the lab frame, the kinematic factor, *K*, can be derived [Feldman and Mayer, 1986] as Equation 3.4:

$$\frac{E_1}{E_0} = K = \left[\frac{\left(M_2^2 - M_1^2 Sin^2\theta\right)^{1/2} + M_1 Cos\theta}{M_1 + M_2} \right]^2 \quad \ldots\ldots\ldots (3.4)$$

where E_0 and M_1 are the incident particle energy and atomic mass, respectively, E_1 is the scattered particle energy, M_2 is the target atomic mass, and θ is the scattering angle. Thus, the

target mass is easily identified by the scattered ion energy for a specific ion beam and scattering angle.

Quantitative thin-film analysis can be done using the scattering *cross section,* which relates the intensity of the incident and scattered ions. The theoretical expression for the Rutherford scattering cross section is given by [Feldman and Mayer, 1986]:

$$\sigma(E,\theta) = \left(\frac{d\sigma}{d\Omega}\right) = 1.296\left(\frac{Z_1 Z_2}{E_0}\right)^2 \left[\frac{1}{Sin^4\,\theta/2} - 2\left(\frac{M_1}{M_2}\right)^2\right] \ldots\ldots (3.5)$$

where E_0 is the incident beam energy, θ is the scattering angle, Z stands for atomic number and M for atomic mass with subscripts 1 and 2 representing incident ions and target atoms respectively. The differential cross section of a given process is defined by a probability, P as,

$$P = \frac{I\sigma N t d\Omega}{I} \ldots\ldots\ldots (3.6)$$

where, I is the number of incident particles, N is atomic density and t is the thickness (i.e. Nt is areal density or target thickness as atoms/cm^2) and $I\sigma Ntd\Omega$ as the number of interactions with σ as the cross section in cm^2/sr. Therefore, if the scattering cross-section is known, the target thickness can be calculated and *vice versa*.

The experimental setup for RBS is illustrated in Figure 3.5. As mentioned earlier, the backscattered particles are detected with a solid-state detector. These detectors are made of a semi-conducting material and are operated much like a solid state diode under reverse bias. The applied high voltage generates a thick *depletion layer* and any charge created by the radiation in this layer is collected at an electrode. The charge, thereby, collected is proportional to the energy deposited in the detector and therefore these devices can also yield information about the energy

of individual particle or photons of radiation. The detectors are made mostly from silicon or germanium.

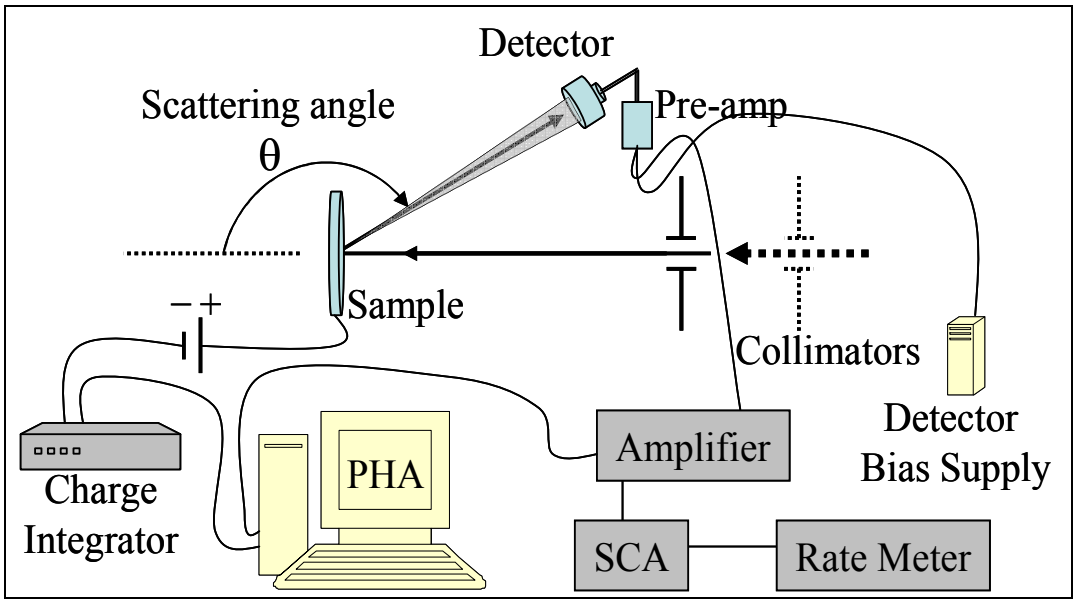

Fig. 3.5: Schematics illustrating experimental set up for RBS.

The signal from the detector is amplified and analyzed with a multi-channel pulse height analyzer (PHA). A computer interface module is used to plot counts as a function of channel number, which represents energy. At near-normal beam incidence the RBS spectral peak can provide target thin film thickness or the areal density, as atoms/cm^2, of a substrate impurity for a given experimental set up as follows:

$$Nt = \frac{\sum - \beta}{I \times \Delta\Omega \times \sigma(E,\theta)} \quad \ldots\ldots\ldots (3.7)$$

where $\sum - \beta$ is the net area under the spectral peak, $\Delta\Omega$ is the detector solid angle in steradians (sr), which is equal to the detector area divided by the square of the distance between target and detector, and σ is the cross section in cm^2/sr.

The limitations of RBS are mainly two-fold. Elastic backscattering requires that the target atoms be much heavier than the beam particles. Therefore, only heavier impurities on lighter substrates are, in general, identifiable. This problem can be partially addressed by a suitable choice for the incident ion beam. Secondly, the detector resolution limits both depth and mass resolution. The mass resolution can be improved by using higher ion energy according to Equation 3.8. The depth resolution can be substantially increased by using a grazing angle of incidence for the beam achieved by tilting the sample away from the detector as shown with a SIMNRA simulation (represented in Figure 3.6). Depth resolution and energy resolution are related by the following equation [Feldman and Mayer, 1986]:

$$\Delta E = \left[\frac{K}{\cos\theta_1} \frac{dE}{dx_{in}} + \frac{1}{\cos\theta_2} \frac{dE}{dx_{out}} \right] x \quad \ldots\ldots\ldots (3.8)$$

where ΔE is the energy resolution and x is depth resolution, K is the kinematic factor. Incident and exit angles (θ_1 and θ_2, respectively) are illustrated in Figure 3.6.

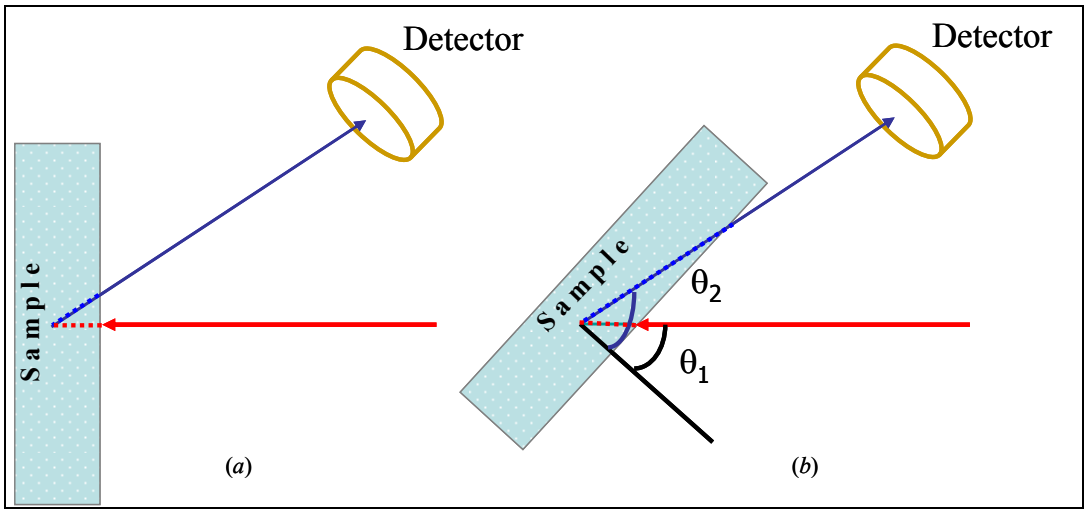

Fig. 3.6: Schematic illustration of the relation between beam incident angle and detector resolution. (a) Normal incident (low resolution) (b) grazing exit (high resolution).

3.2.2 Ion Channeling

Channeling is a phenomenon that occurs in single-crystal samples when the ion beam is incident along or near a major crytalographic direction, as shown in Figure 3.7. As such, correlated, small-angle collisions with the atoms in the atomic rows or planes lead to very regular

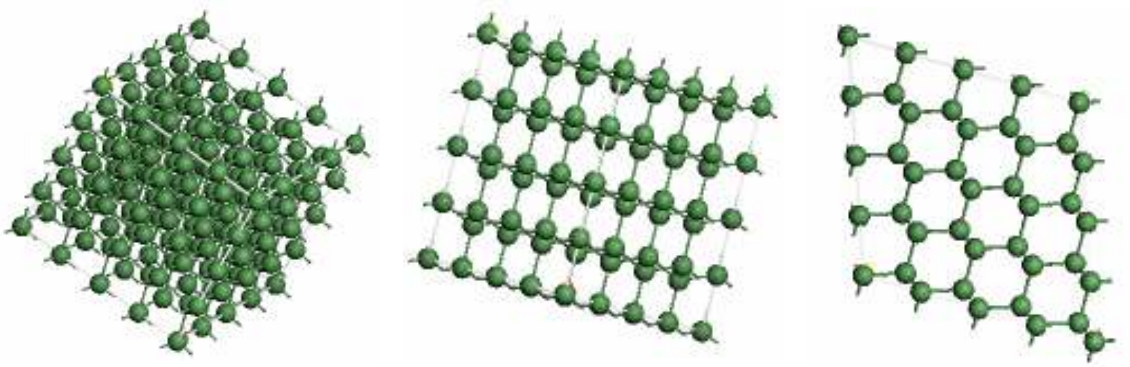

Random Direction Planar Direction Axial Direction

Fig. 3.7: Schematic illustration of crystal orientation with respect to the channeling direction.

oscillations of the ion trajectory within the lattice interstices. As a result, the backscattering yield for channeled ions is much reduced over that for ions moving randomly within the lattice. Since any atom displaced from a lattice site into the interstitial space will interact strongly with channeled ions, ion channeling can be used for structural characterization including profiling of defects and lattice strain, and lattice-location of impurities (i.e., interstitial or substitutional impurities).

Changing the alignment of the beam with respect to the channel by tilting the sample, results in a higher random fraction of the beam, i.e., the portion of the beam that moves as in a random solid. A critical angle, $\psi_{1/2}$, is defined to relate to the angular width of the channel. It

depends on beam energy E, atomic numbers of ion and target atoms, Z_1 and Z_2, and atomic spacing d as follows:

$$\psi_{1/2} = \alpha\left(\frac{2Z_1Z_2e^2}{Ed}\right)^{1/2} \quad \ldots\ldots\ldots (3.9)$$

where e is the charge of an electron and α expresses the dependence on lattice vibration with values ranging from 0.8 and 1.2 [Chu *et al.*, 1978]. The critical angle is usually referred to as the *half angle* for channeling.

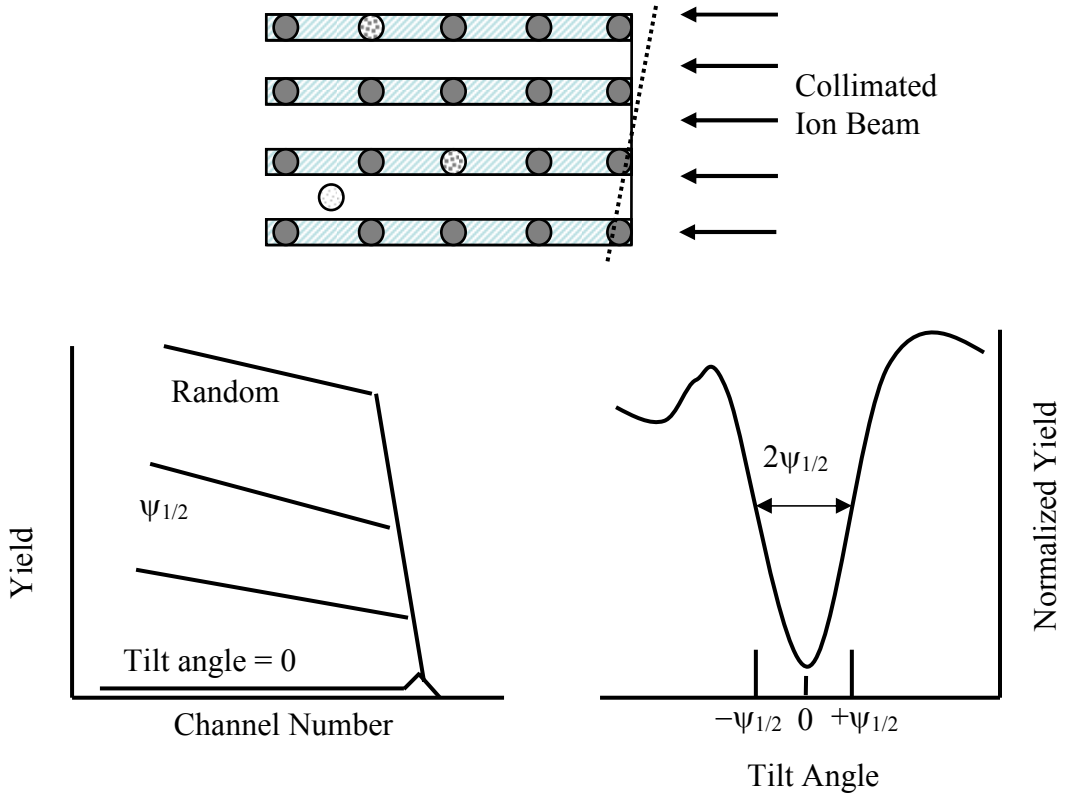

Fig. 3.8: Schematics of Ion channeling basics, beam steering and effects of small angle collisions on backscattering.

The sensitivity of ion channeling with tilt angle is illustrated in Figure 3.8. The target is scanned through tilt angles from random to the best possible channeling orientation by using a goniometer. It is clear that the backscattering yield increases as the tilt angle increases from the

channeling orientation. Sample manipulation was accomplished using a two-axis goniometer capable of angular steps of 0.01°, as illustrated in Figure 3.9. Only a few adjustments of electronic modules are required to the RBS setup for channeling experiments.

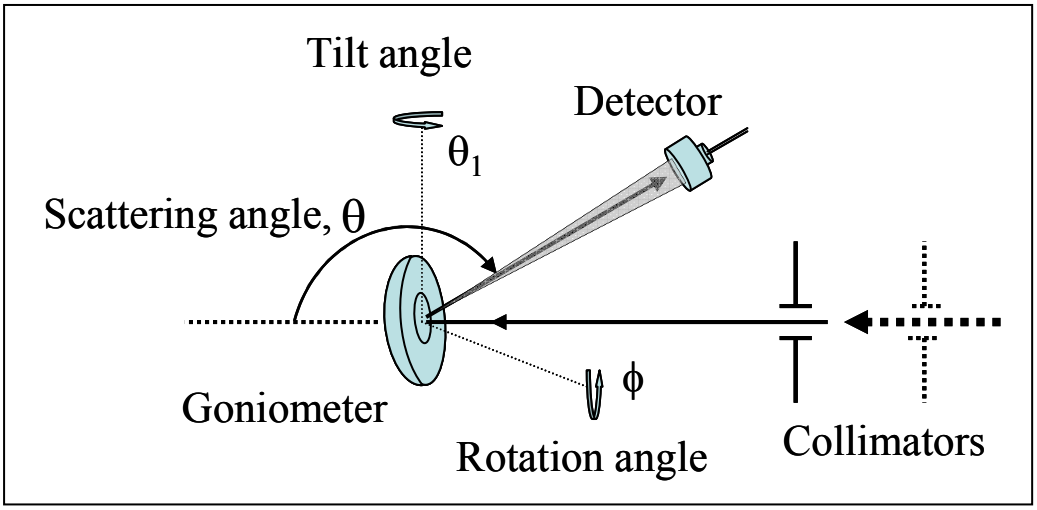

Fig. 3.9: Schematic illustration of experiment setup for ion channeling.

While characterizing a single-crystal thin-films or substrates, it is important to emphasize that Rutherford backscattering spectrometry (RBS) generally refers to random RBS, where samples are continuously rotated around the beam axis to avoid any ion channeling while keeping the scattering angle unchanged.

3.2.3 Oxide Thickness Characterization

Rutherford backscattering/channeling spectrometry is used for measuring the thickness of the grown oxide layers and the composition as well as the strain of the Ge_xSi_{1-x} films. Spectral simulation generated by a standard computer code, SIMNRA, is used to determine sample parameters that yielded a best fit to the experimental data. Parameters, such as composition of

the Ge_xSi_{1-x} layers and the oxide thickness, will be determined from the fit parameters used in the simulated spectrum.

Rutherford backscattering spectrometry (RBS) is not suitable for characterizing light impurities in a heavier substrate. The choice of RBS in analyzing thin layer of oxide on silicon poses similar disadvantages. However, RBS in conjunction with ion channeling (RBS/C) can be used to lower the backscattered yield from the Si substrate to improve the signal-to-noise ratio in the region of the histogram where scattering from oxygen occurs. This provides the sensitivity to monitor oxygen within the oxide layer at the surface.

3.2.4 Strain Characterization

Strain in the layer, which arises from the difference in lattice parameters, can be characterized by the proper use of the ion channeling technique. A strain layer of Si on a SiGe substrate is schematically illustrated with Figure 3.10. A scan across an axially channeled beam will not, in general, reveal any difference but a suitable choice of planner channeling (e.g., <110> scan in the (100) plane as illustrated with Figure 3.10) is able to resolve differences in the lattice parameter between strain and unstrained layers as illustrated with Figure 3.10.

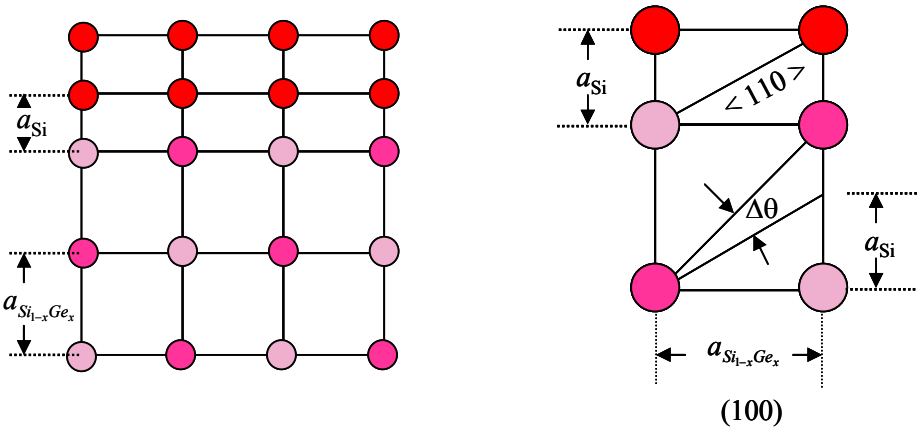

Fig. 3.10: Schematics of biaxial lattice strain and geometric illustration of strain calculation.

Characterization of a biaxially-strained film on a crystal substrate using angular scans across planar channels is shown in Figure 3.11. It is clear that the minimum yield, as well as the angular width of the channels, is similar for both the thin film and the substrates. However, the biaxial strain in the thin film leads to a displacement of the angular location of the minimum yield (i.e. the *zero channel*) to smaller angles. The displacement, $\Delta\theta$, of the angular scans can be used to calculate the strain as follows:

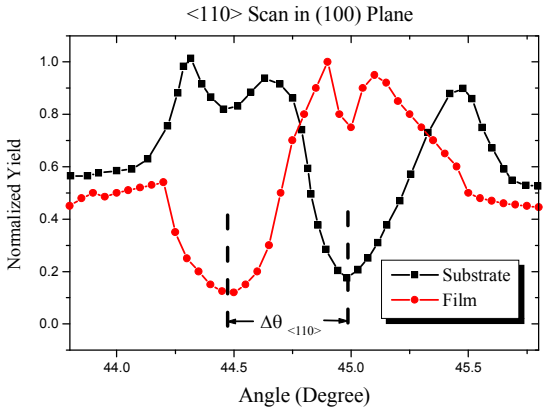

Fig. 3.11: Change in zero angle of channeling indicates lattice strain.

$$Strain = \frac{a_{Si_{1-x}Ge} - a_{Si}}{a_{Si}} = \frac{2\tan\Delta\theta}{1-\tan\Delta\theta} \approx 2\tan\Delta\theta \quad \ldots\ldots (3.10)$$

3.3 Raman Spectroscopy

According to classical electrodynamics, an oscillating dipole is a source of electromagnetic radiation. During the inelastic interaction between light and a molecule the polarizability of the molecule changes which shifts the oscillation frequency from that of the input field, and the shifted oscillation act as a source of secondary radiation. The phenomenon was first observed by an Indian Physicist, Chandrasekhara Venkata Raman, who was awarded the Nobel Prize in Physics in 1930 for his work on the scattering of light and for the discovery of the effect named after him.

3.3.1. Classical Electromagnetic Derivation of Raman Effect

If a light beam with electric field

$$E(t) = E_0 \cos \omega_0 t \ \ldots \ldots \ldots \ (3.11)$$

is incident on a molecule, the molecule will oscillate and causes momentary polarization. The polarization produces an instantaneous electric dipole moment. The resulting induced dipole moment, P is given by,

$$P(t) = \alpha E(t) \ \ldots \ldots \ldots \ (3.12)$$

where α is the polarizability of the molecule. α is in general a function of separation between the atoms, i.e. $\alpha = \alpha(x)$. If x is the displacement from the equilibrium separation between the atoms in the molecule, we can expand the polarizability about the equilibrium separation between the atoms, x_0, using a Taylor series, i.e.

$$\alpha(x) = \alpha_0 + \left(\frac{\partial \alpha}{\partial x}\right)_0 x(t) + \ldots \ \ldots \ldots \ldots \ (3.13)$$

where, for a vibration molecule,

$$x(t) = x_0 \cos \omega_v t \ \ \ldots \ldots \ldots \ (3.14)$$

So,

$$P(t) = \left[\alpha_0 + \left(\frac{\partial \alpha}{\partial x}\right)_0 x_0 \cos \omega_v t\right]\left(E_0 \cos \omega_0 t\right)$$

$$= \alpha_0 E_0 \cos \omega_0 t + \left(\frac{\partial \alpha}{\partial x}\right)_0 x_0 E_0 \cos \omega_0 t \cos \omega_v t$$

$$= \alpha_0 E_0 \cos \omega_0 t + \frac{1}{2}\left(\frac{\partial \alpha}{\partial x}\right)_0 x_0 E_0 \cos\{\omega_0 + \omega_v\} t + \frac{1}{2}\left(\frac{\partial \alpha}{\partial x}\right)_0 x_0 E_0 \cos\{\omega_0 - \omega_v\} t \ \ \ldots \ldots \ (3.15)$$

where the first term correspond to the oscillating dipole responsible for radiating light with the same frequency as the incident one known as Rayleigh scattering, and the following terms are

responsible for the Raman scattering. Vibrational interaction causes the frequency shift through the change in polarizability of the molecules, causing this "new type of secondary radiation" and showing the Raman effect [Raman and Krishnan, 1928 (a,b,c) Raman, 1929]. The scattering with frequency $(\omega_0 + \omega_\nu)$ is known as anti-Stokes scattering whereas the scattering with frequency $(\omega_0 - \omega_\nu)$ is known as Stokes scattering.

It can be inferred from the equation that the rate of change of polarizability with the vibration around the equilibrium position cannot be zero, i.e., $\left(\frac{\partial \alpha}{\partial x}\right)_0 \neq 0$ for a vibration to be Raman active. Vibrational spectra of small molecules in gaseous states also exhibit rotational fine structures. So, rotational transitions also cause Raman effects to some extent, the classical electromagnetic description of which is as follows:

During the course of rotation, the orientation of the molecule with respect to the electric field of radiation changes, and therefore, if the molecule is not optically isotropic, (i.e., it exhibits different polarizability in different directions), then its polarizability will change with time [Ferraro *et al.*, 1985].

The polarizability of a molecule rotating with time can be expanded as

$$\alpha(t) = \alpha_0 + \Delta\alpha \cos(2\omega_r t) + \cdots \quad \ldots (3.16)$$

where, ω_r is the rotational angular frequency of the molecule and $\Delta\alpha = \alpha_{\parallel} - \alpha_{\perp}$ is the anisotopic part of the polarizability [Gupta *et al.*, 1984]. $2\omega_r$ is given instead of ω_r because the rate at which the polarizability changes is twice as great as the rotation due to the fact that a rotation through π angle will bring the diatomic molecule in a position in which its polarizability is the same as initially.

So, a calculation similar to the vibration leads to the molecular dipole moment for rotation as,

$$P(t) = [\alpha_0 + \Delta\alpha \cos(2\omega_r t)]E_0 \cos\omega_0 t$$

$$\Rightarrow P(t) = \alpha_0 E_0 \cos\omega_0 t + \frac{1}{2}\Delta\alpha E_0 \cos\{(\omega_0 + 2\omega_r)t\} + \frac{1}{2}\Delta\alpha E_0 \cos\{(\omega_0 - 2\omega_r)t\} \quad \ldots\ldots\ldots (3.17)$$

The first term of this is associated with Rayleigh scattering and following terms are responsible for anti-Stokes and Stokes scattering, respectively. Now, $\Delta\alpha \neq 0$ is prerequisite for a molecular rotation to be Raman active. From the relation, $\Delta\alpha = \alpha_{\parallel} - \alpha_{\perp}$, it can be inferred that spherical rotors are not Raman active. Before looking for a rotational Raman effect in liquids, it is worthwhile to note that the frequencies of molecular collisions are more frequent than those of the rotation. Molecular rotation does not exist in case of solids because of intermolecular interaction [Gupta *et al.*, 1984, Ferraro *et al.*, 1985].

The simple derivation above is applicable to the case of a diatomic molecule. Most organic and inorganic molecules are more complicated in nature and, because the field and dipole moments are vector quantities, the polarizability takes the form of a tensor. The Equation 3.12 ($P(t) = \alpha E(t)$) then can be expressed in a matrix form:

$$\begin{bmatrix} P_x \\ P_y \\ P_z \end{bmatrix} = \begin{bmatrix} \alpha_{xx} & \alpha_{xy} & \alpha_{xz} \\ \alpha_{yx} & \alpha_{yy} & \alpha_{yz} \\ \alpha_{zx} & \alpha_{zy} & \alpha_{zz} \end{bmatrix} \begin{bmatrix} E_x \\ E_y \\ E_z \end{bmatrix} \quad \ldots\ldots\ldots (3.18)$$

where the polarizability matrix represents what is know as the polarizability tensor [Ferraro *et al.*, 1985]. If any of the components of the tensor change during the vibration, then the vibration is said to be the Raman active.

3.3.2. Vibrational Degree of Freedom and Raman Selection Rule

A molecule consisting of N atoms has 3-N degrees of freedom, which includes six collective translational and rotational degrees of freedom along and about the 3 coordinate axes,

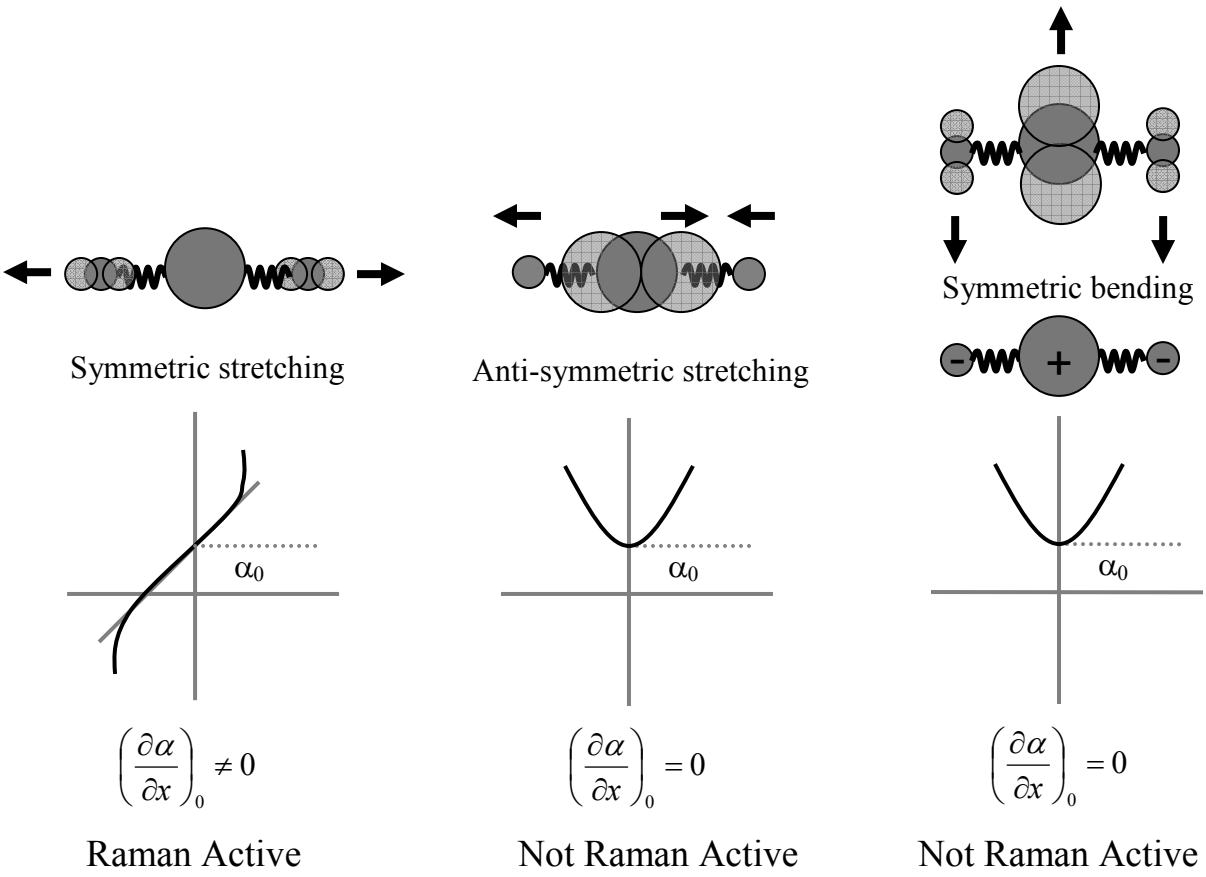

Fig. 3.12: Schematics of vibrational Raman selection rule illustrating polarizability variations in the neighborhood of the equilibrium position and vibrational activities of a linear molecule like CO_2.

respectively. Thus, a typical molecule has $3N-6$ normal vibrations. Let us consider a simple molecule like CO_2 and examine the Raman selection rule for different vibrational modes. Since a linear molecules like CO_2 have no rotation about the molecular axis, the number of independent normal vibrational modes are $3\times3-5= 4$. The normal vibrations, which occur along the atomic bonds, are shown in Figure 3.12. The general forms of dipole moments and polarizability changes with various normal coordinates are also included in the figure. According to the

classical electromagnetic derivation for a vibration to be Raman active the polarizability derivative around the equilibrium position of the molecule cannot be zero, i.e., $\left(\frac{\partial \alpha}{\partial x}\right)_0 \neq 0$. It is evident from the figure that for the symmetric stretching mode the $\left(\frac{\partial \alpha}{\partial x}\right)_0 \neq 0$, whereas for both anti-symmetric stretching and symmetric degenerate bending modes $\left(\frac{\partial \alpha}{\partial x}\right)_0 = 0$. From this it can be concluded that the symmetric stretching mode will participate in Raman scattering.

In polyatomic or more complicated molecules we can regard the total molecular polarizability as made up of contributions from individual bond polarizability that is the superposition of simple cases [Gupta *et al.*, 1984, Ferraro *et al.*, 1985].

3.3.3 Quantum Mechanical Description

Intense photon fields cause vibrational levels of the target electrons to excite to virtual states. During de-excitation most of them come back to the same vibrational level, causing Rayleigh scattering. A few of them come back to different vibrational levels, causing the Raman effect. Some of them end up in higher vibrational states causing Stokes scattering, and some of those were already in a higher vibrational states and end up in a lower vibrational state, causing anti-Stokes scattering as illustrated in Figure 3.13. The Raman effect or Raman shift is calculated from the difference in the energy levels between initial and final vibrational states as follows:

$$\Delta \tilde{\nu} = \frac{1}{\lambda_{incident}} - \frac{1}{\lambda_{scattered}} \text{ cm}^{-1} \quad \ldots\ldots\ldots (3.19)$$

where $\lambda_{incident}$ and $\lambda_{scattered}$ are the frequencies of the incident laser and the scattered beam, respectively.

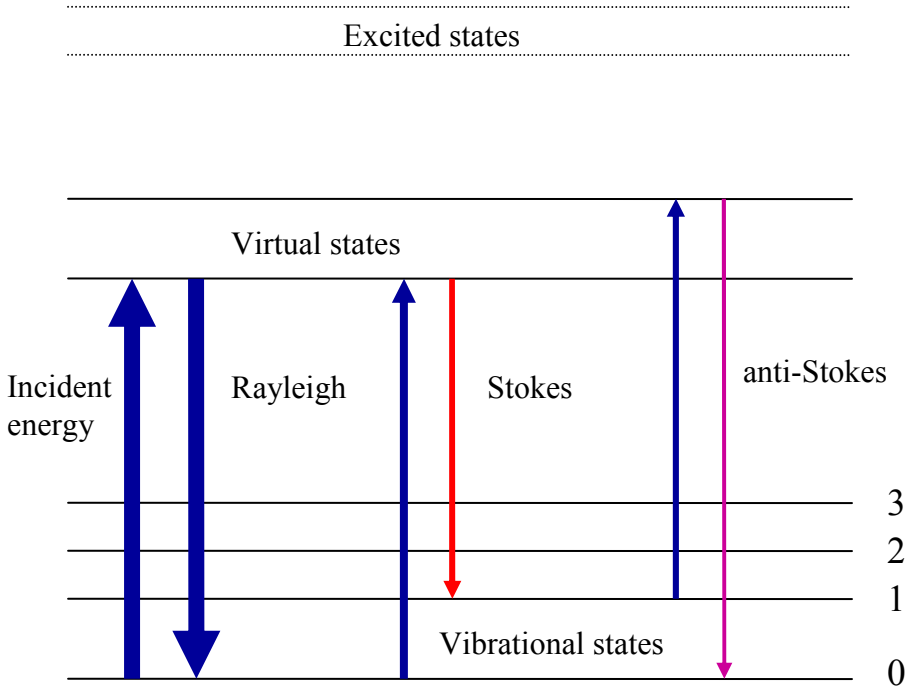

Fig. 3.13: Schematic illustration of the quantum mechanical source of Raman scattering.

3.3.4 Raman Effect in Crystal and Thin Film

For quantized lattice vibrations, the phonon is the source of Raman effect in crystalline materials. Phonons are created or destroyed during inelastic scattering between incident photons and target crystals, whereas, elastic scattering causes Rayleigh scattering. Phonons are created during Stokes scattering and annihilation of phonons occur during Anti-stokes scattering as illustrated in Figure 3.14 [Kittel, 2005].

Considering phonon frequencies, the electromagnetic derivation of the induced dipole moment, $P(t)$, can be summarized (from Equation 3.12 and Equation 3.14) as follows:

$$P(t) = \alpha E(t) = [\alpha_0 + \alpha_1 x(t)]E_0 \cos\omega_0 t = [\alpha_0 + \alpha_1 \{x_0 \cos\Omega t\}]E_0 \cos\omega_0 t$$

$$\Rightarrow P(t) = \alpha_0 E_0 \cos\omega_0 t + \frac{1}{2}\alpha_1 E_0 x_0 \cos(\omega+\Omega)t + \frac{1}{2}\alpha_1 E_0 x_0 \cos(\omega-\Omega)t \ldots\ldots\ldots (3.20)$$

where Ω is the frequency of the phonon. The first part on the right hand side of the equation causes Rayleigh scattering. The second and third parts cause anti-Stokes and Stokes scattering, respectively.

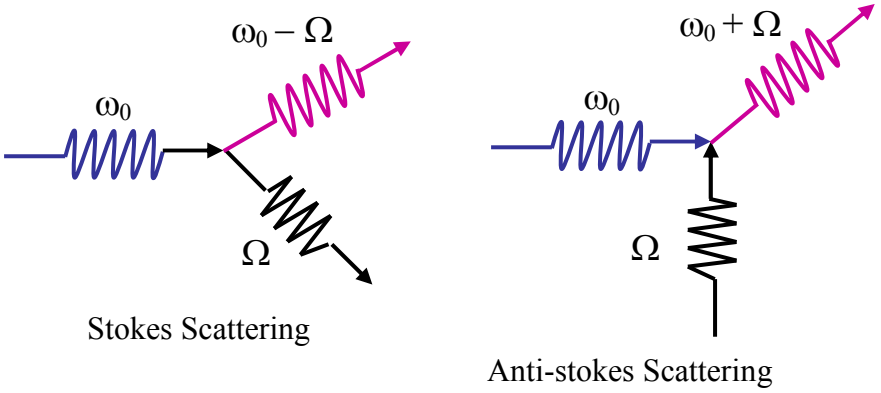

Fig. 3.14: Phonon-photon interaction in crystalline solid.

The phonon–photon interaction causes scattering characteristic of different materials. For instance, in the SiGe system, the phonon associated with Si–Si, Si–Ge and Ge–Ge bonds cause shifts in frequency of different magnitudes.

3.3.5 Instrumentation

The observation of the Raman effect requires illumination of a sample with monochromatic light and then observation of the scattered radiation at a right angle to the incident radiation. The original setup used by C.V. Raman and K. S. Krishnan in 1928 was very simple. They used sunlight as the illuminator and human eyes as the detector [Raman and Krishnan, 1928 (a,b,c), Raman, 1929]. It is incredible that the Stokes and anti-Stokes radiations, which are thousands of time less intense than the Rayleigh scattering, were observed with their experimental setup at that time. The sun is bright, but radiates isotropically over a very broad

range of wavelengths, which degrades the resolution of the system. Since then, various improvements in Raman instrumentation have taken place. It was not until 1970, when lasers became available for sample illumination, that Raman spectroscopy became popular as a materials characterization technique.

A typical Raman spectrometer consists of four major components, as shown in Figure 3.15, namely:

1. Excitation source (Laser)
2. Sample illumination and collection system (optical setup)
3. Wavelength selector (Monochromator)
4. Detection and processing system (Photomultiplier or CCD and PC)

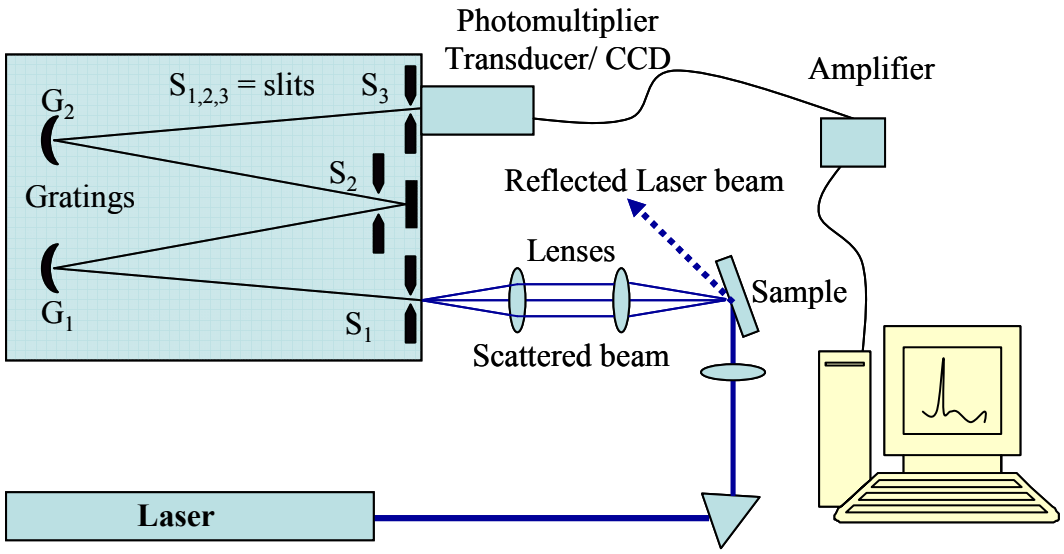

Figure 3.15: Schematic representation of Raman spectroscopy experimental setup.

The laser produces a quasi-monochromatic light that forms a very narrow band of frequencies. Lasers also produce this light in a small, concentrated beam that is very intense

[Ferraro *et al.*, 1985, and *AMS Handbook*, 1986]. The Photomultiplier tube (PMT) consists of a photocathode that emits electrons when photons strike it and thus converts photons into electric signals. The main disadvantage of the PMT is that it can be used in conjunction with the monochromator to detect photons (different energies) one color at a time. Advancements in Raman spectroscopy occurred when a charged coupled device (CCD) replaced the photomultiplier. CCD detectors are a million times more sensitive than the eye and can construct entire Raman spectra within a fraction of a second by counting all the different colors of photons simultaneously.

The output of either type of detection system is a plot of scattered-light intensity as a function of frequency shift (cm^{-1}) in which the shift is calculated relative to the laser line frequency that is assigned as zero.

The choice of laser frequency in thin film characterization depends on the types of films and substrates. Penetration depths of different laser beams of different wavelengths are summarized in Table 3.1. Laser light with a wavelength of 488 nm, which is in the visible range, is most commonly used. It has a reasonable depth of penetration for thin film analysis. Raman spectroscopic analysis of the synthesized samples was performed at the Surface Enhanced Raman Spectroscopy (SERS) laboratory at UNT.

Table 3.1: Penetration depth of different laser wavelengths in silicon and germanium.

Laser Wave Length (nm)	Penetration Depth In Si (nm)	Penetration Depth In Ge (nm)
633	3000	*32*
514	762	*19.2*
488	569	*19*
457	313	*18.7*
325	~10	*9–15*
244	*1–5*	*~7*

3.3.6 Strain Calculation of Ge_xSi_{1-x}

Considering strain, the wave number (Raman shift) associated with the phonon peaks of Si–Si, Si–Ge and Ge–Ge within the film are related as follows [Chen *et al.*, 2002]:

$$\omega_{Si-Si} = 520.2 - 62x - 815\varepsilon \ \text{cm}^{-1} \ \ldots\ldots\ldots (3.21)$$

$$\omega_{Ge-Ge} = 282.5 + 16x - 385\varepsilon \ \text{cm}^{-1} \ldots\ldots\ldots (3.22)$$

$$\omega_{Si-Ge} = 400.5 + 14.2x - 575\varepsilon \ \text{cm}^{-1} \ldots\ldots\ldots (3.23)$$

where strain ε is:

$$\varepsilon = \frac{a_{Si} - a_{in-plane}}{a_{Si}} = \frac{a_{Si} - a_{Ge_xSi_{1-x}}}{a_{Si}}$$

Since, the Raman shift is directly related to the strain and the percent relaxation is more important than the actual strain, the Raman shift can be used in the following way [Buca *et al.*, 2006, Di *et al.,* 2005]:

$$\%\,\text{Re}\,laxation = \frac{\omega_{fully-relaxed} - \omega_{\text{exp}\,erimental}}{\omega_{fully-relaxed} - \omega_{fully-strained}} \times 100\,.$$

Standard samples are used for the comparison with the phonon peaks from fully relaxed and fully strained layers of Ge_xSi_{1-x}.

3.4 References

AMS Handbook, Vol. 10, Amer. Soc. Mat. (1986)

Buca D., Feste S.F., Hollander, B., Mantl, S., Loo, R., Caymax, M., Carius, R., Schaefer, H., Solid-State Electronics **50** (2006) 32

Chen, H., Li, Y. K., Peng, C. S., Liu, H. F., Liu, Y. L., Huang, Q., Zhou, J. M., Xue, Q.K., Physical review B **65** (2002) 233303

Chu, W., Mayer, J.W., Nicolet, M.A., *Backscattering Spectrometry*, Academic Press, New York, (1978)

Di, Z., Zhang, M., Liu, W., Zhu, M., Lin, C., Chu, P. K., Mats. Sci. and Eng. B **124–125** (2005) 153

Feldman, L.C., Mayer, W. J, *Fundamentals of Surface and Thin Film Analysis*, North-Holland, New York (1986)

Ferraro, J.R., Nakamoto, K., Brown, C. W., *Introductory Raman Spectroscopy*, Aacademic Press, New York (1985)

Franssila, S., *Introduction to Microfabrication*, John Wiley & Sons, Ltd, New Jersey (2004)

Gupta S.L., Kumar, V., Sharma, R.C., *Elements of Spectroscopy,* Progati Prakashan, India (1984)

Hirvonen, J.N., Clayton, C.R., in *Surface Modification and Alloying by Laser, Ion, and Electron Beams* (Edit. by Poate, J.M., Foti, G. and Jacobson, D.C.) (1983)

Kittel, C., *Introduction to Solid State Physics*, 8th Ed., Wiley & Sons, New York, (2005)

Mayer, M., *SIMNRA User's Guide*, Report IPP 9/113, Max-Planck-Institut für Plasmaphysik, Garching, Germany (1997)

Middleton, R., *A Negative Ion Cookbook*, Department of Physics, University of Pennsylvania, Philadelphia (1989)

Raman, C. V., Nature, **123** *(*1929) 5

Raman, C. V. and K. S. Krishnan, Nature, **122** (1928a) 12

Raman, C. V. and K. S. Krishnan, Nature, **121** (1928b) 501

Raman, C. V. and K. S. Krishnan, Nature, **121** (1928c) 711

Thomson, J.J., Cambridge Philosophical Magazine, **7** (1904) 237

Usami, N., Azuma, Y., Ujihara, T., Sazaki, G., Fujiwara, K., Murakami, Y., Nakajima, K., Mats. Sci. and Eng. B **89** (2002) 364

Willams, J.S., Poate, J.M., *Ion Implantation and Beam Processing*, Academic Press, New York (1984)

Ziegler,J.F., Biersack, J. P., SRIM/TRIM (Version 2003), Available from: http://www.srim.org/

Ziegler, J. F., Biersack, J. P., Littmark, U., *The Stopping and Range of Ions in Solids*, Pergamon Press, New York (1985)

CHAPTER 4

THERMAL OXIDATION

4.1 Introduction

Thermal annealing is a critical process used in the manufacturing of integrated circuits (ICs). In metallurgy, *annealing* refers to the treatment of solids by slow furnace heating followed by slow furnace cooling, thereby modifying the solid's crystal structure. If the annealing is done above the re-crystallization temperature, new crystals nucleate and grow by the *Oswald ripening* process [Wilson, 1975]. Thermal annealing of semiconductors is often used to activate implanted dopants and anneal ion-induced damage. In addition, thermal processing in an oxidizing ambient is used to grow a vitreous SiO_2 layer, which plays a major role in the fabrication of Si-based integrated circuits (ICs). These oxide layers are notably used as interlayer insulators, capacitor dielectrics, masking layers for selected-area implantation, and as the gate dielectric in metal-oxide-semiconductor (MOS) field-effect transistors (FET's). In fact, the ability to grow an oxide layer on Si with a low density of interfacial defects is a prime reason that Si enjoys such a preeminent position in microelectronics

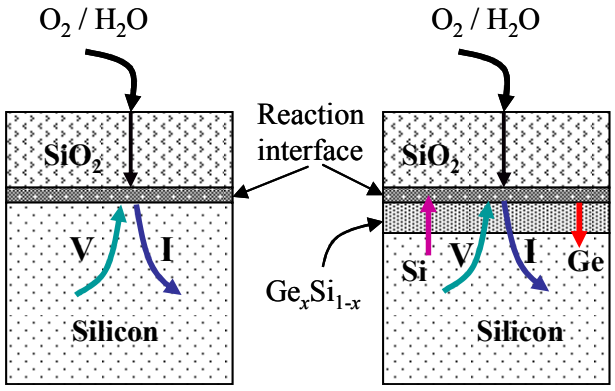

Fig. 4.1: Schematic illustration of oxidation process.

Thermal oxides, grown at high temperatures in an oxidizing ambient, lead to the formation of a vitreous SiO_2 layer on Si, as

indicated in Figure 4.1. Oxide growth occurs by the diffusion of the oxidizing specie (O_2 in dry and H_2O in wet ambient) through the SiO_2 network. At the SiO_2/Si interface, it reacts with Si to form SiO_2 [Frank *et al.*, 1984] as given by the following reactions:

$$Si\ (s) + 2H_2O\ (g) \rightarrow SiO_2\ (s) + 2H_2\ (g) \qquad \text{[Wet Oxidation]}$$

$$Si\ (s) + O_2\ (g) \rightarrow SiO_2\ (s) \qquad \text{[Dry Oxidation]}$$

Either reaction yields a unit increase in the oxide thickness during growth with the consumption of 0.44 units of the underlying Si substrate. Also, the molar volume mismatch between the Si and SiO_2 leads to a compressive strain of approximately 500 MPa in the oxide at the interface [Holland *et al.*, 1987, Fitch *et al.*, 1989]. This can be relieved by visco-elastic flow within the vitreous SiO_2, and/or by the injection of silicon self-interstitials (I) from the SiO_2/Si interface into the bulk silicon or conversely the flow of the vacancies (V) in the opposite direction [Frank *et al.*, 1984], as illustrated with the Figure 4.1. The basic unit of silica is a SiO_4 tetrahedral formed by Si bonded with four oxygen atoms, as illustrated in Figure 4.2. Thermally grown oxides are glassy and exhibit short-range order. Although the atomistic mechanism of oxidation at the monolayer level is still actively studied, Deal and Grove [1965] successfully modeled the kinetic equations of thermal oxidation using macroscopic chemical rate equations and Fick's law of diffusion [Fick, 1855]. The general equations of thermal oxidation of silicon are elaborated in the following section.

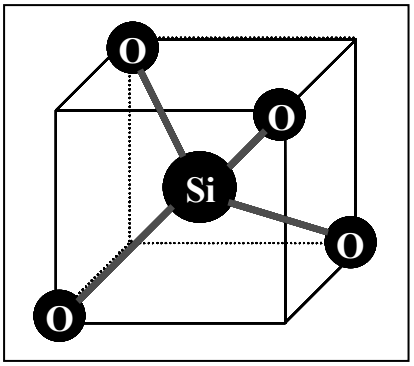

Fig. 4.2: Illustration of silica structure.

4.2 Deal and Grove Oxidation Model

While, the growth kinetics and mechanisms of Si oxidation have been extensively studied [Holland *et al.*, 1987, Fathy *et al.*, 1987, Kobeda and Frene, 1988, Legoues *et al.*, 1989 (a,b), and Deal and Grove, 1965], the Deal and Grove [1965] model continues to provide the most commonly used method for determining oxidation kinetics in Si. Their model assumes that oxidation occurs by three simple steps including (a) transport of oxidants (O_2 and/or H_2O) in gaseous phase to the silicon surface where they are absorbed, (b) diffusion through the growing oxide to the SiO_2/Si interface, and (c) react with Si to form the SiO_2. The following discusses these steps and how they lead to a description of the kinetics of thermal oxidation.

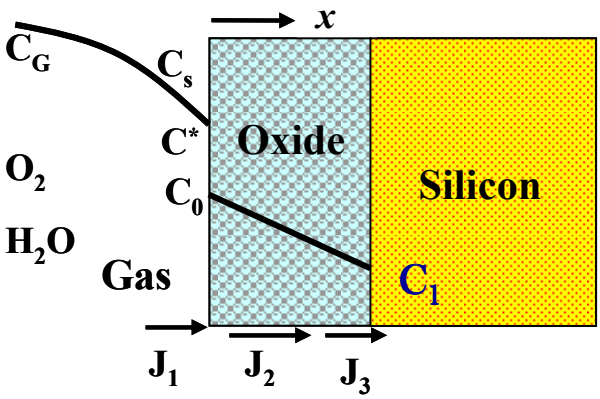

Fig. 4.3: Schematic illustrating model for silicon oxidation.

(a) Gas phase transport:

The transport of oxidant from the ambient to the surface of the solid is given by

$$J_1 = h\left(C^* - C_0\right) \ldots\ldots (4.1)$$

where J_1 is the gas phase flux of oxidant from gaseous phase to solid surface vicinity, h is the gas-phase transport coefficient, and C_0 and C^* are the concentration of the oxidant at the outer surface of oxide and in the gas phase in the vicinity of the surface, respectfully. When $J_1 = 0$, the

concentration $C_0 = C^*$, where C^* is the equilibrium concentration of oxidants in the absence of transport through the surface. C_s (as shown in the Figure 4.3) is concentration of oxidants in gas phase.

(b) Diffusion through oxides:

Normal Fickian diffusion [Fick, 1855] of the oxidant occurs within the oxide, yielding a flux given by

$$J_2 = -D\frac{\partial C}{\partial x} \cong D\frac{(C_0 - C_1)}{x} \ldots\ldots\ldots (4.2)$$

where D is the effective diffusion coefficient, x is the thickness of the growing oxide layer, and, $\frac{\partial C}{\partial x}$ is the concentration gradient of oxidants across the oxide layer, and C_1 is the concentration of oxidant near the silicon-oxide interface.

(c) Interfacial reaction:

The flux associated with the interfacial reaction is given simply by

$$J_3 = kC_1 \ldots\ldots\ldots (4.3)$$

where k is the reaction rate constant of a first order flux relation. Complete reaction of all oxidants arriving at the interface is assumed.

At steady state (when $J_1 \neq 0$), the relationship between these three fluxes is given by

$$J_1 = J_2 = J_3$$

$$\Rightarrow h(C^* - C_0) = D\frac{(C_0 - C_1)}{x} = kC_1 \ldots\ldots\ldots (4.4)$$

By solving C_1 and C_0 (the detail of which is provided in the appendix) the flux of the process can be written as,

$$J_1 = J_2 = J_3 = J = \frac{kC^*}{1 + k/h + kx/D} \ldots\ldots\ldots (4.5)$$

Now, the growth rate of oxide film, dx/dt can be describe by the following equation,

$$\frac{dx}{dt} = \frac{J}{N} \ldots\ldots\ldots (4.6)$$

where N is the number of oxidant molecules associated with the unit volume of the oxide film.

$$\Rightarrow \frac{dx}{dt} = \frac{kC^*/N}{1 + k/h + kx/D}$$

$$\Rightarrow dx + \frac{k}{h}dx + \frac{k}{D}xdx = \frac{kC^*}{N}dt \ldots\ldots\ldots (4.7)$$

The solution requires that the above equation must be integrated with following boundary condition: at $t = 0$, $x = x_i$ (i.e., x_i is the thickness of the pre-existing oxide layer and oxidation starts with the diffusion of oxidants through the oxide layer to be consumed at the silicon-oxide interface). Integration yields

$$x^2 + Ax = Bt + x_i^2 + Ax_i \ldots\ldots\ldots (4.8)$$

$$\Rightarrow \frac{x^2 - x_i^2}{B} + \frac{x - x_i}{B/A} = t \ldots\ldots\ldots (4.9)$$

where $B = \frac{2DC^*}{N}$ is the parabolic rate constant and $\frac{B}{A} = \frac{C^*}{N\left(1/k + 1/h\right)} \cong \frac{C^*k}{N}$ is the linear rate constant. Further simplification leads to

$$x^2 + Ax = B\left(t + \frac{x_i^2 + Ax_i}{B}\right)$$

$$\Rightarrow x^2 + Ax = B(t + \tau) \ldots\ldots\ldots (4.10)$$

where $\frac{x_i^{\,2} + Ax_i}{B} \equiv \tau$, which corresponds to a shift in time co-ordinate due to a pre-existing oxide layer at $t = 0$. Now, if only the positive solution of the above quadratic equation is considered (since there can be no negative oxide layer thickness), we can write the oxide thickness as a function of oxidation time as:

$$x = \frac{-A + \sqrt{A^2 + 4B(t+\tau)}}{2}$$

$$\Rightarrow x = \frac{A}{2}\left\{\sqrt{\left(1 + \frac{t+\tau}{A^2/4B}\right)} - 1\right\} \ldots\ldots\ldots (4.11)$$

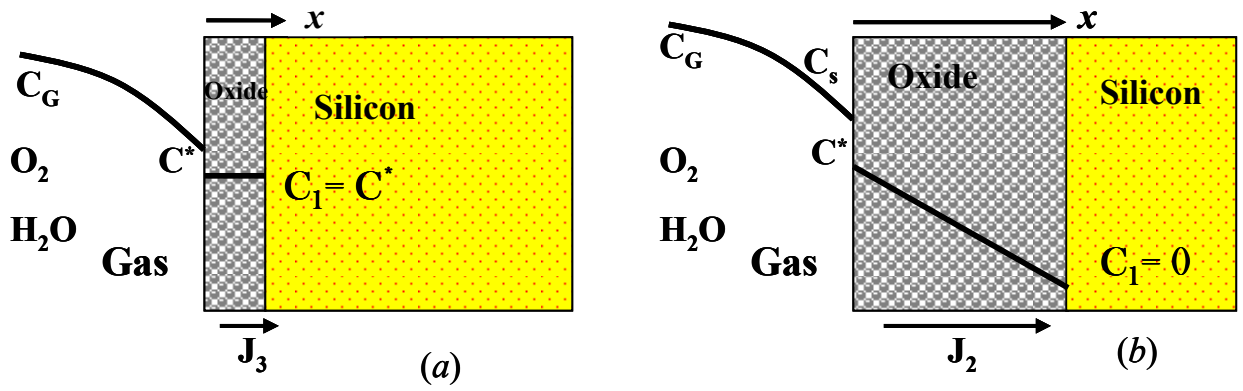

Fig. 4.4: Oxidation model illustrating two extreme cases; (*a*) linear (*b*) parabolic.

Consider the following two limiting cases of Equation 4.11:

(1) During the early stages of oxidation, i.e., $t << A^2/4B$ and $kx/D << 1$, This situation, shown schematically in Figure 4.4(*a*), leads the Equation 4.11 to the following simplified rate equation,

$$x \cong \frac{B}{A}(t+\tau) \ldots\ldots\ldots (4.12)$$

Thus, the relationship between oxide thickness, x, and oxidation time, t, reduces to a linear relation for growth of thin oxides. The combined constant, B/A, which does not depend upon oxidant diffusivity, is commonly referred to as the *linear* rate constant. In the linear regime, the oxidation kinetics is not limited by oxidant diffusion through the oxide but rather by the reaction kinetics at the oxide/Si interface.

(2) At longer oxidation times, i.e., $t >> A^2/4B$ and also $t >> \tau$, where $kx/D >> 1$, which makes $C_1 \approx 0$. This situation, which is shown schematically in Figure 4.4 (*b*), leads to the following,

$$x \cong \frac{A}{2}\left(\frac{t}{A^2/4B}\right)^{1/2}$$

$$\Rightarrow x^2 \cong Bt \quad \ldots\ldots\ldots \quad (4.13)$$

Thus, the general relation between oxide thickness, x, and oxidation time, t, reduces to a parabolic relation. The constant B depends upon the oxidant diffusivity and is referred to as *parabolic* rate constant. In the parabolic regime, the oxidation kinetics is limited by oxidant diffusion through the oxide, as is expected for thicker oxides.

Thus, two different regimes of growth are generally identified [Sze, 1983]; a linear regime where $t << A^2/4B$, which leads to the relation $x = B/A(t+\tau)$ and a parabolic regime when $t >> A^2/4B$, which gives $x^2 = Bt$. In the linear regime, the oxide growth is limited by the SiO_2/Si interface kinetics while in the parabolic regime, the growth rate is controlled by the diffusion of the oxidant through the oxide. The activation energy on the diffusion rate constant, B, is dependent upon the oxidation conditions, i.e., dry, wet or steam oxidation. The interfacial

rate constant B/A has activation energy similar to the energy required for breaking Si−Si bonds and is the same for both dry and wet conditions.

In the absence of a pre-existing oxide, Equation 4.10 can be simplified with considering the various limiting cases. Thus, the rate for τ =0 reduces to

$$x^2 + Ax = Bt \quad \text{, with t} \to 0,\ x_i \to 0$$

$$\Rightarrow x = B\frac{t}{x} - A \ldots\ldots\ldots (4.14)$$

This is an important relationship since it suggests a method for experimentally determining the various constants such as A and B. A simple x vs. t/x plot of the experiment data yields B as the slope and $-A$ as the x-intercept (Y-axis interface).

Both oxidant diffusion and the interfacial reaction are thermally activated processes which can be expressed by a simple Arrhenius relationship [IUPAC Goldbook definition, 1997] given as $B = A_0 e^{-\frac{E_a}{RT}}$

$$\Rightarrow \ln(\frac{B}{A_o}) = -\frac{E_a}{R}\frac{1}{T} + C \ldots\ldots\ldots (4.15)$$

where, E_a is the activation energy, A_o the pre-factor, R is the gas constant and T is the temperature. So, the activation energy of the associated process can be evaluated from the Arrhenius type plot of $\ln(B/A)$ as a function of inverse temperature ($1/T$) of the process. This method will be used later to determine the activation energy of the interfacial reaction.

4.3 Thermal Oxidation of Ge-ion Implanted Silicon

4.3.1. Introduction

Development of high-performance devices fabricated using novel devices/materials such as SiGe Heterostructure Bipolar Transistor (HBT) [Dunn *et al.*, 2003] in Strained-Silicon-on-Insulator (SSOI) depends, in part, on a better understanding of oxidation kinetics, especially in SiGe alloys. The dependence of the kinetics on Ge concentration, oxidation ambient and temperature are crucial in developing processes to yield the desired oxide thickness with a low-defect-density interface for enhanced carrier mobility and low power consumption.

Several authors have reported the dependency of the oxidation rates on impurity levels. For example, a rate enhancement was noted [Holland *et al.*, 1987, Ho and Plummer, 1979, Gotzlich *et al.*, 1980] for thermal oxidation of heavily doped, P, Sb, Ge, while a decrease [Josquin, 1980] in oxidation rates due to the presence of nitrogen was observed. Tételin *et al.* [1998] considered low temperature atomic-oxygen assisted oxidation of SiGe. Although different groups have reported on the thermal oxidation of highly doped silicon [Colonna *et al.*, 2003] and epitaxially grown SiGe [Garrido *et al.*, 1999, Spadafora *et al.*, 2003, Olsen *et al.*, 2004], the mechanism for the kinetic enhancement in Ge-ion implanted silicon is not yet fully resolved. For instance, LeGoues *et al.* [1989] seem to attribute strain at the Si/SO_2 interface as the source of the kinetic enhancement although their analysis could not account for the differences between wet and dry oxidation.

It has previously been demonstrated [Holland *et al.*, 1987, Fathy *et al.*, 1987] that implanted Ge in Si is totally rejected during oxidation by the growing oxide. This segregation of the Ge produces a "snow-plow" effect that forms an enriched Ge layer at the Si/SiO_2 interface

and enhances the oxidation kinetics in wet O_2 [Holland *et al.*, 1987, Fathy *et al.*, 1987, Terrasi *et al.*, 2002] and possibly in dry O_2, although there is some disagreement [LeGoues *et al.*, 1989, Spadafora *et al.*, 1999 and Spadafora *et al.*, 2003]. The action of this segregated Ge on oxidation kinetics is similar to other segregated impurities in that it affects only the interfacial rate constant. However, it differs in that the dependence of the interfacial kinetics on the Ge-ion concentration is a step-function: below a critical concentration of Ge at the oxide/Si interface no enhancement is observed, while at or above this critical concentration (~80 % Ge), the interfacial reaction is increased by a fluence-independent factor [Holland *et al.*, 1987]. Kinetic enhancement and Ge accumulation at the oxide interface under wet ambient conditions at higher fluences have been reported by other groups as well [Tételin *et al.*, 1998, LeGoues *et al.*, 1989]. Nevertheless, the mechanism responsible for kinetic enhancement demands further clarification for both dry and wet conditions.

Results are presented relating to the oxidation of Ge-ion implanted Si during both wet and dry conditions, and the role of Ge in enhancing the oxidation kinetics. One of the focuses of this work was on the oxidation behavior for dry conditions, where ambiguous results have been reported [LeGoues *et al.*, 1989, Spadafora *et al.*, 2003]. The interfacial rate constant B/A was determined for different conditions to establish the effect of interfacial Ge on oxidation kinetics. Rutherford backscattering spectrometry (RBS) was used to characterize the SiO_2 and the composition of the Ge_xSi_{1-x} layers to determine the oxidation kinetics and to monitor changes in the distribution and interfacial concentration of the implanted Ge during oxidation.

4.3.2 Experimental Procedure

In the present work, *p*-type Si (100) wafers with resistivities in the range of 5-15 Ω-cm were used. Some samples were prepared using singly-charged $^{74}Ge^{+}$ ions at 80 keV with a fluence of 2×10^{16} ions/cm^2. Low-current densities (less than 1 μA/cm^2) were maintained to avoid target heating during implantations. A region was masked to retain virgin Si for comparison. To examine the fluence dependent effects some samples were also prepared by implanting Ge-ions with the energy of 70 keV with fluences ranging from 5×10^{14} ions/cm^2 to 2.4×10^{16} ions/cm^2. Oxidation was done in a standard quartz-tube furnace in either a dry O_2 ambient or wet conditions (where O_2 is bubbled through deionized (DI) water held at 95 ˚C). All samples were cleaned in a dilute HF solution (1:1 = 48% HF: DI water) and rinsed afterwards in DI water. Oxidations were done between 900 − 1100 ˚C for different time cycles. RBS measurements were used to determine the oxide thickness and the distribution of the implanted germanium. Measurements were done on both implanted and unimplanted (virgin) regions of the same sample to ensure an accurate comparison of the effects of oxidation. RBS data were acquired using 1.5 MeV He^{+} ions with a solid-state, surface-barrier detector, positioned at 135° to detect backscattered He^{+} ions. High-depth resolution RBS was used for determining the compositional change in Ge_xSi_{1-x} layer. A computer program, SIMNRA-version 6.2, was used to simulate the RBS spectra for various experimental conditions [Mayer, 1997, Mayer, 1999]. The composition and thickness of the Ge_xSi_{1-x} layers were determined from the simulation parameters that yielded the best fit to the actual spectral data.

Since no effect is expected unless the interfacial Ge concentration is above a critical value, samples were specifically prepared with a high surface concentration. This is important for dry O_2 conditions were the interfacial reaction is the rate-limiting step for only a short period,

i.e., for very thin oxide layers. If the critical Ge concentration is not present during this time, then no effect is expected. The following multi-step method of sample preparation was used. As-implanted samples were initially oxidized at 1050 ˚C for 1 hour to completely segregate the implanted Ge into a layer at the oxide interface. The oxide layer was then carefully removed by wet etching in a dilute HF-bath. The etched sample was then evaluated to determine the composition of the segregated layer. High-depth resolution RBS determined the layer (now at the surface) to be $Si_{0.7}Ge_{0.3}$. These samples were then used in the experiments to determine the dry oxidation kinetics. Due to the trend of down-sizing of electronic devices, the linear regime for growth of thin oxides was a focus of the present study.

4.3.3 Results and Discussion

The oxidation kinetics were determined using RBS to monitor the thickness of the oxide layer as a function of oxidation conditions. RBS spectra from virgin and Ge-ion implanted samples after wet oxidation at 900 ˚C for 1 hour are compared in Figure 4.5. The position of the arrows for Si and O refers to the respective backscattering energy from these elements at the surface. Comparison of the scattering yield from the surface oxide indicates that it is much thicker in the implanted region than in virgin Si. This clearly demonstrates the enhancement of the oxidation kinetics by the presence of Ge. Also, the position of the scattering peak from Ge (located ahead of the Si scattering edge) is consistent with the Ge at the oxide/Si interface indicating that the implanted Ge has been segregated at the interface during oxide growth. This is seen more clearly in Figure 4.5 by movement of the Ge profile with continuing oxidation (e.g., 5 min to 60 min). Clearly, this is the result of nearly complete segregation of Ge into the underlying Si during oxidation.

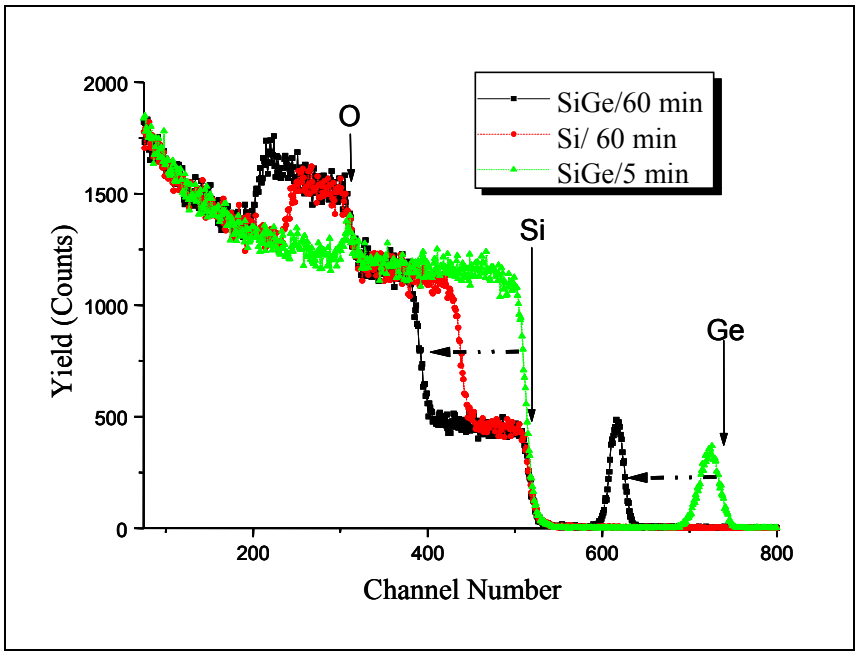

Fig. 4.5: RBS spectra from a virgin Si and Ge+-implanted samples comparing the oxide thickness grown during wet oxidation at 900 ˚C/ 1 hr. A thicker oxide is clearly seen on the implanted sample. An implanted sample, oxidized for only 5 min, is also shown to demonstrate how the Ge peak tracks the location of the SiO_2/Si interface as the oxidation proceeds [Hossain *et al.*, 2005] (Reproduced with the permission from Elsevier).

4.3.3.1 Oxidation Kinetics vs. Fluence

The dependence of the oxidation rate on implanted fluence is shown in Figure 4.6. The figure shows that the oxidation rate is substantially affected by the Ge-ion implantation over the entire fluence range investigated. This is not in complete agreement with the initial reports [Holland *et al.*, 1987, Fathy *et al.*, 1987] of the fluence effect, which claimed that the oxidation rate was essentially constant beyond a critical fluence, corresponding to about one monolayer of Ge. The new data clearly demonstrates that there is nearly an exponential dependence on the implanted fluence of Ge (as indicated by the linear dependence of the oxidation rate on fluence on the semi-log graph.).

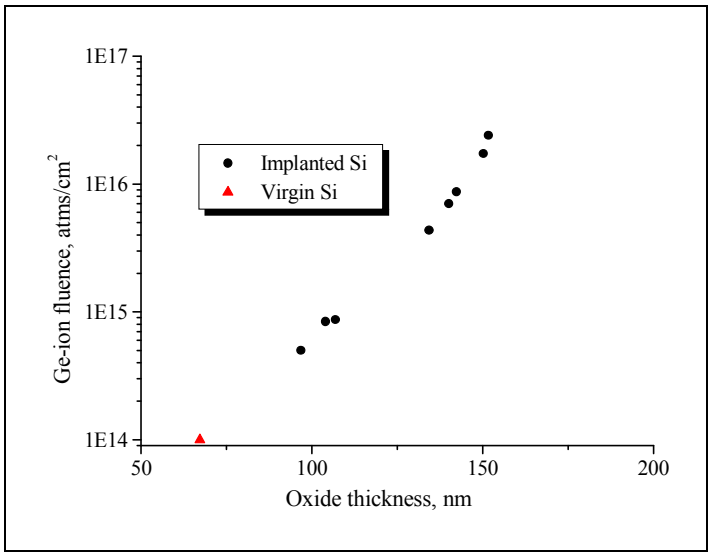

Fig. 4.6: Implantation fluence vs. oxide thickness in Si (100) implanted with 70 keV Ge-ion after wet oxidation at 900 ˚C for 30 min [Hossain *et al.*, 2007] (Reproduced with the permission from Elsevier).

Furthermore, the fluence range was chosen to span the critical thickness of the segregated Ge layer for dislocation formation. Below the critical thickness (corresponding to a fluence of ~1×10^{16} ions/cm^2), the Ge:Si layer forms commensurately, i.e., pseudomorphically, with the underlying Si substrate. Since the lattice parameter of Ge is about 4 % larger than Si, the segregated layer becomes highly strained. M. Chisholm of Oak Ridge National Laboratory (personal communication, 2002) showed that the segregated Ge films form pseudomorphically beyond this critical thickness due possibly to the effects of the overlying oxide layer. Nonetheless, he observed the onset of plastic deformation and relaxation beyond germanium fluence of ~2×10^{16} ions/cm^2. It was interesting to investigate this phenomenon above and below the critical thickness for the onset of strain relief to determine the role of strain in oxidation enhancement. However, the results in Figure 4.6 clearly indicate that the oxidation rate increases with fluence in a rather smooth manner through this critical point indicating that lattice strain does not play a role in this effect, in contrast to claims by LeGoues *et al.*. [1989].

4.3.3.2 Effects of Ge on Dry Oxidation

It should be noted that 900 ˚C dry oxidation of an as-implanted Si sample produced similar snow plowing of Ge but no enhancement of the oxidation rate. This is consistent with earlier results reported by Holland *et al.* [Holland *et al.*, 1987, Fathy *et al.*, 1987] where the absence of an enhancement was attributed to a Ge interfacial concentration lower than the critical value needed to "turn-on" the enhancement.

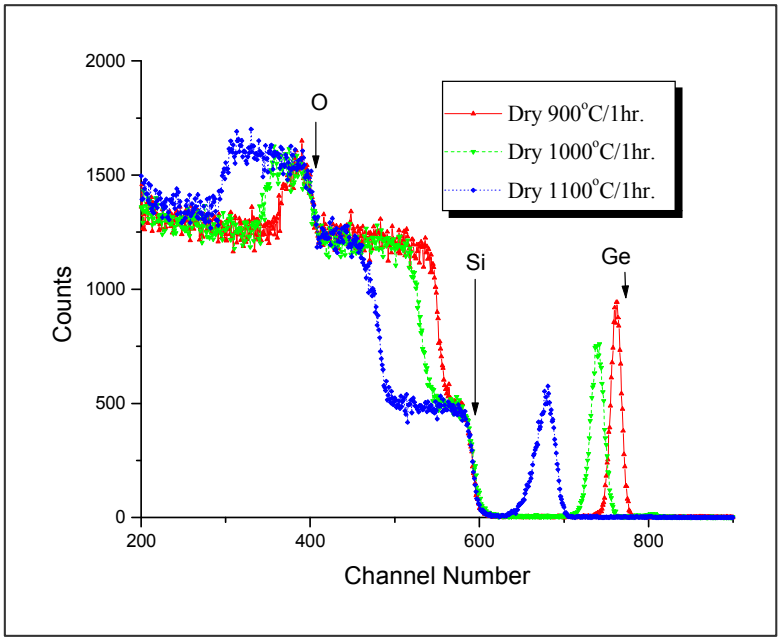

Fig. 4.7: RBS spectra of (100) Si (prepared with a high surface concentration of Ge) after dry oxidation at 900˚, 1000˚ and 1100 ˚C for 1 hr. "Snow-plowing" of the Ge is clearly seen in each spectrum indicating no incorporation of the Ge within the thermal oxide at any temperature [Hossain *et al.*, 2005] (Reproduced with the permission from Elsevier).

Dry oxidation was further investigated in this work to determine whether or not the absence of enhancement is due to the low Ge concentration at the interface or is related to a more fundamental oxidation issue (e.g., the nature of the oxidant, O_2 for dry and H_2O for wet conditions). To this end, samples were specially prepared for the dry oxidation experiments to have a 30 % Ge concentration at the surface (as described earlier in the experimental section).

The following describes the method used for preparing these samples. Samples were implanted and then oxidized in a dry O_2 ambient at different temperatures for 1 hour. RBS spectra from these samples are shown in Figure 4.7. Similar to the results in Figure 4.5, the location of the Ge peak is not fixed but is correlated to the location of the oxide/Si interface. The peak shifts to lower energy (i.e., to deeper within the sample) as the oxide thickness increases. Next, the composition of the segregated Ge layer after dry oxidization was determined using high-depth resolution RBS measurements. The spectral results from the samples after the removal of the oxides by HF solution are shown in Figure 4.8. These results show that the composition

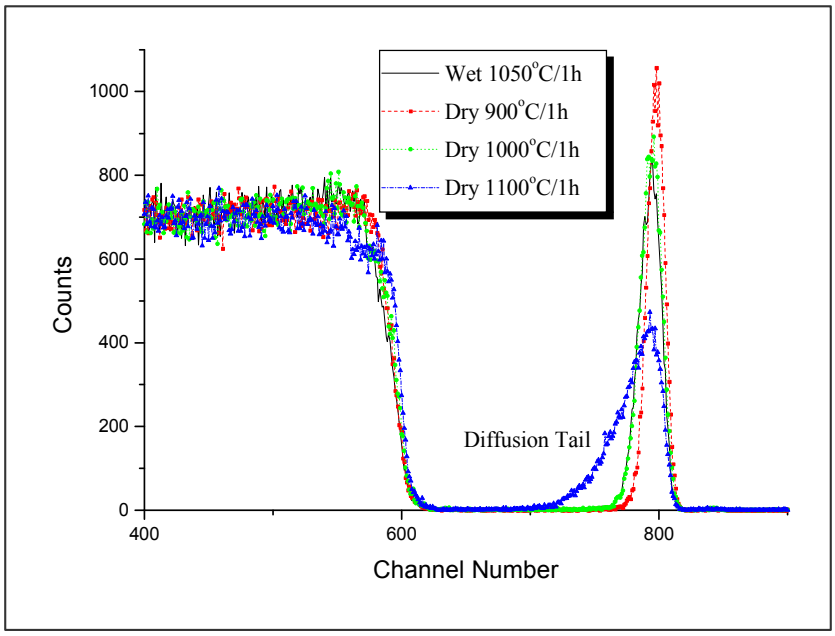

Fig.4.8: High depth resolution RBS spectra of samples previously shown in Figure 4.7. Prior to analysis, the oxide layer was removed in HF to facilitate the resolution of the $Ge_{1-x}Si_x$ composition and the diffusion profile of Ge [Hossain *et al.*, 2005] (Reproduced with the permission from Elsevier)

of the segregated layer after an hour of dry oxidation (initially $Si_{0.7}Ge_{0.3}$) became more Ge rich at the low oxidation temperatures. The Ge content in the layer increased to 80 % after 900 ˚C oxidation, and 34 % after oxidation at 1000 ˚C. The 1100 ˚C results indicate that the segregated

layer is quite diffused and no longer distinct. Therefore, samples were prepared using the 1050 ˚C for investigation of the effects of Ge on the kinetics of dry oxidation. This preparation ensures that a high Ge concentration is present so that the effect during the linear growth regime could be studied.

The kinetics of dry oxidation were determined at the three different temperatures for both implanted and virgin Si samples. The results are given in Table 4.1 expressed as the best-fit parameters to the Deal and Grove model [Deal and Grove, 1965]. Comparison of the linear rate constant B/A and the diffusion rate constant B for implanted and virgin samples at each temperature, clearly shows that the oxidation kinetics are enhanced at both 900 ˚C and 1000 ˚C (but not at 1100 ˚C). In each case, the enhancement is the result of an increase in the linear rate constant due to the presence of Ge at the interface at or above a critical concentration (~80 % Ge within a monolayer). This onset corresponds to the concentration at which the film becomes more Ge-like. The results are similar to those previously reported for steam or wet oxidation, and clearly show that the effect is present for dry conditions and may derive from a common mechanism.

Table 4.1: Rate constants for oxidation of virgin and implanted silicon in dry ambient, $x^2 + Ax = B(t + \tau)$. (B/A' is the modified linear rate constant for implanted Si)

Oxidation Temperature, ˚C	B (μm^2/h)	A (μm)	A' (μm)	B/A (μm/h)	B/A' (μm/h)
900	0.0042	0.1287	0.0293	0.0326	0.1433
1000	0.0114	0.0874	0.0509	0.1304	0.2240
1100	0.0359	0.0743	0.0743	0.4832	0.4832

4.3.3.3 Effects of Ge during Wet Oxidation

The RBS spectra in Figure 4.9 provide a comparison of the composition of the segregated Ge_xSi_{1-x} layers in wet oxidized samples at different temperatures. The spectra were

acquired using a scattering geometry chosen to maximize the depth resolution of the measurements (as explained in the experimental section). A best-fit simulated spectrum is shown for each of the different experimental conditions. The sample wet oxidized at 900 ˚C results in the formation of an almost pure (~100 %) Ge film while the composition of the film decreases to only 30 % in the sample oxidized at 1050 ˚C.

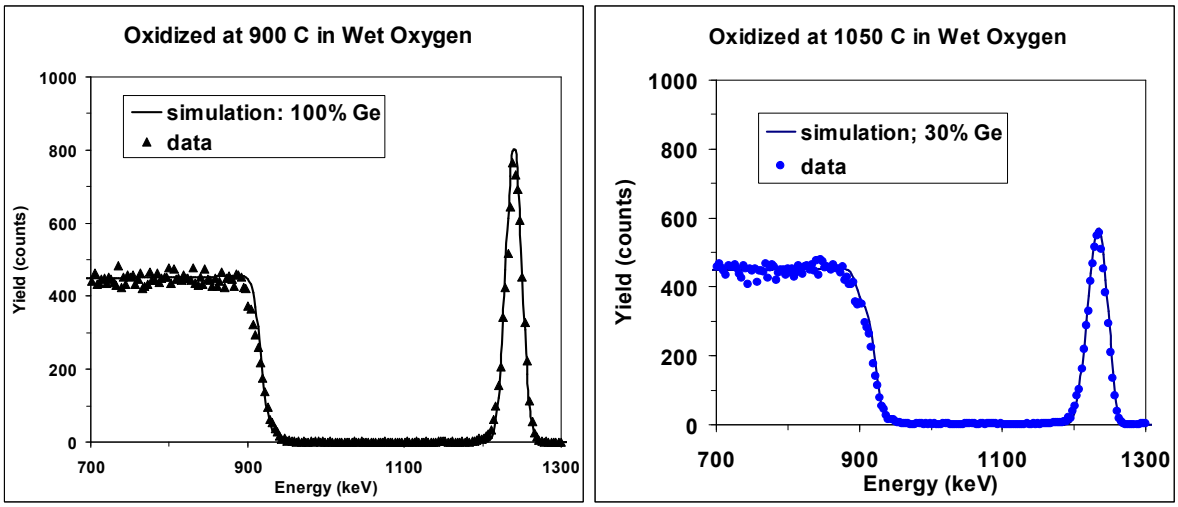

Fig. 4.9: Comparison of RBS spectra acquired from Ge^{+}-implanted Si after oxidation at 900°C and 1050°C. Compositions are determined by best-fit to simulated spectra shown for each spectral condition [Hossain *et al.*, 2007] (Reproduced with the permission from Elsevier).

Figure 4.10 shows the relative kinetic behavior of Ge-implanted silicon with respect to virgin silicon during thermal oxidation at different temperatures in wet ambient in samples implanted with germanium fluence of 2×10^{16} ions/cm^2. Rate enhancement was observed during wet oxidation over the temperature ranging 900 ˚C to 1000 ˚C. The absence of an effect at higher temperatures can be attributed to the lower Ge concentration in the segregated GeSi film. On the graph oxide thicknesses, x, is plotted as a function of t/x (t is the oxidation time). Best-linear-fit trend lines are used to extract the Deal and Grove model [Deal and Grove, 1965] parameters. The

linear and parabolic rate constants obtained from the model are presented in Table 4.2 (The similar parameters for dry oxidation have already been introduced in Table 4.1).

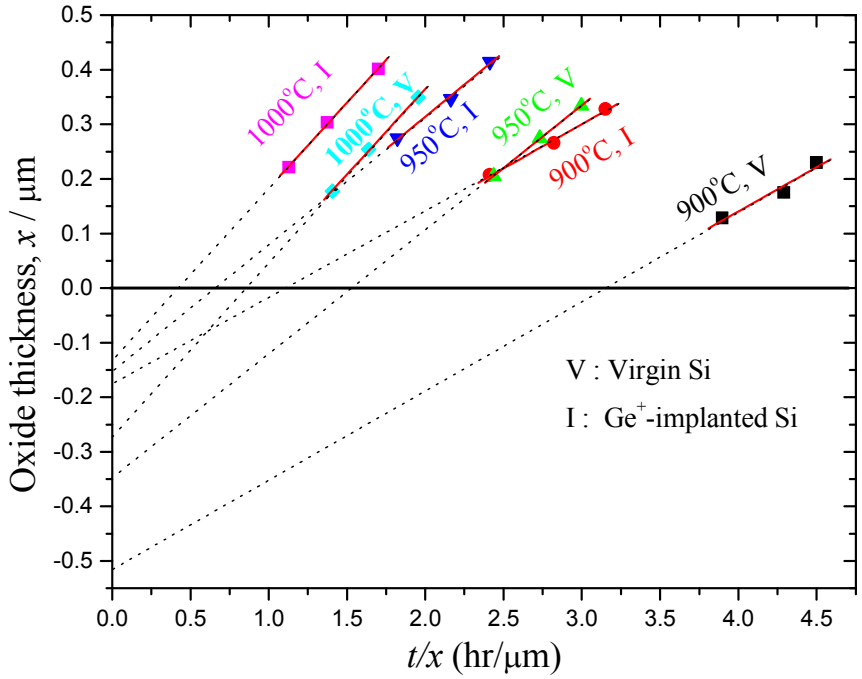

Fig. 4.10: Wet oxidation kinetics of Ge^+-implanted and virgin Si.

Table 4.2: Rate constants for oxidation of virgin and implanted silicon in wet ambient; $x^2 + Ax = B(t + \tau)$ (B/A' is the modified linear rate constant for implanted Si).

Oxidation Temperature, ˚C	B (μm^2/h)	A (μm)	A'(μm)	B/A (μm/h)	B/A'(μm/h)
900	0.1620	0.5082	0.1868	0.3188	0.8672
950	0.2300	0.3549	0.1576	0.6481	1.4689
1000	0.3131	0.2615	0.1298	1.1973	2.4122

The rate constants summarized in Table 4.1 and 4.2 have been then used to calculate the activation energy of the various processes under different oxidation conditions, i.e., wet vs. dry. The results are summarized in the following figures. The uncertainties of the figures are related to RBS results and the best-fit SIMNRA simulations, and are within ± 5 %.

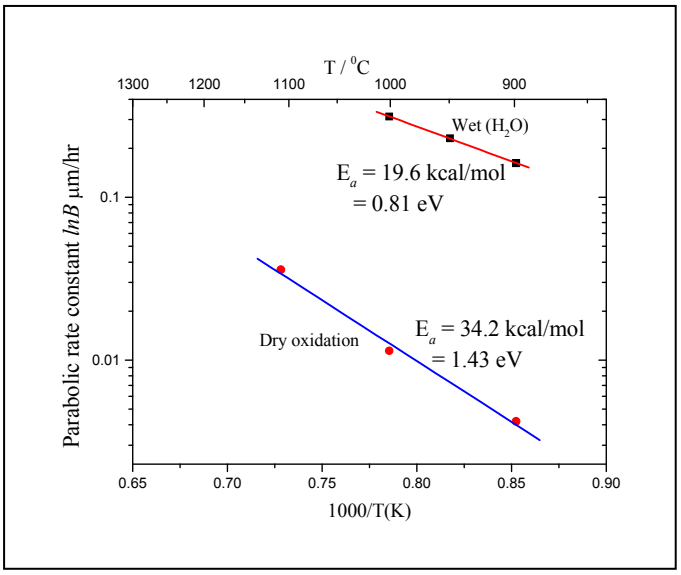

Fig. 4.11: Arrhenius plots of parabolic rate constants of virgin Si (100) for dry and wet ambient.

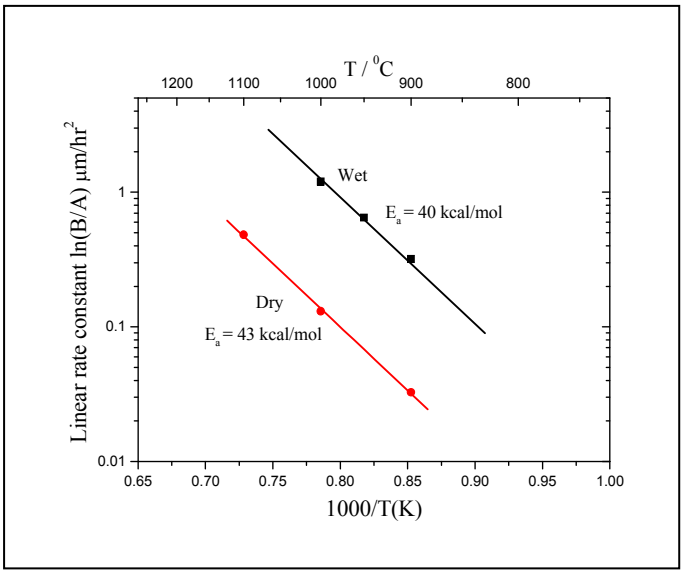

Fig. 4.12: Arrhenius plots of linear rate constants of virgin Si (100) for dry and wet ambient.

Figure 4.11 shows that the parabolic rate constant falls with inverse temperature during thermal oxidation of virgin silicon as described by the Deal and Grove model. The slopes indicate the activation energies for dry and wet oxidations as 1.43 eV and 0.81 eV respectively. The corresponding results reported by Deal and Grove [1965] were 1.23 eV for dry oxidation and 0.78 eV wet condition. The activation energies for diffusion of O_2 and H_2O in fused silica are 1.18 eV and 0.78 eV respectively [Ghandhi, 1983]. Our results agree favorably with the diffusion of oxygen and H_2O in silica, and confirm that the parabolic rate constant is related to the diffusion of oxidants through the growing oxide layer. Figure 4.12 shows that logarithm of linear rate constant (*ln(B/A)*) also falls with inverse temperature (1/*T*) at a slope of 40 kcal/mol (1.71 eV) for wet oxidation of virgin

silicon. The corresponding slope for dry oxidation is 43 kcal/mol (1.81 eV). The results are, on average, in a close agreement with the energy required to break a Si−Si bond (42.2 kcal/mol) [Hess and Deal, 1977, Pauling, 1967]. This suggests that the rate limiting process associated with the interfacial oxidation reaction is simply bond breaking. An Arrhenius plot for wet oxidation is presented in Figure 4.13, which compares results for implanted and virgin Si. The results clearly indicate a decrease in the linear rate constant in the implanted sample.

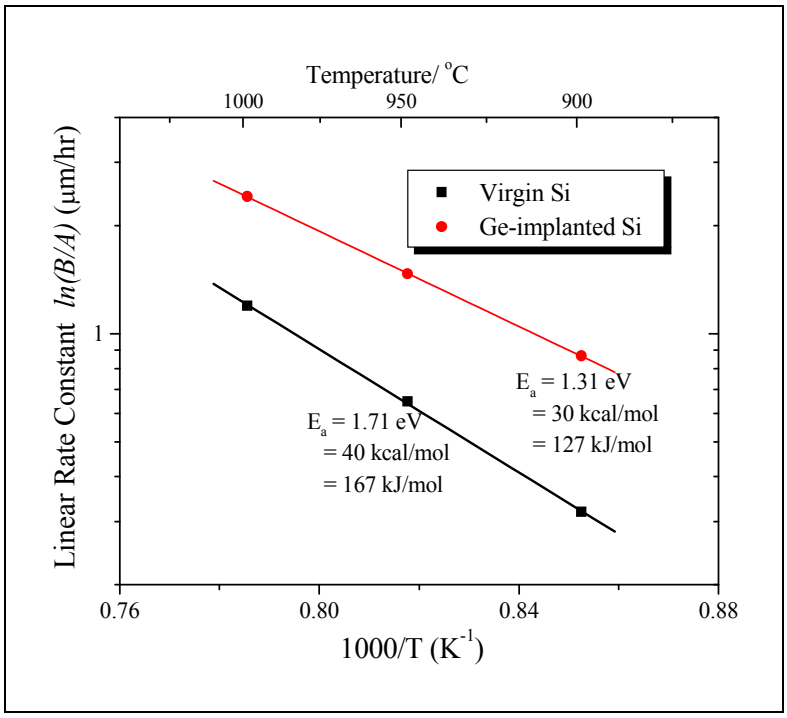

Fig. 4.13: Arrhenius plots of linear rate constants of Ge-ion-implanted and virgin Si (100) for wet oxidation.

Activation energies of linear rate constants under dry conditions are shown in Fig. 4.14. The slope of the *ln*(*B/A*) vs. *1/T* data yields a value of 27.5 kcal/mol (1.16 eV) (using a linear fit with ±10 % standard deviation). The result is in good agreement with the Ge–Ge bond energy [Average bond-dissociation energy for Ge−Si is 36 kcal/mol (1.52 eV) and Ge−Ge is 33

kcal/mol (1.39 eV) (extracted from the standard state enthalpy of formation (ΔH_{f298}) value)] [Speight, 2005].

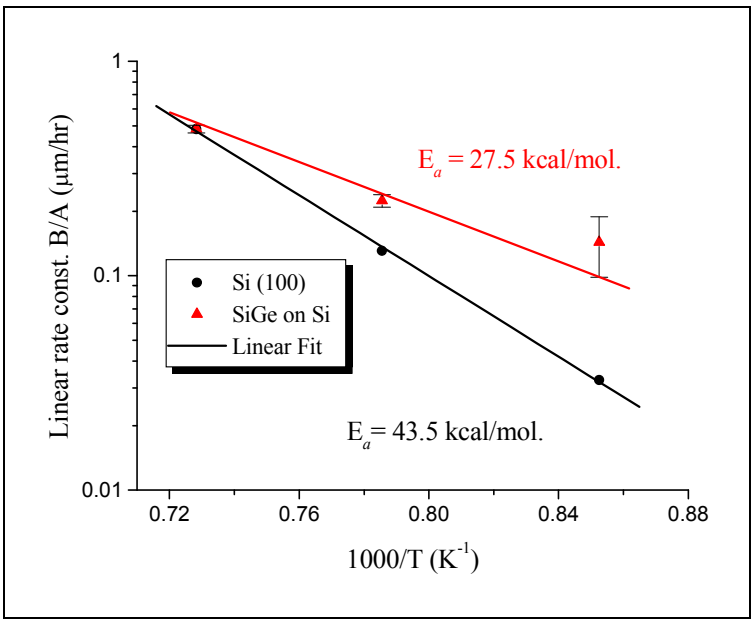

Fig. 4.14: Arrhenius plots versus temperature from which activation energies for both virgin and implanted silicon are derived by using the respective Deal and Grove model parameters achieved after dry oxidation [Hossain *et al.*, 2007] (Reproduced with the permission from Elsevier).

Comparative Arrhenius plots for implanted silicon in both dry and wet oxidation conditions are represented in Figure 4.15. On average they resolve almost the similar amount of activation energy, which in a close agreement with the energy required to break the Ge−Ge bonds. As depicted in Figure 4.12, the interfacial rate constant is similar during both dry and wet oxidation. Both results in similar slopes, i.e., require same amount of energy to activate the oxidation reaction. Thus, it can be concluded from these experimental results that Ge-implanted silicon oxidizes with a similar interfacial mechanism in both dry and wet atmospheres and requires almost the same activation energy, which is related to the Ge−Ge bond energy. Of course, oxidation occurs faster during wet rather than dry oxidation of Ge-ion implanted silicon

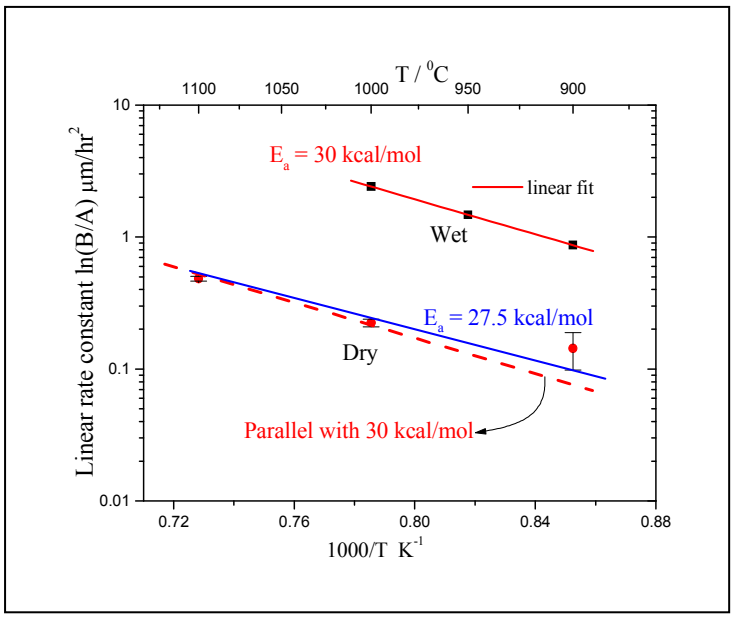

Fig. 4.15: Comparative Arrhenius plots of linear rate constants resolving activation energies of Ge^+-implanted Si for thermal oxidation in dry and wet ambient.

similar to that found in the virgin one. This is however related to higher equilibrium concentration of H_2O that that of O_2 in the oxide [Deal and Grove, 1965].

4.3.3.4 Simulation of Ge Profiles during Oxidation

Lastly, Figure 4.16 and 4.17 present the results of computer simulation of the Ge segregation process during oxidation. The simulation uses an as-implanted profile generated by another simulation routine, SRIM [Ziegler *et al.*, 1985]. The oxidation process is simulated using intrinsic rates from the Deal and Grove model (i.e., no attempt was made to model the kinetic enhancement). The details of the program are given by O. W. Holland [1989]. The simulation data in Figure 4.16 give the interfacial concentration of Ge as a function of the oxide thickness. This is shown for three different oxidation temperatures. Initially there is no Ge at the interface since the as-implanted profile is peaked below the surface. As the oxidation process

progresses, the interfacial Ge concentration increases to a maximum value. At 920 ˚C, a nearly pure Ge layer is formed at ~0.06 microns, which persists over the entire simulated growth process. This result strongly suggests that dry oxidation at this temperature should produce a high-concentration of Ge at the interface, as was observed experimentally. At 1000 ˚C, the Ge concentration peaks at ~0.1 microns but decreases for thicker oxides due the interdiffusion with the Si substrate, while the concentration remains relatively low at 1100 ˚C for all oxidation times. The 1000 ˚C results indicate that it is possible to achieve high Ge concentrations at the interface for short periods of time. Again, this is consistent with the experimental results that showed the kinetics to be enhanced at this temperature. Moreover, computer simulation data for the wet oxidation process are presented in Figure 4.17. It is evident from the simulations for wet

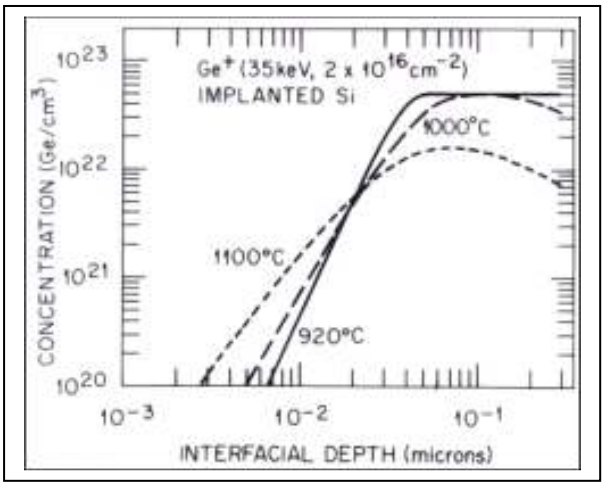

Fig. 4.16: Computer simulation of dry oxidation in Ge^+-implanted Si at different temperatures. [Hossain *et al.*, 2005] (Reproduced with the permission from Elsevier).

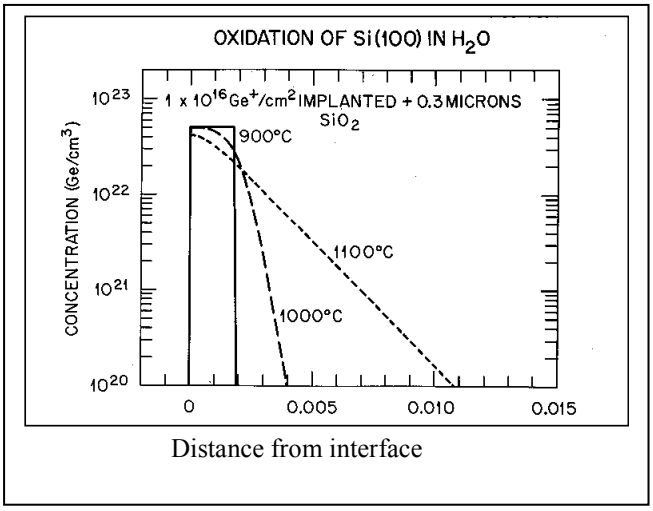

Fig. 4.17: Computer simulation of wet oxidation in Ge^+-implanted Si at different temperatures. [Hossain *et al.*, 2007] (Reproduced with the permission from Elsevier).

oxidation between 1000 °C-1100 °C that the Ge concentration falls well below 100 %, consistent with experimental observation.

4.3.4. Conclusions

Both dry and wet oxidation rates were enhanced over their intrinsic values in Ge-ion implanted Si at both 900 ˚C and 1000 ˚C. The snow plowing of Ge during dry oxidation was shown to be similar to that reported under wet conditions. Furthermore, it was determined from the measurement of kinetic parameters that the enhancement was the result of a modified interfacial reaction. Computer simulation of the segregation process indicated that it is possible to achieve a high interfacial concentration of Ge at either 920 ˚C or 1000 ˚C during dry oxidation. This suggests that enhanced oxidation rates could be achieved under appropriate conditions. A systematic study, covering thermal oxidation over a wide range of Ge-ion fluences also reveals that kinetic enhancement is due to changes in interfacial reactions associated with the lower Ge−Ge binding energy. Highly Ge-rich layer formation at the reaction interface, related to the oxidation condition, plays an important role in rate enhancement. Oxide growth rate enhancement over virgin silicon can be achieved by proper tuning of fluence and oxidation conditions.

4.4 References

Colonna, S., Terrasi, A., Scalese, S., Iacona, F., Raineri, V., Via, F. L., Mobilio, S., Surface Science **532-535** (2003) 746

Deal, B.E., Grove, A. S., J. Appl. Phys. **36** (1965) 3770

Dunn, J. S., Ahlgren, D. C., Coolbaugh, D. D., Feilchenfeld, N. B., Freeman, G., Greenberg, D. R., Groves, R. A., Guarín, F. J., Hammad, Y., Joseph, A. J., Lanzerotti, L. D., St.Onge, S. A., Orner, B. A., Rieh, J.-S., Stein, K. J., Voldman, S. H., Wang, P.-C., Zierak, M. J.,

Subbanna, S., Harame, D. L., Herman, D. A., Meyerson, B. S., IBM J. Res. & Dev. **47** (2003) 101

Fathy, D., Holland, O.W., White, C.W., Appl. Phys. Lett. **51** (1987) 1337

Fick, A., *Phil. Mag.* **10** (1855) 30

Fitch, J. T., Lucovsky, G., Kobeda, E., Irene, E. A., J. Vac. Sci. Technol. B **7** (1989) 153

Frank, W., Gösele, U., Mehrer, H., Seeger, A., in: G.E. Murch, A.S. Nowick (Eds.), *Diffusion in Crystalline Solids*, Academic Press, Florida (1984) 95

Garrido, B., Cuadras, A., Bonafos, C., Morante, J.R., Fonseca, L., Franz, M., Pressel, K., Microelectron. Eng. **48** (1999) 207

Ghandhi, S.K., *VLSI Fabrication Principles*, John Wiley & Sons, New York (1983)

Gotzlich, J.F., Haberger, K., Ryssel, H., Kranz, H., Traumuller, E., Radiat. Eff. 47 (1980) 207

Hess, W., Deal, B.E., J. Electrochem. Soc. **124** (1977) 735

Ho, C.P., Plummer, J.D., J. Electrochem. Soc. **126** (1979) 1516

Holland, O.W., White, C.W., Fathy, D., Appl. Phys. Lett. **57** (1987) 520

Holland, O.W., Appl. Phys. Lett. **54** (1989) 320

Hossain, K., Savage, L.K., Holland, O.W., Nucl. Instr. and Meth. Phys. Res. B **241** (2005) 553

Hossain, K., Holland, O.W., Naab, F., Mitchell, L.J., Poudel, P. R., Duggan, J.L., McDaniel, F.D., Nucl. Instr. and Meth. Phys. Res. B **261** (2007) 620

IUPAC Goldbook definition, *IUPAC Compendium of Chemical Terminology*, 2nd Ed. (1997)

Josquin, W.J.M.J., Radiat. Eff. **47** (1980) 221

Kobeda, E., Frene, E.A., J. Vac. Sci. Technol. **B 6** (1988) 574

LeGoues, F.K., Rosenberg, R., Meyerson, B.S., App. Phys. Lett. **54** (1989a) 644

LeGoues, F.K., Rosenbarg, R., Nguyen, T., Himpsel, F., Meyerson, B.S., J. Appl. Phys. **65** (1989b) 1724

Mayer, M., *SIMNRA User's Guide*, Report IPP 9/113, Max-Planck-Institut für Plasmaphysik, Garching, Germany (1997)

Mayer, M., Proceeding of the 15th International Conference on the Application of Accelerators in Research and Industry, Duggan, J.L., Morgan I.L., (Eds.), AIP Conf. Proc. **475** (1999) 541

Olsen, S.H., O'Neill, A.G., Norris, D.J., Cullis, A.G.,. Bull, S.J, Chattopadhyay, S.,. Kwa, K.S.K, Driscoll, L.S., Waite, A.M., Tang, Y.T., Evans, A.G.R., Mat. Sci. and Eng. B **109** (2004) 78

Pauling, L., *The Chemical Bond***,** Cornell University Press, New York (1967)

Spadafora, M., Terrasi, A., Mirabella, S., Piro, A., Grimaldi, M.G., Scalese, S., Napolitani, E., Garrido, M., Cuadras, B., A., Bonafos, C., Morante, J.R., Fonseca, L., Franz, M., Pressel, K., Microelectron. Eng. **48** (1999) 207

Spadafora, M., Terrasi, A., Scalese, S., Bongiorno, C., Carnera, A., Marino, M. D., Napolitani, E., App. Phys. Lett. **83** (2003) 3713

Speight, J.G, *Lange's Handbook of Chemistry***,** McGraw-Hill, New York (2005)

Sze, S.M., *VLSI Technology*, McGraw-Hill, (1983)

Terrasi, A., Scalese, S., Re, M., Rimini, E., Iacona, F., Raineri, V., Via, F. L., Colonna, S., Mobilio, S., J. Appl. Phys. **91** (2002) 6754

Tételin, C., X. Wallart, J. P. Nys, L. Vescan, D. J. Gravesteijn, J. Appl. Phys., **83** (1998) 2842

Wilson, R, *Metallurgy and Heat Ttreatment of Tool Steels***,** McGraw-Hill, New York (1975)

Ziegler, J. F., Biersack, J. P., Littmark, U., *The Stopping and Range of Ions in Solids***,** Pergamon Press, New York (1985)

CHAPTER 5

METHODOLOGY OF SYNTHESIZING THIN-FILM GeSi: EXPERIMENTAL METHOD AND INITIAL CONSIDERATIONS

5.1 Experimental Method and Sample Preparation

Commercially available silicon-on-insulator (SOI) wafers were used in the present study. They were supplied by MEMC Electronic Materials Inc. with the following specifications: size- 100 mm ± 5 mm; orientation-type- (100) CZ; device silicon thickness- 1899 Å, uniformity- 24 Å, dopant- B (p-type), resistivity- 10−20 Ω·cm; and BOX thickness- 3704 Å. The device side was polished and passivated with a 490 Å oxide layer. Some properties were unspecified, e.g., BOX thickness uniformity, surface roughness, dislocation density, BOX defects (pipe defects), HF defects, and surface metals, which can be important parameters [Chediak *et al*., 2002] for certain applications. The processing steps involved in the synthesis of a thin GeSi film are schematically illustrated in Figure 5.1. The wafers were initially treated with a dilute HF solution to remove the protective layer or native oxides, and then implanted with 70 keV Ge-ions. SRIM/TRIM simulations were done prior to implantation to determine various parameters (e.g. ion range). Fluences ranging from 1×10^{15} to 2×10^{17} ions/cm^2 were chosen in accordance with the targeted Ge_xSi_{1-x} film thicknesses. Implantation initially produces a very dilute GeSi solution within the implanted volume with a peak concentration at the projected ion range.

Subsequently, the dilute GeSi solution is processed by thermal oxidation to form a highly enriched GeSi layer on the underlying buried oxide, i.e., BOX. Oxidation was done in a standard quartz-tube under either dry O_2 conditions or wet conditions achieved by bubbling O_2 gas through deionized water at ~95 ˚C. The oxidation kinetics, previously discussed, were used to determine the necessary oxidation conditions to achieve this enrichment. Since the device Si

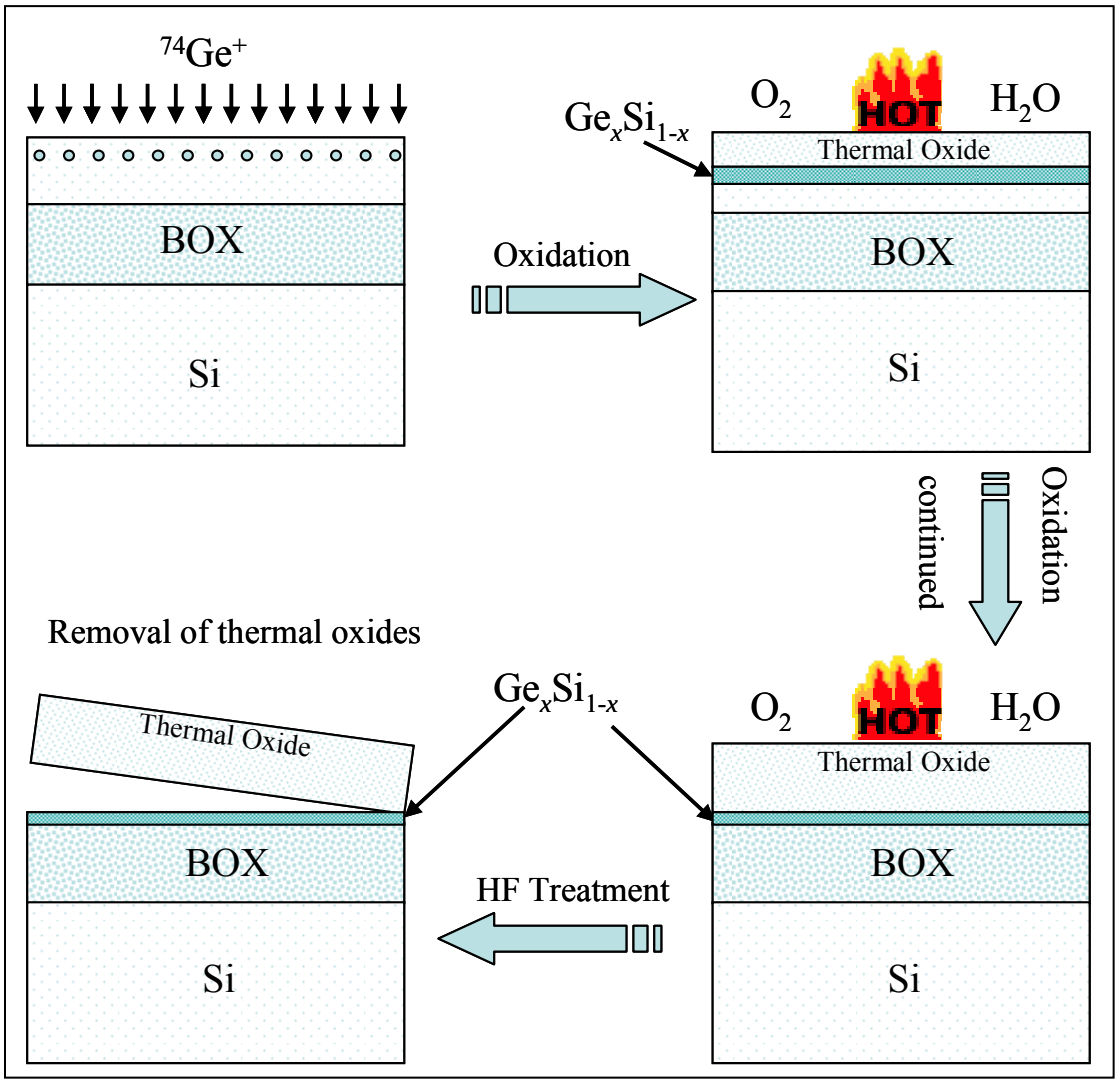

Fig. 5.1: Process flow for Ge_xSi_{1-x} thin film-on-insulator synthesis.

was vendor specified as ~1899 Å, an oxide thickness of ~4200 Å is required to consume all of the Si so that only a pure Ge film is left on top of the BOX, (since 0.44 nm of Si is consume for every nanometer of SiO_2). Kinetic data of the thermal oxidation of Ge-implanted Si (100) at 900 ˚C in wet ambient is shown in Figure 5.2 with a fitted curve (using the Deal and Grove model). These oxidation conditions were considered optimal since both simulation and experimental data, as discussed in Chapter 4, indicated that wet thermal oxidation at 900 ˚C yields a nearly 100 % Ge film at the reaction interface. The circled data points, corresponding to

this targeted oxide thickness, indicate that 92 min. oxidation is required to remove all of the Si from the top layer. At different stages of sample preparation and analysis, dilute HF solution (1:1 = DI water: 48 % HF) was used to etch off this surface oxides to expose the segregated Ge_xSi_{1-x} film.

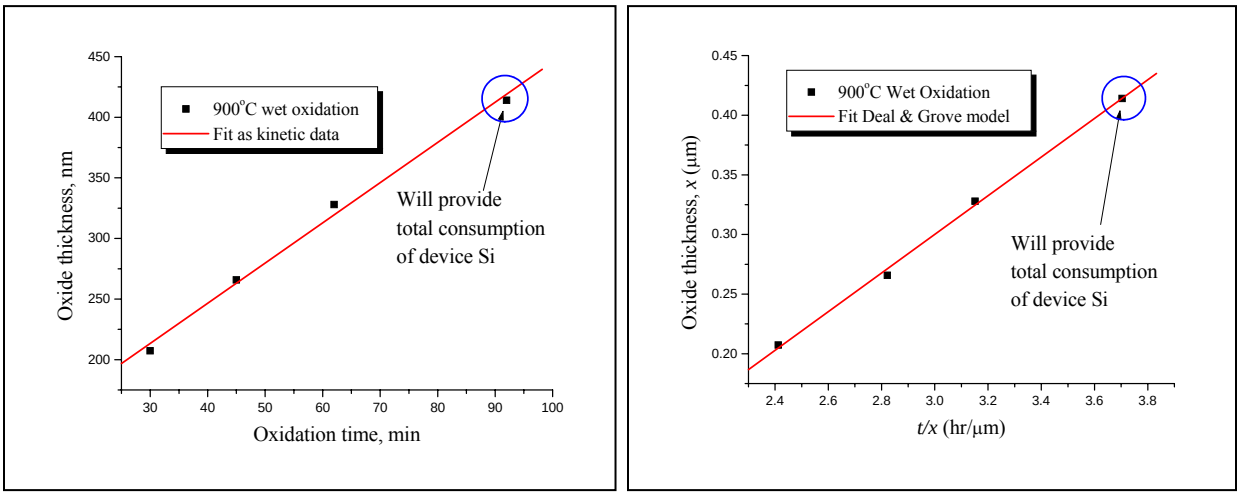

Fig. 5.2: Kinetic data of the thermal oxidation of Ge^+-implanted Si (100) at 900 ˚C in wet ambient expressed as a function of both *t/x* and *t*.

5.2 Process Monitoring and Control

At different stages of sample preparation and thin film synthesis ion beam characterization techniques were used for process monitoring.

5.2.1 Crystallinity of the Ge-rich Layer

The crystallinity of the segregated Ge-rich layer was investigated by the ion channeling technique. Channeled vs. random spectra are compared along both <100> and <110> axial directions after thermal oxidation of Ge-ion implanted silicon. The oxide layer was however removed with a dilute HF treatment before channeling analysis. Figure 5.3 shows the spectra

from a sample prepared by implanting a bulk Si wafer to yield about a 5 nm Ge layer after oxidation. The germanium fluence for this sample was 2×10^{16} ions/cm^2. A significant drop

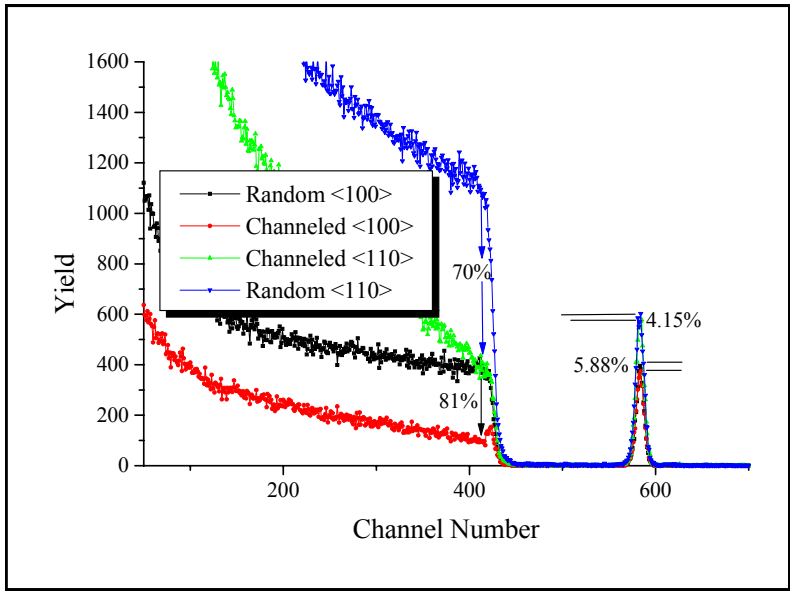

(*a*)

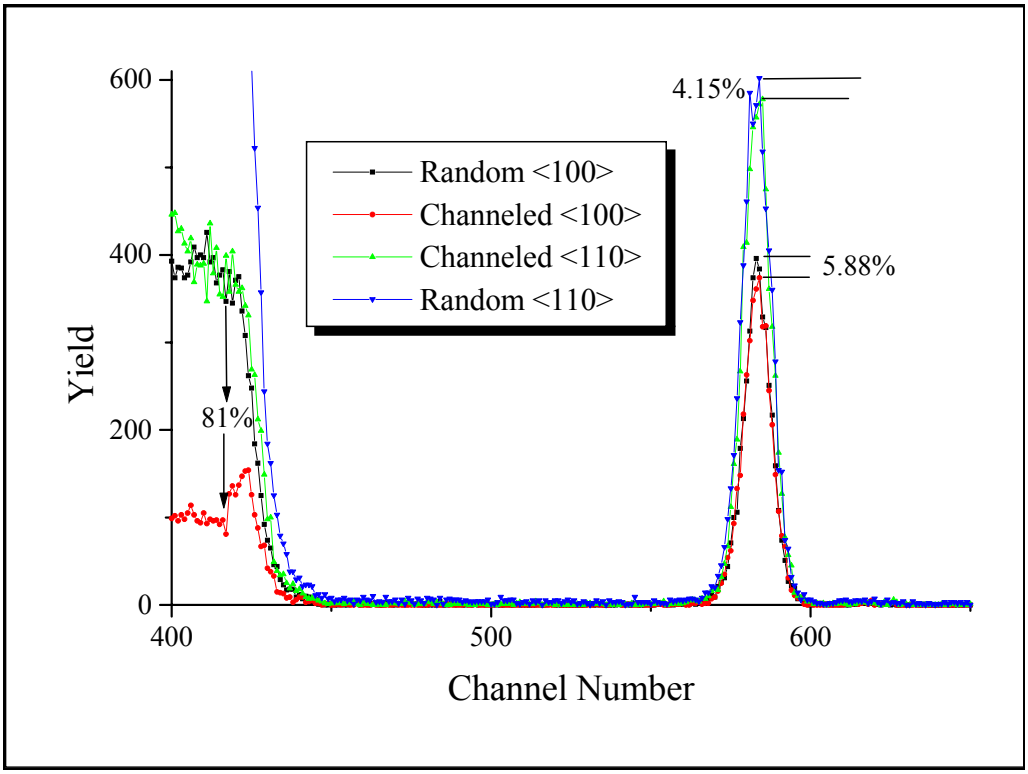

(*b*)

Fig. 5.3: (a) Random and ion-channeled RBS spectra of Ge_xSi_{1-x} thin film on Si, the baseline of which is magnified with (b) to show difference in channeling yield.

(70−80 %) in the aligned yield from the substrate, i.e., channeling minima, χ_{min} of 20-30 %, indicates that the crystallinity of the substrate is good. However, the difference in the aligned and random Ge yield is not nearly so large. This could indicate that the segregated Ge film is quite defective, although this is not consistent with inspection by electron microscopy that showed the layer to be a defect-free, single crystal. Alternatively, the first several monolayers of a single-crystal target are largely visible to the ion beam during channeling due to surface reconstruction and thermal vibrations [Chu *et al.*, 1978]. Therefore, the channeling yield from very thin films is not expected to be as reduced as in a bulk crystal. To more clearly distinguish the difference in backscattered yield from Ge-rich layer, the scale in Figure 5.3 (*a*) is magnified and the results shown in Figure 5.3(*b*). It is somewhat disappointing that the channeling minima, χ_{min}, is not lower than ~95 %.

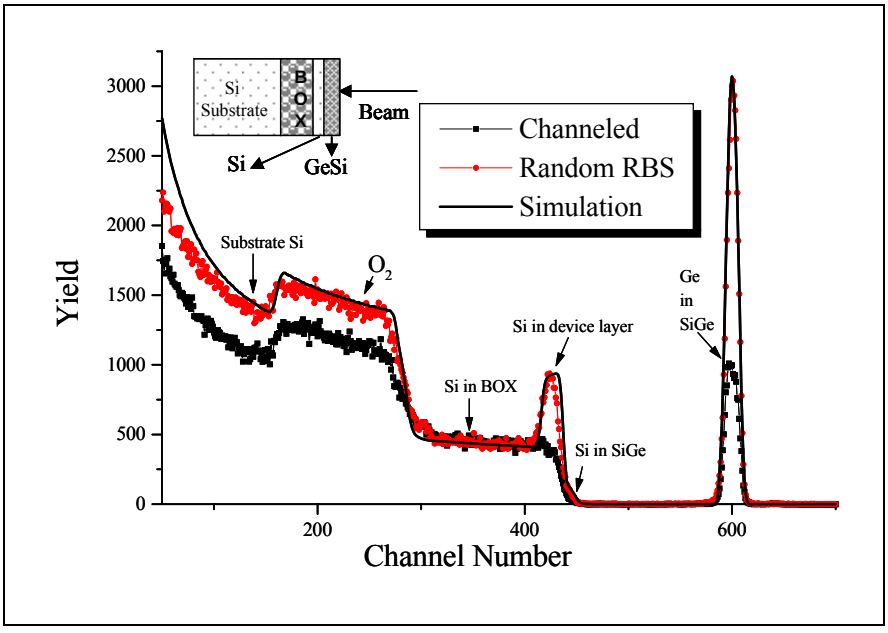

Fig. 5.4: Random and ion-channeled RBS spectra of a thicker Ge_xSi_{1-x} thin film along simulated results illustrating a crystalline and aligned $Ge_{0.95}Si_{0.05}$ film-on-SOI.

However, a thicker film was synthesized by implanting Ge at a higher fluence, i.e., 2×10^{17} ions/cm^2, into SIMOX type SOI to better understand the previous channeling results. Channeling results along <100> from this sample are compared in Figure 5.4 to the random yield- both experimental and simulated using the computer code SIMNRA [Mayer, 1997]. It can be seen that the simulation has resolved a Ge-rich layer of $Ge_{0.95}Si_{0.05}$ with the thickness of 31 nm on SOI. A channeling minimum, χ_{min}, of 0.29 is observed from the GeSi film indicating that the segregated thin film is of very good crystalline quality.

The quality of as-received SIMOX wafers was also examined to determine its quality and to confirm the vendor's specifications. RBS spectra from such samples are shown in Figure 5.5 for wafers received from one of the vendors. As it was mentioned earlier, during the process of SOI preparation by the SIMOX method, O^+-implanted silicon is annealed at about 1250 ˚C in an argon atmosphere with about 5 % oxygen for several hours. A thick layer of silicon dioxide is formed during this process, in addition to the development of a buried oxide (BOX).

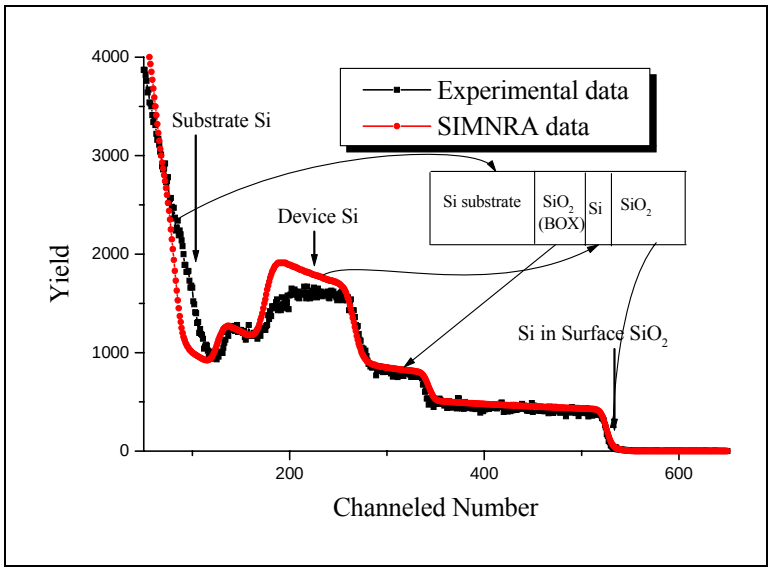

Fig. 5.5: RBS spectrum along with simulation on a SIMOX type SOI wafer as-received from a vendor (University Wafers).

As seen in Figure 5.5, the as-received SOI has a thick layer of thermal oxide (~7000 Å) as a top layer. Thus, the samples were cleaned and etched using a diluted HF solution [1:1 = 48 % HF: DI (deionized) water] followed by rinsing with DI water to remove any impurities and/or surface oxides. The samples were then analyzed to examine the quality of the device silicon, as well as the buried oxide (BOX) interface. Channeled vs. random RBS spectra of SOI wafer

(*a*)

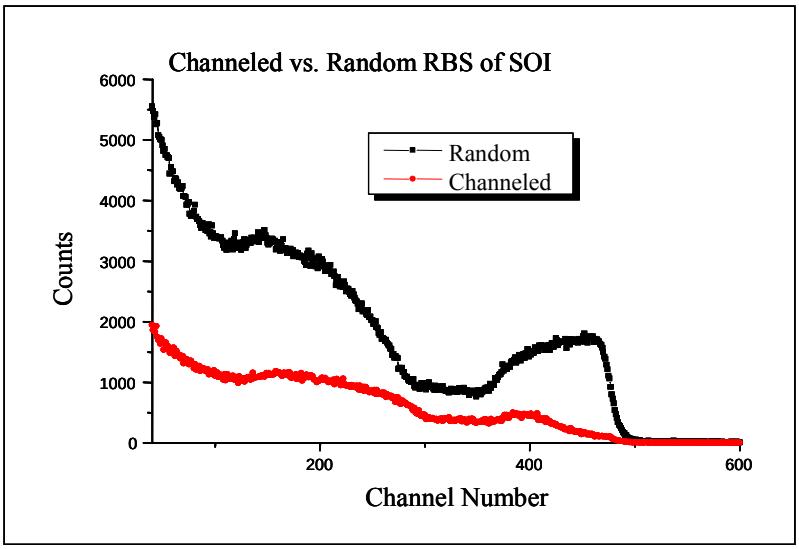

(*b*)

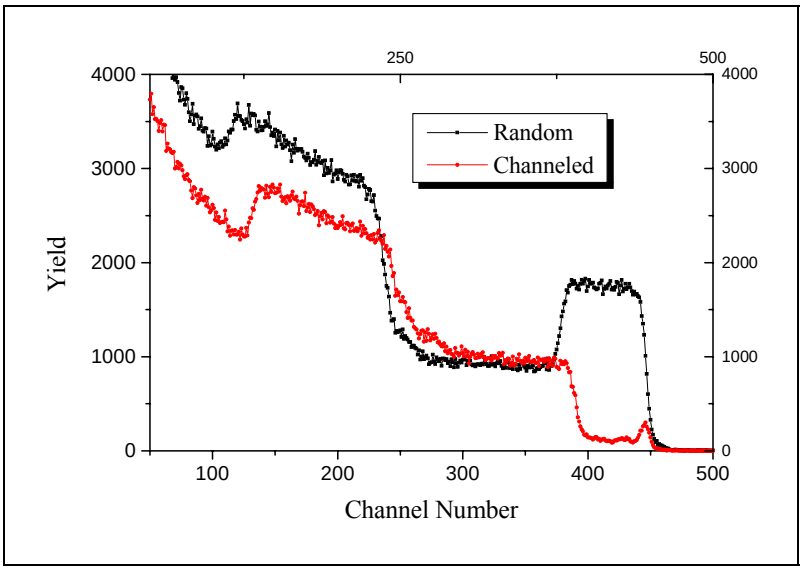

Fig. 5.6: Random vs. channeled RBS spectra of SOI wafers; (*a*) and (*b*) represents two different vendors.

from two different vendors are shown with Figure 5.6 (*a*) and (*b*). Figure 5.6 (*a*) represents sample from University Wafers, and Figure 5.6 (*b*) represent SIMOX from MEMC Electronic Materials Inc. supplied to Motorola Inc. The spectra indicate that, the device layer is of a much higher quality in the MEMC material since the channeling minimum, χ_{min} , of this layer is ~7 %, which is lower than in the other vendor's wafer, Also, the interfacial region between the device layer and the BOX is much more distinct in the MEMC material. This is seen from comparison of the scattering yield from the regions near the front and back oxide interfaces. It is clear the increase in the scattering yield (between Si and SiO_2) occurs much more rapidly in the MEMC samples. This indicates that the two interfaces in the wafers from University Wafers are either very rough or not distinct. As a result the SIMOX supplied by MEMC Inc. was chosen as the substrate for our present study.

5.3 References

Chediak, A., Scott, K., Zhang, P., *SIMOX-The winner for 300mm SOI Wafer Fabrication*, (website of P. Zhang www.mse.berkeley.edu/~pzhang/MSE225/) (2002)

Chu, W., Mayer, J.W., Nicolet, M.A., *Backscattering Spectrometry*, Academic Press, New York, (1978)

Mayer, M., *SIMNRA User's Guide*, Report IPP 9/113, Max-Planck-Institut für Plasmaphysik, Garching, Germany (1997)

CHAPTER 6

THIN FILM SEGREGATION

6.1 Results and Discussion

While the process of fabricating a thin GeSi film on SiO_2 is simple in theory, it can be a very difficult process to control. In particular, the removal of Si from the device layer by oxidation is a simple process; it must be controlled precisely to ensure that all of the Si is removed without overdriving the process leading to damage of the almost pure Ge film.

A step-by-step segregation routine has been established to achieve a reproducible and controllable process for producing a GeSi thin film on insulator (GOI) wafer. As discussed in the previous chapter, the kinetic data indicates that wet oxidation at 900 ˚C for an hour and thirty

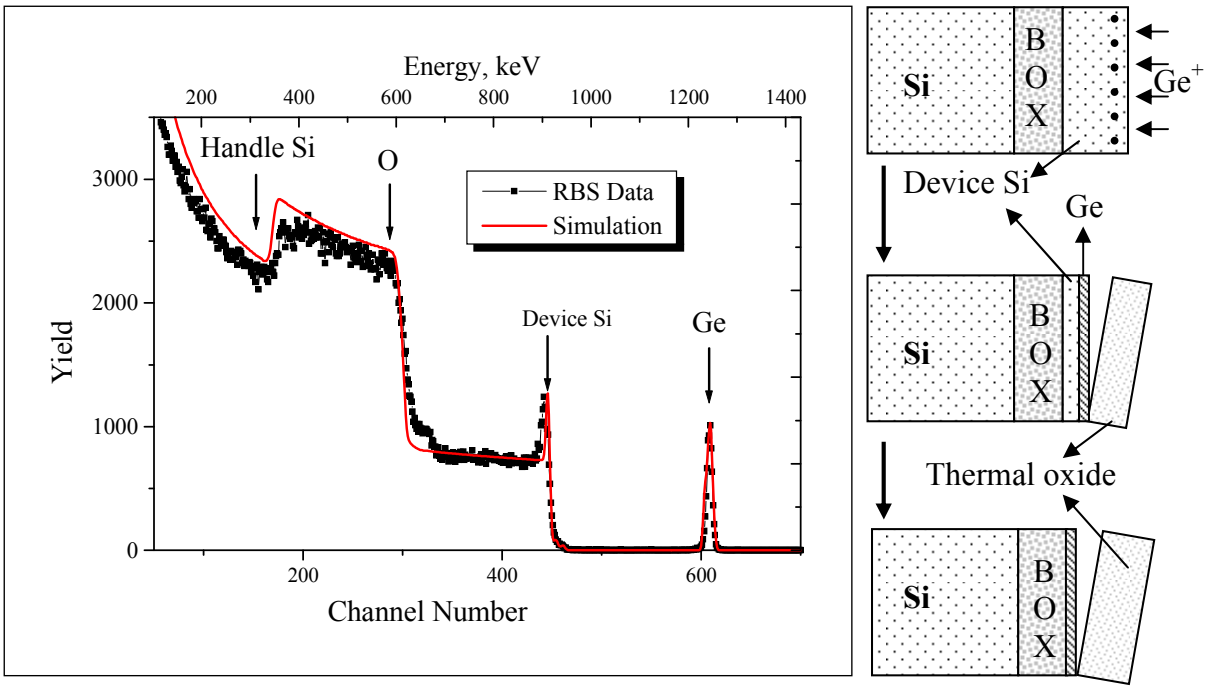

Fig. 6.1: (*a*) RBS and a simulated spectrum of Ge-rich thin film on insulator with 10-20 nm of device Si in-between (*b*) illustration of process steps to facilitate a better understanding of the experimental and simulated spectrum.

minutes is required to consume all of the Si within the device layer. Thus, samples were analyzed by Rutherford backscattering spectroscopy (RBS) at frequent intervals during the oxidation cycle starting with an oxidation time of 1 hr and 25 min. Thereafter, samples were oxidized using a slightly longer thermal cycle, i.e., a few minutes, and then analyzed. Results from some of the analyzed sample will be discussed.

A spectrum and SIMNRA [Mayer, 1997] simulation are shown in Figure 6.1 from a sample that was oxidized for 1 hr and 25 min. Prior to analysis the thermally-grown oxide was removed by dilute HF solution (represented by the peeled off thermal oxide in Fig 6.1(*b*)). The best-fit simulation spectrum indicated that the area under the Ge peak corresponded to 1.3×10^{16} ions/cm^2. However, there remains about 10 nm of Si in the device layer underneath the Ge. This is seen from the scattering peak from this Si layer located near the scattering from the front of the BOX.

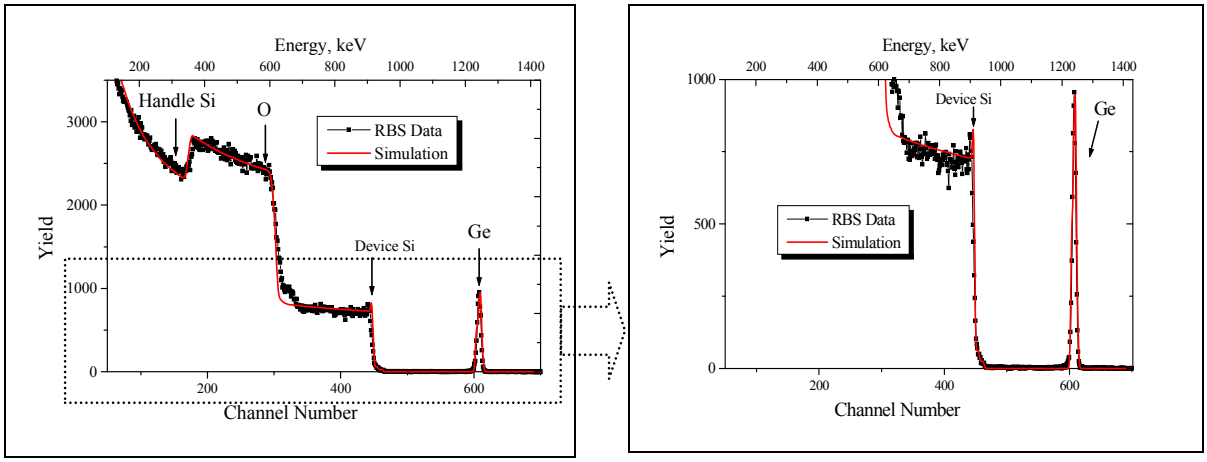

Fig. 6.2: RBS and simulated spectra of Ge-rich thin film on insulator with ~3nm of device Si in-between.

Figure 6.2 represents a sample which was oxidized for 1 hr and 30 min. Best-fit simulation shows a pure layer of Ge thin film was formed during the segregation process. The magnified section of the spectrum, however, shows that about 3 nm of Si remains behind the Ge

layer. This silicon with tensile stress (as it is suggested by the results of Raman spectroscopy, which are discussed separately) can be a good source of strain silicon-on-insulator (SSOI). Keeping that topic aside for future study, the objective of the present work is to consume the device silicon as thermal oxide to achieve Ge-on-insulator (GOI).

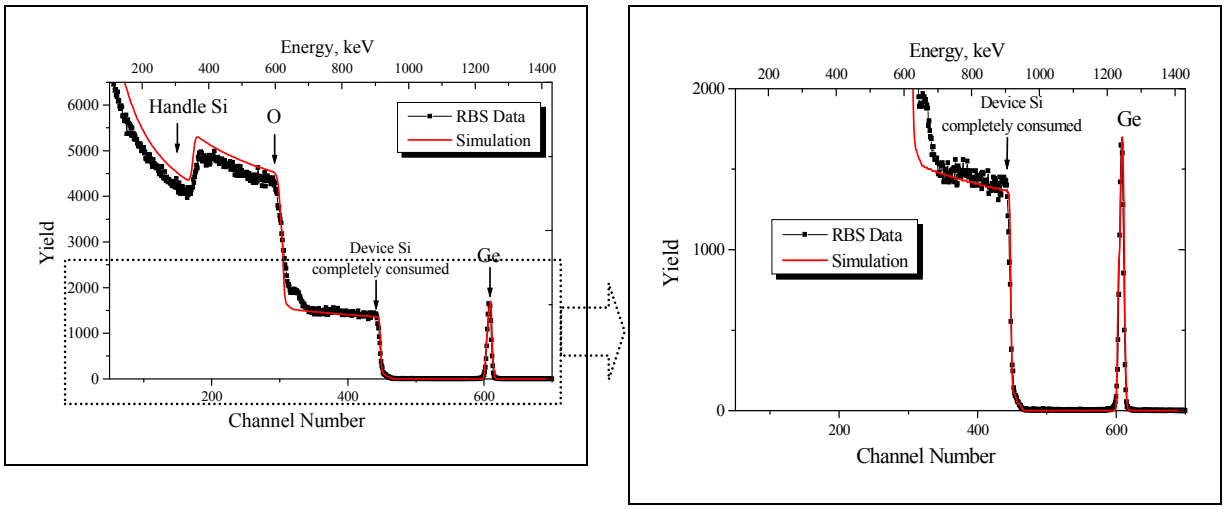

Fig. 6.3: RBS and simulated spectra of Ge-rich thin film on insulator without any sign of device Si in-between.

Figure 6.3 represents another sample with a few additional minutes in the oxidation furnace. RBS data does not indicate any evidence of having device silicon. Simulated spectra show a very good fit with a germanium thin film of 2.6 nm in thickness on insulator.

Some samples were oxidized a little longer and the effects were explored. Figure 6.4 represents a sample which was oxidized a few minutes longer than the sample, represented by Figure 6.3. It can be inferred from the spectrum that much of the germanium has disappeared

during exposure to the oxidizing ambient. GeO_2 is not stable, and in the presence of silicon (from the device layer) dissociates as indicated by the following reaction:

$$GeO_2 + Si \rightarrow SiO_2 + Ge$$

GeO_2 has a similar structure with that of SiO_2 with a boiling point of 1200 ˚C. If no silicon is present then GeO_2 can undergo the following reactions:

$$1/2GeO_2 + 1/2Ge(s) \rightarrow GeO(s) \rightarrow GeO(g)$$

which accounts for the loss of Ge when it is exposed to the oxidizing ambient in the absence of a Si underlayer. The process will be more apparent with the experiments and discussion mentioned in the following chapters.

The critical thickness for a stable Ge-rich layer is ~2 nm according to the Matthews-Blakeslee's [1974] equilibrium model. Thus, the film synthesized from Ge-ion implanted SOI at

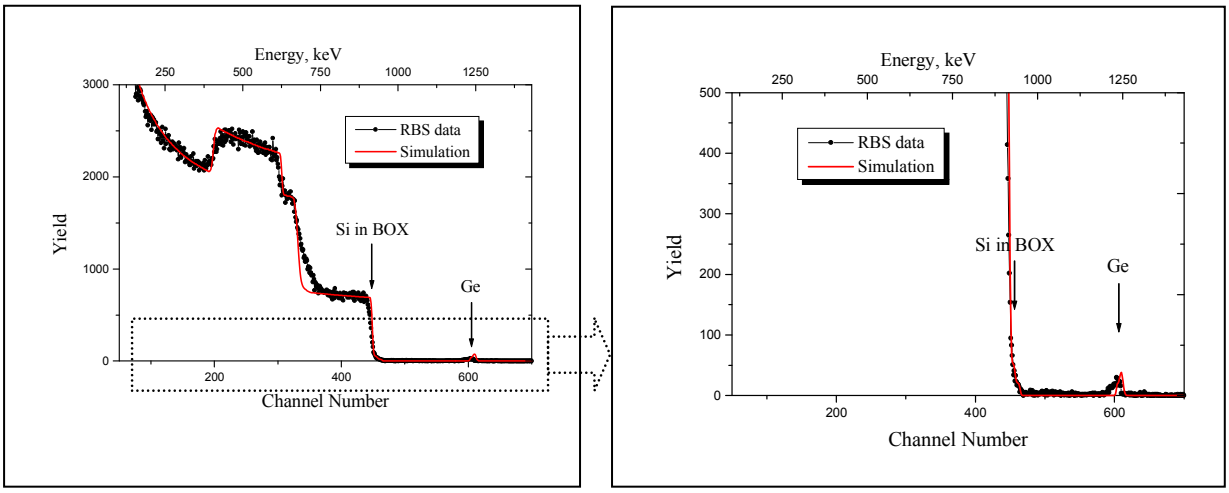

Fig. 6.4: RBS and simulated spectra of Ge-rich thin film on insulator which had the same initial dose as the sample with Figure 6.1-6.4. Significant Ge evaporation was noticed as GeO.

a dose of 1.3×10^{16} ions/cm^2 slightly exceeds the stable region. As a part of the study for the

formation of pseudomorphic and relaxed GeSi:Si heterostructures, GOI was prepared with the germanium film thickness near the stable region using a Ge implantation fluence of 2×10^{16} ions/cm^2. RBS spectra are shown in Figure 6.5 at different stages in the fabrication process. The as-oxidized spectrum in the figure indicates that germanium was completely harvested and made a sandwich layer between oxides. A sample at the identical stage of the fabrication process was analyzed with cross sectional scanning electron microscopy (SEM) and the results are discussed separately.

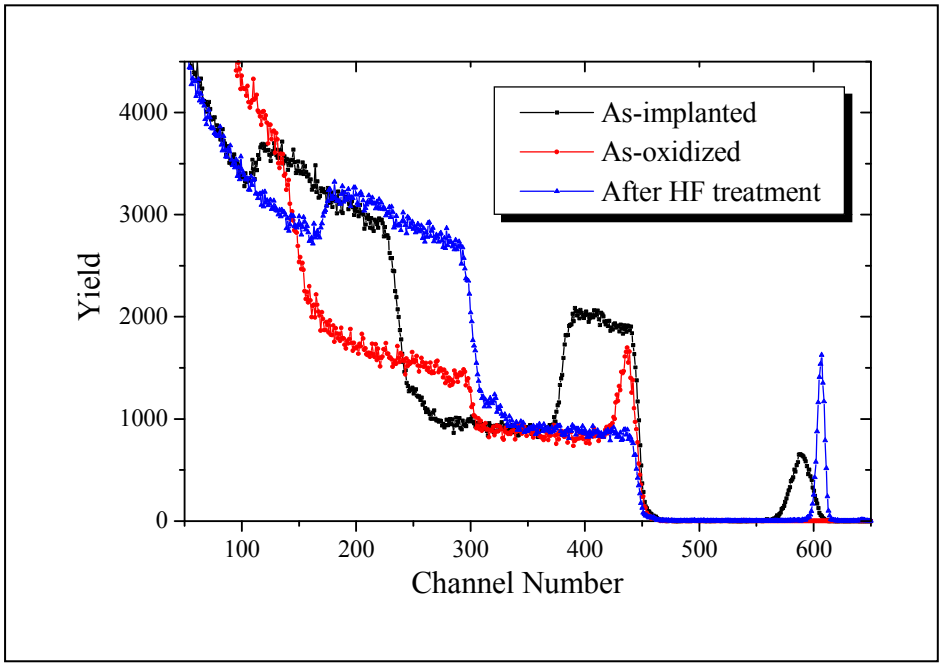

Fig. 6.5: RBS spectrum as analyzed at different stages of SGOI/GOI fabrication.

Best-fit SIMNRA [Mayer, 1997] simulation is separately shown with the RBS spectrum of the HF treated sample with Figure 6.6. Simulation showed that the Ge thin film was 4.2 nm in thickness without any evidence of residual silicon. The experimental conditions used for the

simulation were as follows: beam ^{4}He, energy 1.503 MeV, beam incident angle 10˚, exit angle

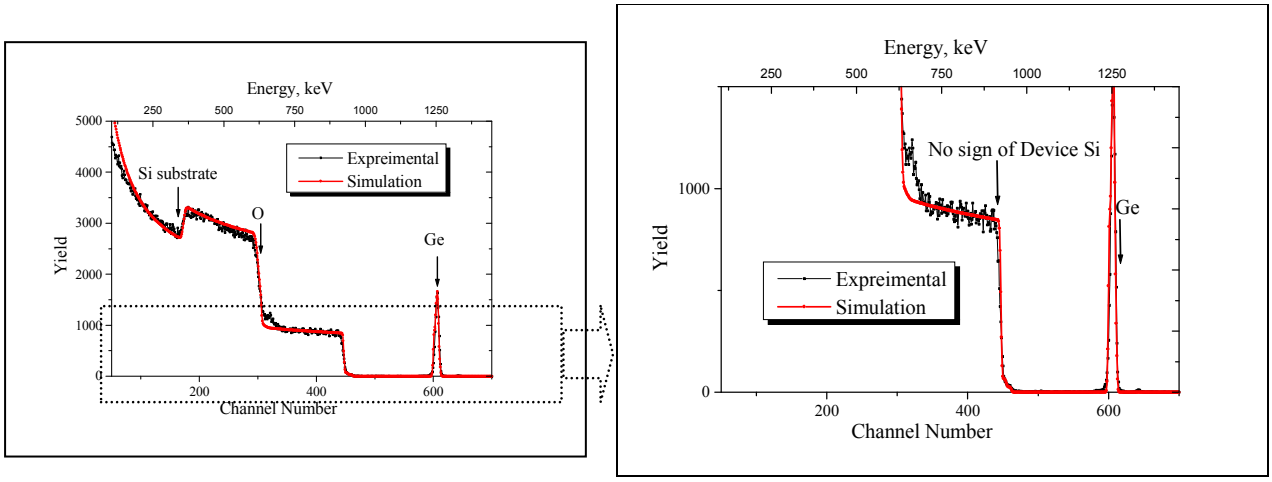

Fig. 6.6: RBS and simulated spectra of Ge-rich thin film on insulator with no sign of device Si in-between; initial dose was 2×10^{16} ions/cm^2.

55˚, scattering angle 135˚ and detector resolution was 6 keV. RBS resolution with such a situation is better than 2 nm for pure silicon as if it stays as device silicon behind the germanium film.

The process steps thereby lead to the fabrication of Ge_xSi_{1-x} on insulator, the strain relaxation and morphology of which films are discussed with the subsequent chapters.

6.2 Reference

Matthews, J. W., Blakeslee, A. E., J. Cryst. Growth (Netherlands), **27** (1974) 118

Mayer, M., *SIMNRA User's Guide*, Report IPP 9/113, Max-Planck-Institut für Plasmaphysik, Garching, Germany (1997)

CHAPTER 7

STRAIN RELAXATION

7.1 Theoretical Consideration

The relaxation of strained layer has been studied by different groups [Moran *et al.*, 1999, Moran *et al.*, 2000, and Hobart *et al.*, 2000]. Relaxation, in general, occurs plastically by surface roughening or the generation of misfit dislocations, which can lead to the formation of threading segments that penetrate to the free surface. Since threading dislocations, which originate from the misfits and penetrate through the film, can significantly degrade the opto-electrical properties of the material, research has focused on managing mismatch strain without dislocation generation. A. F. Vyatkin [2006] provided a summery of other groups' efforts including Matthews and Blakeslee's model [Matthews and Blakeslee, 1974] and described the role of point defects in SiGe thin film relaxation. According to Matthews and Blakeslee [1974], threading dislocation glide is affected by interactions of point defects with the dislocation core motion, which can inhibit glide. Point defects can also increase the probability of dislocation climb over glide, since climb requires either the addition or removal of atoms at the edge of the dislocation. Therefore, stress relaxation may occur through the formation of misfit dislocations but without the formation of threading dislocations.

To facilitate the present discussion, the previously shown graph (Figure 2.10) comparing the critical thickness as a function of germanium concentration in the Ge_xSi_{1-x}/Si system is repeated in Figure 7.1, where the black line with square symbol represents of the Matthews and Blakeslee equilibrium model and the red line with circular symbol represents the trend of experimental results of Douglas J. Paul [2004] in growing Ge_xSi_{1-x} on Si(100) at 550 ˚C by

molecular beam epitaxy (MBE). The regime above the theoretically calculated and the experimental determined thickness is usually known as *metastable* regime. Robert Hull [1995]

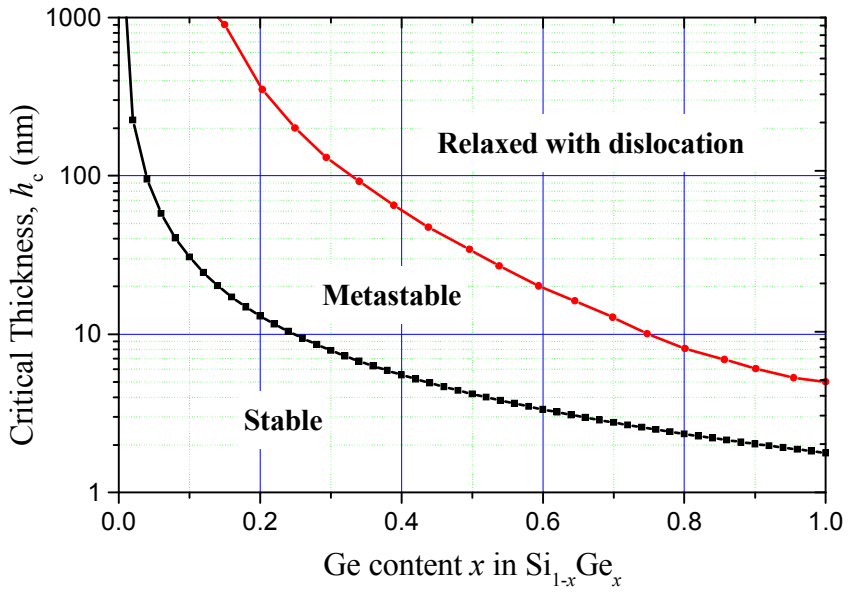

Fig. 7.1: Graphical representation of Matthews and Blakeslee's critical thickness of pseudomorphic $Si_{1-x}Ge_x$ layers as a function of germanium fraction comparing to experimental results.

proposed that the discrepancy between theory and the low temperature experimental observation of critical thickness is related to the kinetic barrier associated with relaxation. Even though the measurement in some instance depends on the limits for detecting a low density of dislocations, the extent of the metastable regime depends mostly on the following regions:

i. Growth temperature: a lower growth temperature can lead to sluggish relaxation kinetics since the relaxation is a thermally activated process with required energy >> *kT*.

ii. Growth rate: a higher growth rate can delay relaxation since the sample spends less time at higher temperature.

iii. Strain: misfit dislocation initiation and propagation rate usually increases with increasing strain.

iv. Interface orientation: smothers difference means wider regime.

v. Peierls barrier [Peierls, 1940] or Peierls-Nabarro stress [Nabarro, 1947], which is the activation energy required for moving a dislocation in an otherwise perfect crystal [Hull and Bacon, 2001]: The resistance to dislocation movement is related to inter-atomic barrier height i.e., the force between the atoms in the dislocation core. Si happens to have a relatively higher Peierls barrier and, as a consequence, the higher the Ge concentration in Ge_xSi_{1-x} the lower the resistance for dislocation movement.

As in any thermally activated process, dislocation motion must overcome an energy barrier to be active. The effective stress, which is the difference between lattice mismatch stress and restoring stress from the created misfit dislocation, is the driving energy for the process of energy accommodation. Dodson and Tsao [1987] demonstrated that the formation of a coherent metastable strain layer can be explained simply by a standard description of dislocation dynamics. In any event, the effective stress is the driving force for misfit dislocation development and motion. For a thickness up to the critical value, the effective stress is negative and, above this value, the increasing effective stress makes dislocation formation energetically more favorable. Due to an initial sluggishness of the relaxation kinetics, a slightly thicker strained layer can coexist as demonstrated by different research groups [Paul, 2004, Dodson and Tsao, 1987], the example of which is illustrated with Figure 7.1 as well.

The 4 % lattice mismatch between Si and Ge is accommodated in heteroepitaxial growth by biaxial strain in the Ge film, which is equivalent to about 8 % of volume change as calculated below (Calculation parameters are illustrated with Figure 7.2.):

$V = a_1^2 a_2$, where a_1 is the in-plane (strained) lattice parameter and a_2 is the out-of-plane lattice constant of Ge, so that $\Delta V/\Delta a = 2\, a_1\, a_2 \Rightarrow \Delta V = 2\, a_1\, a_2 \Delta a$.

Now, volume strain is $\Delta V/V = 2\, a_1\, a_2 \Delta a / a_1^2 a_2 = 2\Delta a / a_1 = 2 \times 0.04 = 0.08, \Rightarrow 8\ \%$, where $\Delta a = |a_1 - a_2|$ and the Si-Ge lattice mismatch $= |a_1 - a_2| / a_1 = 0.04$.

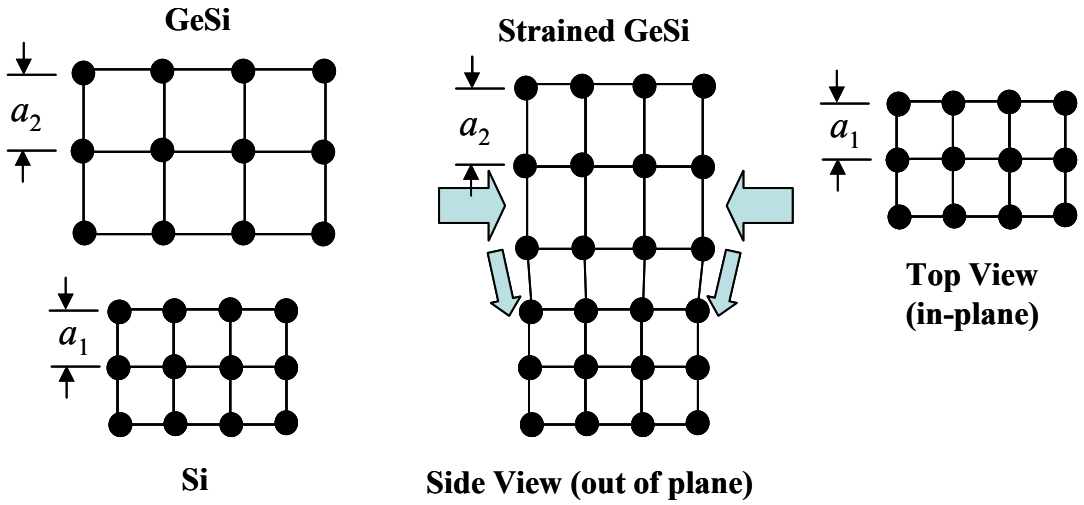

Fig. 7.2: Schematics of strain associated with lattice parameter in GeSi:Si heterostructure illustrating change in in-plane and out-of-plane lattice parameter.

Thus, the introduction of ~8 % vacancy concentration is required to fully relax a 4 % biaxially strained germanium layer. Some of the relaxation techniques are introduced before explaining the integrated partial relaxation phenomenon observed during the fabrication process.

7.1.1 Ion Irradiation

The injection of vacancies into a film by ion irradiation is a well-understood phenomenon. During ion radiation or ion implantation the energetic ion collides with the host atoms and, if any collision transfers enough energy above the corresponding displacement

energy, a vacancy (an empty lattice site left behind when a recoil atom leaves its original position) is formed. All displacement does not create vacancies because some of those (statistically about 30 %) are recovered by replacement collision. Vacancy productions are associated with sputtering, interstitials creation, and transferring the atoms to the next layer (for

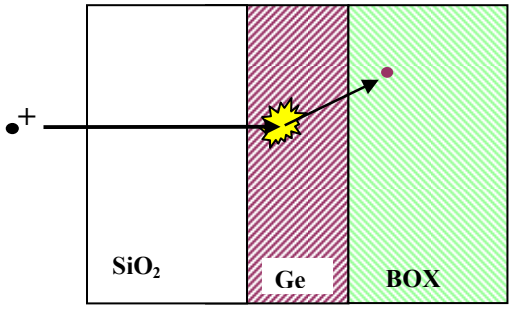

(*a*) Rarefaction of pseudomorphic film occurs during ion irradiation due to atomic recoil due to ion collisions. This leads to transport of matter (i.e., atoms) out of the film.

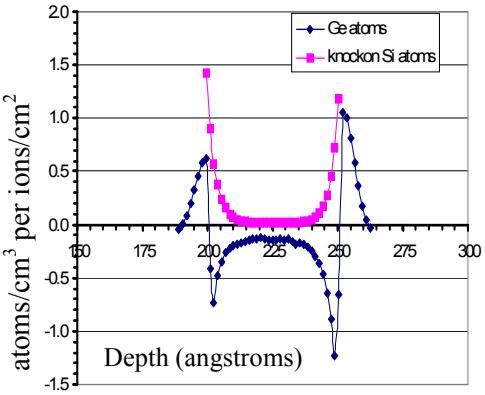

(*b*) TRIM (transport of ions in matter) simulation of rarefaction of Ge in a Si:Ge:SiO_2 heterostructure by 80 keV Ge^+-ions

Fig. 7.3: Schematics and simulated results of ion irradiation.

the present substrate materials, sinking into the buried oxide layer).

Preliminary investigations demonstrated that the introduction of vacancies within the device layer after initial oxidation could lead to the formation of an almost completely relaxed GeSi film on SiO_2. The injection of vacancies was done by high-energy implantations with Ge-ions with a range well within the BOX. Just as oxidation results in the transport of Ge by segregation, it appears that the ion-induced vacancies were similarly transported by the growing oxide interface. Thus, after oxidation under optimal conditions to remove all of the Si from the device layer, both the Ge and ion-injected vacancies remained. The vacancies appeared to provide the necessary open volume within the film to fully relax the elastic strain.

The process of ion-induced relaxation is illustrated in Figure 7.3. Of course, the critical part of the relaxation process is the use of a SOI substrate, which not only allows the Ge-rich film but also the injected vacancies to be transported to the buried oxide interface during thermal oxidation of the superficial Si layer. Relaxation of the segregated film is then achieved by injection of vacancies to provide sufficient open volume within the lattice to accommodate the compressive strain. Vacancy injection is demonstrated schematically in Fig. 7.3(*a*), which shows the interaction of an ion with a target atom resulting in the formation of a vacancy. Simulation of the ion-atom interaction in solids was done with the SRIM computer code. The simulated structure is shown in Fig. 7.3(*b*). As discussed earlier, this code tracks the interstitial transport in the solid within ion cascades, and as such can be used to determine the vacancy injection rate. Simulation results showing the excessive vacancies within a Ge film within Si:Ge:SiO_2 heterostructure is shown in Figure 7.3(*b*). The data denoted as Ge atoms gives the depth dependent change in the atomic density of Ge. It can be seen that there is substantial loss of Ge from the film (i.e., vacancy injection) through out the film with a greater loss near the interfacial boundary. It is this injection of open volume that provides the driving force for a compressively strained layer to relax. The critical dose necessary for full relaxation of strained Ge-layer, x (ions/cm^2), is therefore given as:

$$x = 8\ \% \times \text{film thickness (ions/cm}^2) \times \%\ \text{vacancy/ion.}$$

7.1.2 Sputtering

An alternative method of achieving relaxation in highly strained thin-films involves sputtering, a type of etching technique where the atoms from the surface or near-surface are sputtered out by transfer of momentum from the ion. Sputtering is a purely physical mechanism

unlike chemical processes. The various parameters that controls sputtering rate are the radio frequency (RF) power, the distance between the electrodes, sputtering pressure etc. It does not require ultrahigh vacuum and thin film thickness can be well controlled.

Sputtering can occur during ion implantation as well. During collision if a target atom is given energy greater than the surface binding energy (SBE) of that target, the atom may be sputtered (provided the leaving atom still retains the energy normal to the surface greater than the SBE). Heat of sublimation is commonly used to estimate the surface binding energy (SBE) of an atom to a surface and is known only for a few materials. Typical values are: 4.46 eV for Ni, 3.52 eV for Cu, 3.91 eV for Pd, 2.97 eV for Ag, 5.86 eV for Pt and 3.80 eV for Au [Ziegler *et al.*, 1985].

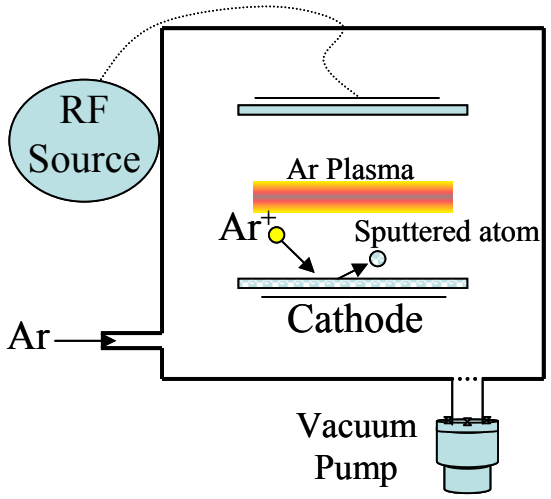

Fig. 7.4: Schematics of sputtering basics.

Sputtering, especially RF sputtering can be used to etch almost all type of materials like metal, semiconductors, and insulators. This is a quick and cost effect way of introducing point defects at or near the surface. It requires only 1×10^{-3} to 1×10^{-4} Torr pressure to create and maintain plasma for sputtering. Argon (Ar) is the mostly used gas for making plasma to knock out target atoms for introducing point defects. A schematic of the sputtering system with its essential components is illustrated with Figure 7.4. For a compressively strained thin film of a mono layer to a few mono layers of thickness, sputtering can be used effectively as a method to induce relaxation of mismatch strain. As the mechanism

is illustrated with the 1-D example (in Figure 7.5) in which a strained, closed-packed row of atoms is sputtered and a single vacancy is injected. Only slight atomic rearrangements are required thereafter to relax the atomic row.

Fig. 7.5: One dimensional illustration of strain relaxation by sputtering.

7.2 Results and Discussion

Figure 7.6 represents the results of the Raman spectroscopy, which was used to characterize the strain in the thin film. A monochromatic laser with 488 nm in wavelength was used to excite the samples. There are four Raman active modes are present in Ge_xSi_{1-x}/Si system, namely (i) Ge−Ge mode (ii) Si−Ge mode and (iii) Si−Si mode from SiGe, and (iv) Si−Si mode

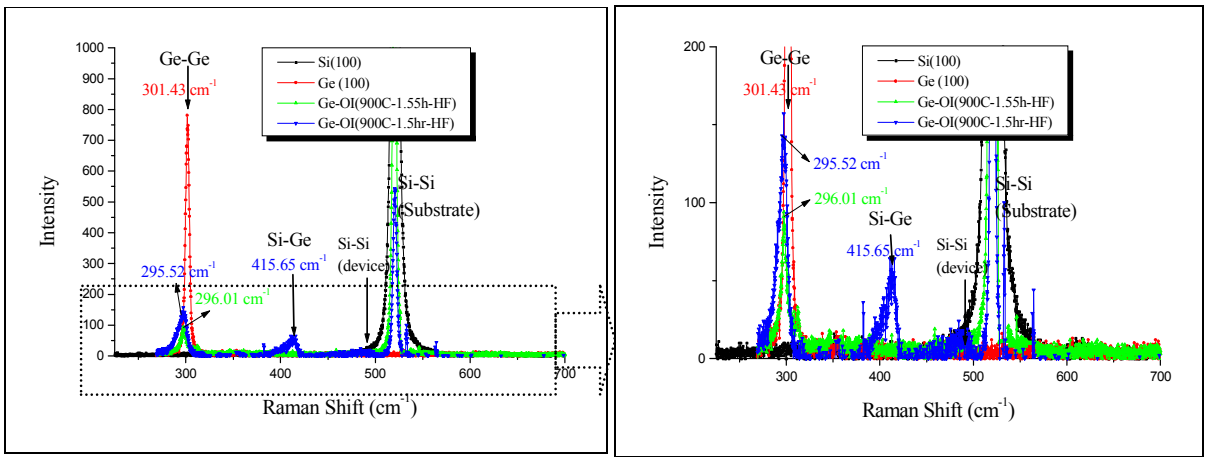

Fig. 7.6: Raman spectra of SGOI and GOI layers along with those of bulk Ge and Si.

from the substrate. As is seen from the spectra, the close proximity of the Ge−Ge peak to the bulk Ge peak indicates partial relaxation of the film. A strain calculation by using the equation, given earlier as $\omega_{Ge-Ge} = 282.5 + 16x - 385\varepsilon$ cm^{-1} [Chen *et al.*, 2002], yields a value of less than 1 % indicating substantial relaxation. Additionally, the 1.5 cm^{-1} Raman shift towards the relaxed state of the specific sample which was kept a few minutes longer in the oxidation furnace indicates that the relaxation process is an integrated part of the fabrication process. Before getting into the discussion on relaxation processes, the other important feature that the spectra resolved was the existence of Raman modes of Si−Ge and Si−Si from thin films. The disappearance of Si−Ge and Si−Si modes in some samples (as revealed in Figure 7.6) at some stage of thin film synthesis indicates that a pure Ge layer on insulator (GOI) was formed. A similar disappearance of the Si−Ge and Si−Si modes in Raman spectrum was noticed by the Takagi group in Japan [Nakaharai *et al.*, 2003] during the final stages of fabricating GOI by a Ge-condensation technique. The details of the stages have already been discussed in Chapter 6, along with RBS data and SIMNRA simulations.

Two different mechanisms to account for the spontaneous relaxation of the Ge film during segregation (i.e., as observed by Raman spectroscopy) are discussed in the following. These include (*i*) the evaporation of Ge atoms, and (*ii*) compliant substrate: Si (device)-SiO_2 (BOX) interface roughness in SIMOX.

(*i*) The evaporation of Ge atoms

During oxidation of the implanted SOI, snow-plowed Ge enriches in concentration within a very small volume with its surface exposed to the oxidant. This may encourage the formation of GeO, which is volatile. At the later stages of oxidation, when little or no Si is present within the reaction volume, the reactions

$$\frac{1}{2}GeO_2 + \frac{1}{2}Ge(s) \rightarrow GeO(s) \rightarrow GeO(g) \text{ instead of } GeO_2 + Si \rightarrow SiO_2 + Ge$$

will lead to the loss of germanium from the film. The activation energy or the enthalpy of the reaction GeO(s) → GeO(g) is 62 kcal/mol [Pauleau and Remy, 1975], which is only favorable when the Si supply is insufficient. The phenomenon is illustrated schematically with Figure 7.7.

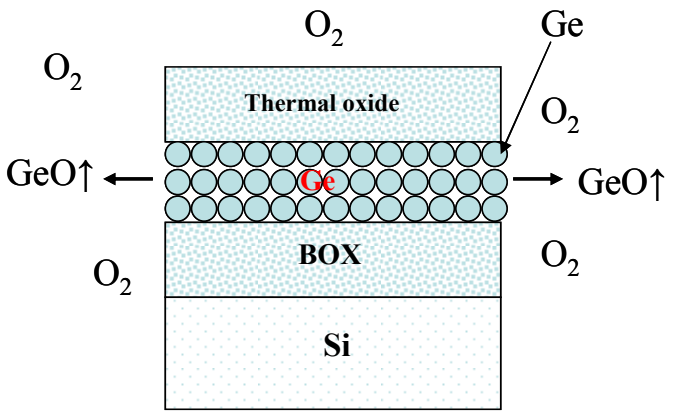

Fig. 7.7: Illustration of Ge-evaporation.

The Ge-rich layer is magnified for illustration purpose but the exposed area, which depends on the thickness of the Ge_xSi_{1-x}, is on the order of nanometers. Evaporated Ge atoms leave enough free spaces to the thin film for relaxation.

In order to gain evidence to support the Ge-evaporation phenomenon, a series of experiments were performed by oxidizing the exposed Ge-rich Ge_xSi_{1-x} thin films. To distinguish or to ensure that the Ge loss is not related to the oxide loss during HF treatment, the oxidized samples are analyzed before such etching. The results are presented with the Figures 7.8 to 7.11. The ROI (region of interest) integral ($\Sigma-\beta$) of Ge-peak was shown to be reduced significantly during oxidation of the exposed Ge-rich layer. The loss of Ge was noticed at a temperature as low as 800 ˚C. A similar observation was made by Ishikawa *et al.* [1999] during their investigation into the fabrication of SiGe-on-insulator by the SIMOX technique. Noticing the effect of Ge loss during thermal oxidation from the exposed Ge-rich layer Di *et al.* [2005] used a Si cap layer before stating the Ge condensation process (as SOI/Si/SiGe/Si sandwiches). However, Ge can still be lost even when the surface or

capping oxide is not removed. Little or no Ge is lost during oxidation as long as the surface oxide layer remains intact (if oxidation does not persist beyond the critical point where all of the Si within the device layer is consumed). Beyond this point, Ge loss is observed. This is

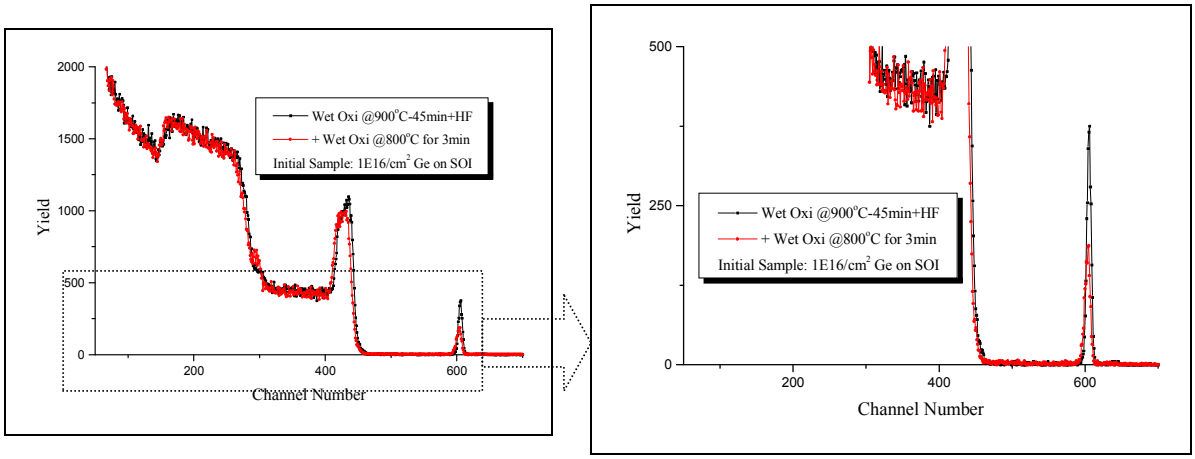

(*a*) (*b*)

Fig: 7.8 (*a*): Sample: Ge-implanted on SOI with doses 1×10^{16} ions/cm^2, then wet oxidized at 900 ˚C for 45 min +HF treated. After RBS analysis, sample is wet oxidized for 3 min at 800 ˚C and analyzed again; (*b*) is for the same figure with (*a*) with base line magnified.

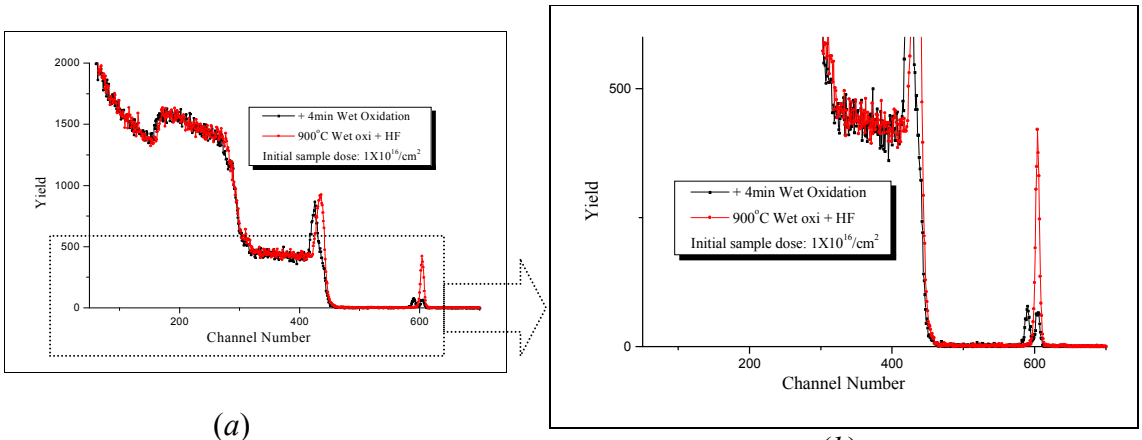

(*a*) (*b*)

Fig. 7.9: (*a*): Sample: Ge-implated on SOI with doses 1×10^{16} ions/cm^2, then wet oxidized at 900 ˚C for 45 min + HF treated. After RBS analysis, sample is wet oxidized for 4 min at 900 ˚C and analyzed again; (*b*) is for the same figure with (*a*) with base line magnified.

demonstrated with the RBS results in Figure 7.11. This figure is identical to Figure 6.4 and is repeated here to demonstrate the loss of Ge that occurs beyond the critical point. It is clear that

most, if not all, of the Ge can be lost due to formation of GeO(g) during oxidation. At the same time, the amount of exposure during oxidation can be utilized as beneficial tool for stimulating thin film relaxation through Ge loss rather than formation of misfit dislocations.

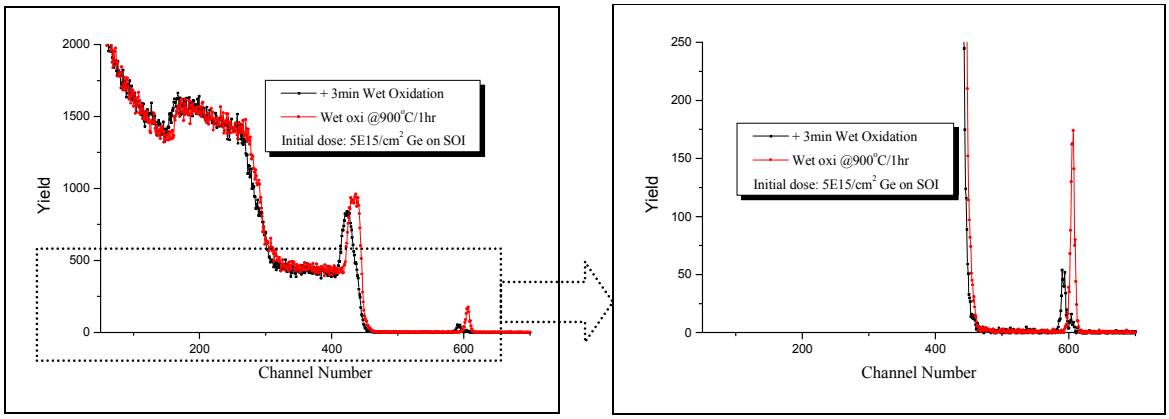

Fig. 7.10: Sample implanted on SOI with 5×10^{15} Ge ions/cm^2, is then wet oxidized at 900 ˚C for 45 min + HF treated. After RBS analysis, sample is wet oxidized for 3 min at 900 ˚C.

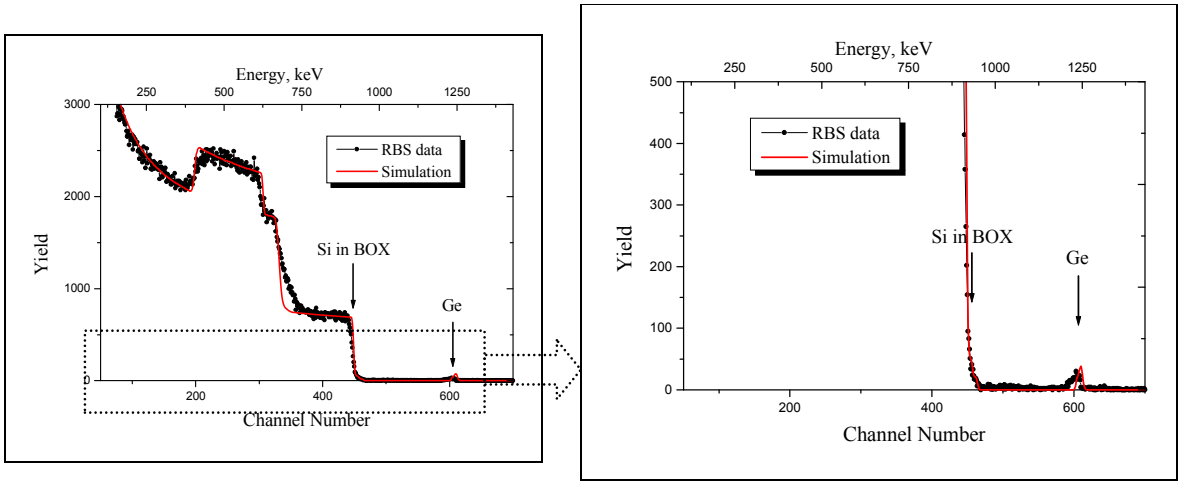

Fig. 7.11: RBS and simulated spectra demonstrating a significant Ge evaporation as noticed during over oxidation even with cap oxide layer on (same as Figure 6.4).

(*ii*) Compliant substrate and interface roughness

In SIMOX, the Si/BOX interface is rough and acts as a better compliant substrate for relaxed Ge_xSi_{1-x} thin films without forming dislocations. As different groups [Moran *et al.*, 1999, Yamanaka *et al.*, 2006] demonstrated a rough growth surface promoting strain relaxation without dislocation deformation, Yamanaka *et al* [2006] demonstrated the formation of a strained-relaxed SiGe thin film by growing on a previously ion irradiated silicon. Si-ion implantation may promote relaxation of the MBE-grown film by injection of point defects into the growth substrate and/or by roughening of its surface (due to sputtering). The rough interface of SIMOX type SOI makes the Ge_xSi_{1-x} thin films relax by partial strain accommodation by plastic deformation at the interface. The morphological evidence will be revealed with the cross sectional microscopy, the results of which are discussed in the following chapter. The effect of substrate roughening and film relaxation was demonstrated by different groups (Eaglesham and Hull, [1995] with Ge/Si epitaxy, and Peale *et al.* [1995] with β-$FeSi_2$/Si epitaxy). The presence of higher surface roughness and dislocation densities than Unibond [Chediak *et al.*, 2002] makes SIMOX a better starting material for the present study of fabricating partially strain-relaxed Ge_xSi_{1-x}-on-insulator.

7.3 References

Chediak, A., Scott, K., Zhang, P., *SIMOX-The winner for 300mm SOI Wafer Fabrication*, (also online at www.mse.berkeley.edu/~pzhang/MSE225/) (2002)

Chen, H., Li, Y. K., Peng, C. S., Liu, H. F., Liu, Y. L., Huang, Q., Zhou, J. M., Xue, Q.K., Physical review B **65** (2002) 233303

Di Z., Zhang, M., Liu, W., Zhu, M., Lin, C., Chu, P. K., Materials Science and Engineering B **124–125** (2005)

Dodson, B. W., Tsao, J.Y., App. Phys. Lett., **51** (1987) 1325

Eaglesham, D.J., Hull, R., Materials Science and Engineering B **30** (1995) 197

Hobart, K. D., Kub, F. J., Fatemi, M., Twigg, M. E., Thompson, P. E., Kuan, T. S., and Inoki, C. K., J. Electron. Mats., **29** (2000) 897

Hull, R., Section 1.2, 1.3 in *Properties of Strained and Relaxed Silicon Germanium*, Edited by Eric Kasper, INSPEC, Germany (1995)

Hull, D., Bacon, D. J., *Introduction to Dislocations*, 4th Edition, Pergamon Press Oxford, New York (2001)

Ishikawa, Y., Shibata, N., Fukatsu, S., Appl. Phys.Lett. 75 (1999) 983

Matthews, J. W., Blakeslee, A. E., J. Cryst. Growth (Netherlands), **27** (1974) 118

Moran, P. D., Hansen, D. M., Matyi, R. J. Cederberg, J. G., Mawst, L. J., Kuech, T. F., App. Phys. Lett., **75** (1999) 1559

Moran, P. D., Hansen, D. M., Matyi, Mawst, L. J., Kuech, T. F., App. Phys. Lett., **76** (2000) 2541

Nabarro, F. R. N., Proc. Phys. Soc., **59** (1947) 256

Nakaharai, S., Tezuka, T., Sugiyama, N., Moriyama, Y., Takagi, S., App. Phys. Lett., **83** (2003) 3516

Paul, D. J., Semicond. Sci. Technol. **19** (2004) R75

Pauleau, Y. Remy J.C., Journal of the Less Common Metals, **42** (2) (1975) 199

Peale, D.R., Haight, R., LeGouse, F.K., Thin Solid Films **264** (1995) 28

Peierls, R., Proc. Phys. Soc., **52** (1940) 34

Vyatkin, A. F., Thin Solid Films **508** (2006) 90

Yamanaka, J., Sawano, K., Suzuki, K., Nakagawa, K., Ozawa, Y., Hattori, T., Shiraki, Y., Thin Solid Films **508** (2006) Pages 103

Ziegler, J. F., Biersack, J. P., Littmark, U., *The Stopping and Range of Ions in Solids*, Pergamon Press, New York (1985)

CHAPTER 8

MORPHOLOGY OF THE THIN GeSi FILM

8.1 General Microscopy Principles

Imaging is necessary to study the morphology and structure of synthesized thin films. The choice of an imaging technique is limited by the required resolution. Rayleigh criterion of light microscope defines the resolution, δ, as follows [Williams and Carter, 1996];

$$\delta = \frac{0.61\lambda}{\mu Sin\beta} \ldots\ldots\ldots (8.1)$$

where λ is wavelength of the radiation, μ is the refractive index of the view medium and β is the collection of the magnifying lens. For a specific experimental setup μ and β remains the same, so the resolution, the smallest distance between two points that can be resolved, is proportional to the wave length of the radiation. The wavelength of visible light varies between 400 to 700 nm, which limits the resolution of optical microscopy to the hundreds of nanometer range (e.g., 300 nm resolution for green light with the wavelength of 550 nm). On the other hand, high-energy electrons can have a very narrow wavelength. Based on de Broglie's concept of wave particle duality, the wavelength, λ, can be related with the particle's momentum, p, as follows;

$$\lambda = \frac{h}{p} \ldots\ldots\ldots (8.2)$$

where h is Plank's constant. An electron accelerated by an electrostatic potential, V, gains kinetic energy equal to the potential energy as; $eV = m_o v^2/2$, and momentum, p, given by;

$$p = m_0 v = \left(2m_0 eV\right)^{1/2} \ldots\ldots\ldots (8.3)$$

where m_o is the rest mass of the electron and v is the velocity. The electron wavelength thereby changes with accelerating voltage as,

$$\lambda = \frac{h}{\sqrt{2m_0 eV}} \ldots\ldots\ldots (8.4)$$

Equation 8.4 and 8.1 infer that higher resolution can be achieved by applying higher accelerating voltage. However, the exact relationship between wavelength and electron energy can differ because the accelerated electron velocity reaches the relativistic region at higher potential drop. After performing appropriate transformation by considering the relativistic rest mass of the electron, the momentum expression turns into the following form:

$$p = \left[2m_0 eV \left(1 + \frac{eV}{2m_0 c^2} \right) \right]^{1/2} \ldots\ldots\ldots (8.5)$$

As a result, the electron wavelength varies as a function of energy as follows:

$$\lambda = \frac{h}{\sqrt{\left[2m_0 eV \left(1 + \frac{eV}{2m_0 c^2} \right) \right]}} \ldots\ldots\ldots (8.6)$$

For instance, an electron beam of 100 keV has a wavelength of 0.0037 nm, which makes electron microscopy superior to optical microscopy in materials characterization. In addition to optical observation of the thin film, scanning electron microscopy (SEM) was used in the present study. For a better understanding, a brief description of SEM is given in the following.

8.1.1 Scanning Electron Microscopy

Scanning electron microscopy (SEM) is a characterization technique where a high-energy electron beam is scanned across the surface to produce a high-resolution image of the sample surface. In case of a typical SEM, electrons emitted from a cathode filament are extracted and accelerated with an energy ranging from a few keV to 100 keV. The electrons are then focused

into a beam with a spot size of a few nanometers and scanned in a raster fashion across the area of interest on the sample surface. Electrons interact with sample surface though scattering events. Low energy (<50 eV) secondary electrons generated from the sample are collected and detected by a scintillator-photomultiplier which converts the electron energy into light then back into electrical signal to produce an ordinary SEM digital image. The detector is positively biased to attract the low energy secondary electrons. Since a steeper surface will emit a higher number of secondary electrons, a SEM image has three dimensional effects with a very high resolution (1 nm or less are possible).

During beam-sample interactions some electrons elastically scatter backward or reflect and are detected with an Everhart-Thornley detector [Everhart and Thornley, 1960]. The energies of the backscattered electrons are usually high and are sensitive to the atomic number of the target elements. Images are generated in the similar fashion with the aid of a scintillator. Bright areas in the image represent the location of heavier elements. An annular type detector can be used to improve the resolution by detecting electrons scattered through larger angles. The detector is negatively biased which repels low energy secondary electrons thereby only backscattered electrons are detected. Goldstein *et al.* [2003] provides a good reference for further study on SEM.

Even though the resolution is somewhat limited compared to transmission electron microscopy (TEM) (which is a competitive technique of thin film analysis), SEM possesses a number of advantages. Sample preparation for the SEM is relatively easy, which reduces the overall sample analysis time significantly. SEM can also be used to image a comparatively large area of the sample for compositional and morphological variation. Even though TEM has some advantages, it poses some specific disadvantages, e.g., sample preparation is especially a tedious

process which makes this TEM analysis very time consuming. Moreover, sample preparation, including thinning, can destroy or change the structural properties of the sample to be analyzed. Since a tiny part of a system is used and magnified to analyze in the nanoscale, the outcome of the analysis might not represent the entire sample. Nevertheless, the merit of a characterization technique depends upon specific applications and requirements as determined by the research project. SEM sample analysis was performed at the Samuel Roberts Noble Electron Microscopy Laboratory of the University of Oklahoma.

8.2 Results and Discussion

Microscopic analysis was performed with the help of Homer L. Dodge Department of Physics and Astronomy of the University of Oklahoma. In general, the samples analyzed could be divided into two categories, e.g., a highly-enriched Ge-rich film on SiO_2 layer either (*i*) exposed by HF etching or (*ii*) with the thermal oxide cap. Category (*i*) samples were used to investigate the surface morphology and compositional distribution, whereas type (*ii*) samples were cleaved for cross-sectional analysis.

Figure 8.1 represents a sample with type (*i*) with Ge_xSi_{1-x} (x =1) exposed so that the surface morphology of the Ge-rich layer is revealed. From the plane-view SEM image, it can be inferred that the surface of the synthesized Ge layer is very smooth. A side-by-side comparison of the compositional-sensitive, backscattered electron images indicates no compositional variations. Therefore, the surface morphology is consistent with a smooth thin-film without compositional variations.

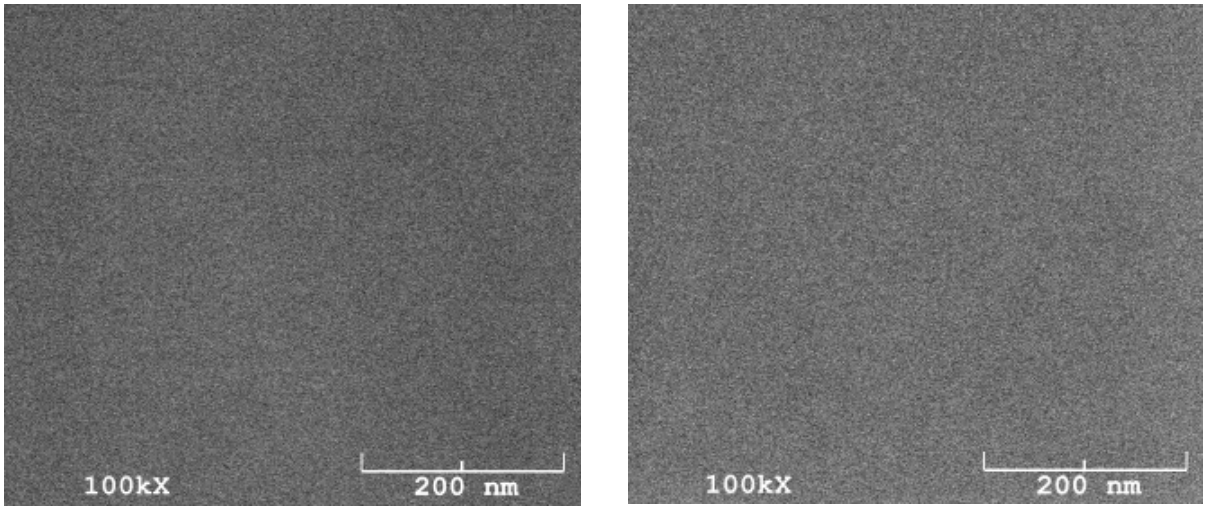

(*a*) Ordinary SEM Image

(*b*) Backscattered EM Image
(Composition sensitive)

Remarks: No compositional variation

Fig. 8.1: Plane-view SEM images of the Ge-rich layer.

Figure 8.2 shows cross-sectional images from a type (*ii*) sample, where the $SiO_2/Ge_xSi_{1-x}/SiO_2/Si$ interfaces are visible. Magnified, cross-sectional SEM images of the interfacial region are also

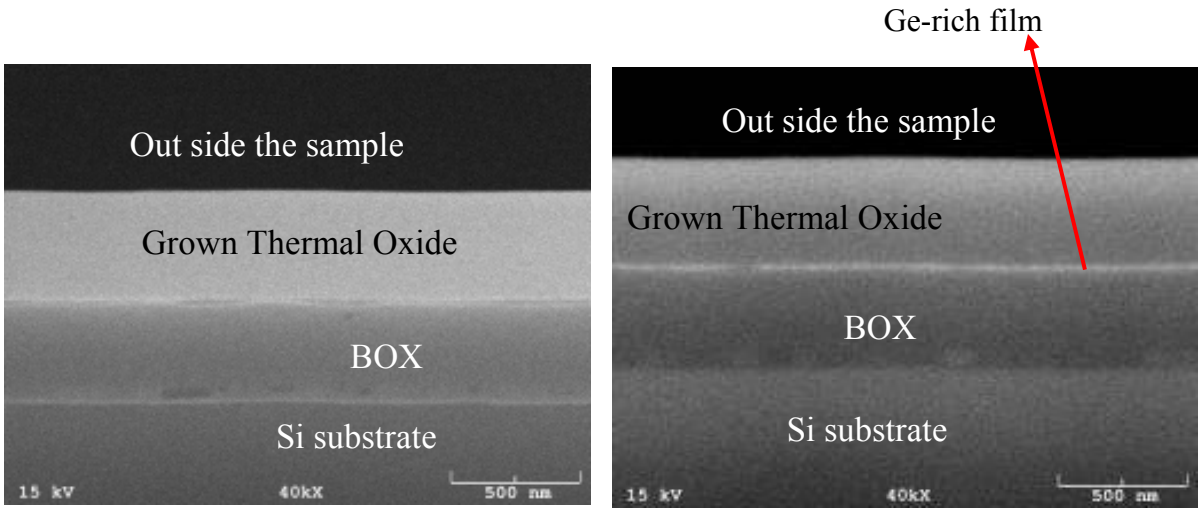

Ordinary SEM Image

Backscattered EM Image (BEM)
(Composition sensitive)

Fig. 8.2: Cross sectional SEM images showing $SiO_2/Ge_xSi_{1-x}/SiO_2$ /Si interfaces. BEM image shows that Ge is harvested at the thermal oxide-BOX interface by thermal oxidation.

shown in Figure 8.3. Each SEM image is accompanied by a composition-sensitive backscattered electron microscopy (BEM) image. The last set of images was resolved with higher magnification. Each of the cross-sectional SEM images indicates that the various interfaces are atomically sharp and planar.

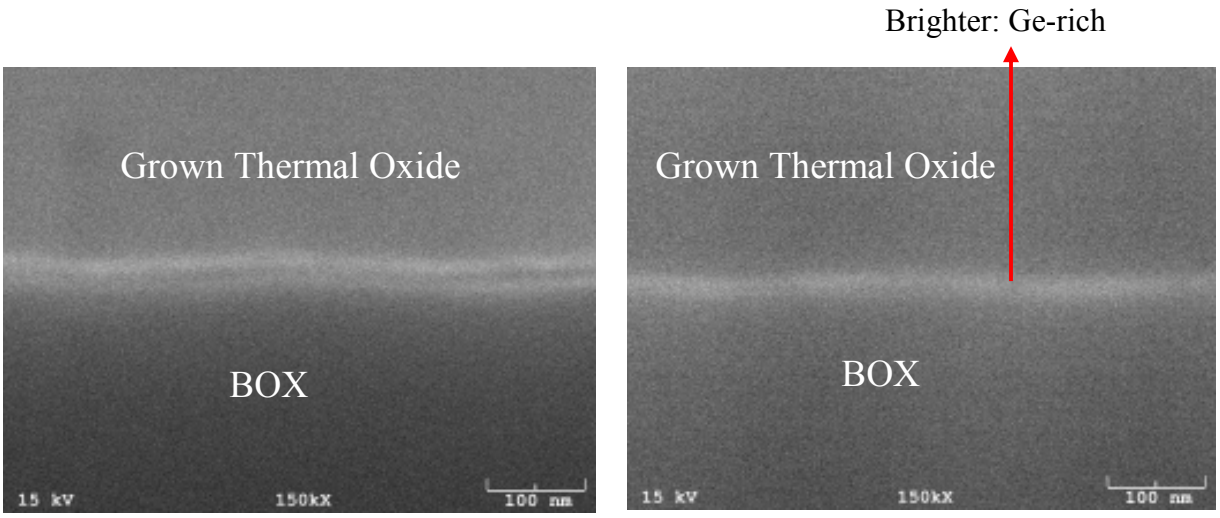

Ordinary SEM Image

Backscattered EM Image
(Composition sensitive)

Fig. 8.3: Cross sectional SEM images showing $SiO_2/Ge_xSi_{1-x}/SiO_2$ interfaces with higher magnification. Brighter line at thermal oxide-BOX interface represents Ge-rich layer.

Lastly, the undulation of the segregated thin film is investigated in Figure 8.4, where magnified cross sectional SEM is presented. This waviness is related to the BOX uniformity at the interface (between the top silicon layer and the buried oxide of SOI), at which the Ge_xSi_{1-x} thin film is segregated. In the figure, a slightly exaggerated zigzag line is superimposed on the image to delineate these undulations within the Ge film. This interfacial roughness of SIMOX has some positive effects on the thin film relaxation (the detail of which is discussed already in

the previous chapter) but at the same time limits the thinness to which a continuous Ge-on-insulator can be attained.

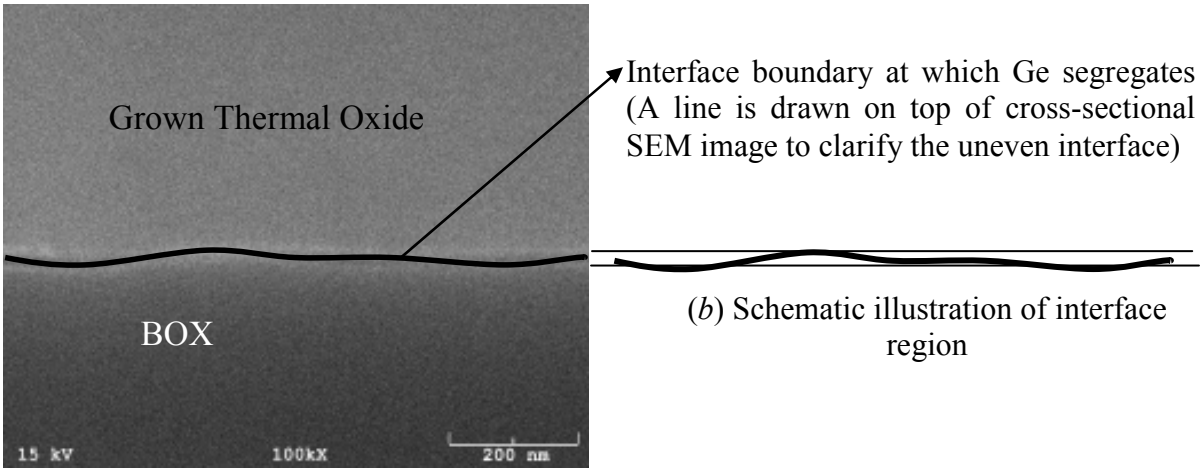

(*a*) Ordinary SEM image

(*b*) Schematic illustration of interface region

Fig. 8.4: Illustration of undulating (due to interfacial roughness of SIMOX.) continuous Ge film at the thermal oxide-BOX interface.

8.3 References

Everhart T.E., Thornley, R.F.M., J. Sci. Instrum. 37 (1960) 246

Goldstein, J. I., Newbury, D., Joy, D., Lyman, C., Echlin, P., Lifshin, E., Sawyer, L., Michael, J., *Scanning Electron Microscopy and X-Ray Microanalysis*, 3rd Edition, Springer, New York, (2003)

Williams, D.B., Carter, C.B., *Transmission Electron Microscopy Basic I*, Plenum Press, New York (1996)

CHAPTER 9

CONCLUSIONS

Results of an investigation into the thermal oxidation of Ge-implanted Si were presented in this thesis. Not only are the results significant in their own right, but they serve as the basis for development of a unique process of synthesizing a thin Ge_xSi_{1-x} film on SiO_2 for use as a compliant substrate for growing lattice mismatched films.

Thermal oxidation of a Ge-implanted Si wafer was shown to segregate the Ge at the growing interface into a distinct layer. This layer was commensurate with the underlying Si and formed pseudomorphically for an ion fluence $\leq 2\times10^{16}$ ions/cm^2 after which it relaxed by the formation of misfit dislocations. The composition of this GeSi layer depended upon the oxidation conditions ranging from nearly 100 % Ge for wet oxidation at 900 ˚C to 30 % Ge at 1050 ˚C. The presence of a high concentration of Ge at the growing interface was shown to significantly enhance the oxidation kinetics. In particular, this occurred only if the concentration of Ge was above ~80 %, but it also was shown to depend upon the thickness of the segregated film. This phenomenon was investigated over an implantation fluence ranging to 2×10^{17} ions/cm^2, and the oxidation kinetics were shown to increase over the entire fluence range. Thus, it was clearly demonstrated that the strain state of the segregated film was not related to the enhancement effect. Also, the enhancement in the growth kinetics was shown to be a result of an increase in the reaction kinetics at the growth interface, which was correlated to the Ge−Ge bond energy. While it was readily shown that the enhancement occurred during wet oxidation, oxidation under dry conditions was, for the first time, demonstrated. The activation energy of

the interfacial reaction was measured under both wet and dry conditions and shown to be the same, indicating a common mechanism for enhanced oxidation.

The oxidation results are summarized as follows:

i. Implanted Ge in Si is totally rejected by the growing thermal oxides during both dry and wet oxidation conditions.

ii. The concentration of the Ge-rich layer at the interface depends on the kinetic competition between the growth of oxides and the diffusion of Ge into silicon.

iii. At or above a critical concentration (~80 % Ge within a monolayer), the interfacial reaction is increased by a fluence-independent factor. This corresponds to the concentration at which the film becomes more Ge-like.

iv. Interfacial oxidation reaction was modified by the presence of Ge and was enhanced due to the weaker Ge−Ge and Ge−Si bonds than that of Si−Si.

v. Oxidation of Ge^{+}-implanted silicon can also be modeled as "Deal and Grove" and can be used for computer simulation.

vi. Ge segregation produces a "snow-plow" effect that forms an enriched Ge layer at the Si/SiO_2 interface and enhances the oxidation kinetics in wet and in dry ambient under appropriate conditions.

A methodology for forming a compliant substrate based upon a thin Ge film on a visco-elastic oxide was also presented. The process steps involve the oxidation of a Ge-ion implanted SOI wafer formed by a SIMOX technique followed by thermal oxidation. Application of these steps was shown to result in the desired heterostructure, i.e. $Ge/SiO_2/Si$. Process sensitivity was identified near the point during oxidation where all of the Si within the device layer of the SOI is

consumed. Without any underlying Si, the encapsulated Ge layer can be volatilized by the following reaction:

$$GeO_2 + Si \rightarrow SiO_2 + Ge, \quad \text{followed by} \qquad \frac{1}{2} GeO_2 + \frac{1}{2} Ge \rightarrow GeO\ (s)$$

Solid germanium monoxide (GeO(s)) is volatile and is easily evaporated in its gaseous form (GeO(g)). It was shown that this effect could be beneficial since Ge loss may be responsible for strain relaxation within the film. Alternatively, it was suggested that the relaxation could also happen due to surface roughening. Such roughening can, sometimes, lead to the formation of pinholes within the film at longer oxidation times.

Thus, a process was demonstrated for forming a partially relaxed Ge film on oxide for consideration as a compliant substrate. More work is needed to better understand the relaxation process, as well as the film roughening. However, the process is sufficiently developed to provide wafers to evaluate its potential as a compliant substrate.

APPENDIX

DEAL AND GROVE OXIDATION MODEL

During oxidation of silicon, oxidants (O_2 and/or H_2O) are transported in the gaseous phase to the silicon surface where they are absorbed and diffuse through the growing oxide layer to meet fresh silicon. The process (as illustrated with Figure A1) involves the three distinct steps [Deal and Grove, 1965] represented by the following flux equations:

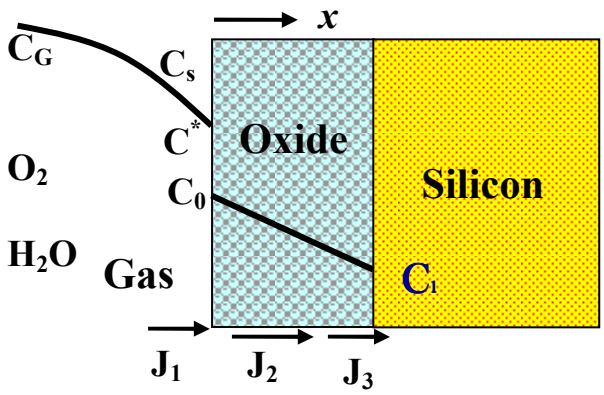

Fig. A1: Model for oxidation of silicon.

(a) Gas phase transport:

$$J_1 = h\left(C^* - C_0\right) \ldots\ldots \text{(A.1)}$$

where J_1 is the gas phase flux of oxidant from gaseous phase to solid surface vicinity, h is the gas-phase transport coefficient, C_0 and C_s are the concentration of the oxidant at the outer surface of oxide and in the gas phase respectfully. At $J_1 = 0$, $C_0 = C^*$ where C^* is the equilibrium concentration of oxidants in absence of their transport through the surface.

(b) Diffusion through oxides:

$$J_2 = -D\frac{\partial C}{\partial x} \cong D\frac{\left(C_0 - C_1\right)}{x} \ldots\ldots\ldots \text{(A.2)}$$

which is Fick's law [Fick, 1855] with an effective diffusion coefficient D. The thickness of the growing oxide layer is expressed by x, the concentration gradient of oxidants across the oxide

layer by $\frac{\partial C}{\partial x}$ (assuming steady state diffusion and a linear gradient in the oxidant concentration), and the concentration of oxidant near the silicon-oxide interface is given by C_1.

(c) Reaction rate at the oxide-silicon interface:

$$J_3 = kC_1 \ldots\ldots\ldots \text{(A.3)}$$

where k is the reaction rate constant of a first order flux relation. Complete reaction of all oxidants arriving at the interface is assumed.

At steady state (and (when $J_1 \neq 0$), the flux through the sample is expressed as

$$J_1 = J_2 = J_3$$

$$\Rightarrow h\left(C^* - C_0\right) = D\frac{\left(C_0 - C_1\right)}{x} = kC_1 \ldots\ldots\ldots \text{(A.4)}$$

To relate the oxidation rate from the flux of oxidant from the ambient, we need to solve for C_0 and C_1.

Starting from $J_1 = J_2$, i.e., from the Equation (A.4)

$$h\left(C^* - C_0\right) = D\frac{\left(C_0 - C_1\right)}{x}$$

$$\Rightarrow C^* - C_0 = \frac{D}{xh}C_0 - \frac{D}{xh}C_1$$

$$\Rightarrow \frac{D}{xh}C_1 = \frac{D}{xh}C_0 + C_0 - C^*$$

$$\Rightarrow C_1 = C_0 + \frac{xh}{D}C_0 - \frac{xh}{D}C^* \ldots\ldots\ldots \text{(A.5)}$$

Now, putting this value of C_1 into the second part, i.e. $J_2 = J_3$ we get,

$$D\frac{\left(C_0 - C_0 - \frac{xh}{D}C_0 + \frac{xh}{D}C^*\right)}{x} = k\left(C_0 + \frac{xh}{D}C_0 - \frac{xh}{D}C^*\right)$$

$$\Rightarrow -hC_0 + hC^* = kC_0 + \frac{kxh}{D}C_0 - \frac{kxh}{D}C^*$$

$$\Rightarrow C_0\left(h + k + \frac{khx}{D}\right) = C^*\left(h + \frac{kxh}{D}\right)$$

$$\Rightarrow C_0 = C^*\left(\frac{h + \frac{kxh}{D}}{h + k + \frac{kxh}{D}}\right) = C^*\left(\frac{1 + {kx}/{D}}{1 + {k}/{h} + {kx}/{D}}\right) \ldots\ldots\ldots \text{(A.6)}$$

Similarly we get,

$$C_1 = C^*\left(\frac{1}{1 + {k}/{h} + {kx}/{D}}\right) \ldots\ldots\ldots \text{(A.7)}$$

In a diffusion controlled process when ${D}/{kx} \to 0$, $C_1 \to 0$ and $C_0 \to C^*$ and the flux of the process can be written as,

$$J_1 = J_2 = J_3 = J = \frac{kC^*}{1 + {k}/{h} + {kx}/{D}} \ldots\ldots\ldots \text{(A.8)}$$

Now, the growth rate of oxide film, dx/dt can be describe by the following equation,

$$\frac{dx}{dt} = \frac{J}{N} \ldots\ldots\ldots \text{(A.9)}$$

where N is the number of oxidant molecule associated with unit volume of oxide film.

$$\Rightarrow \frac{dx}{dt} = \frac{{kC^*}/{N}}{1 + {k}/{h} + {kx}/{D}}$$

$$\Rightarrow dx + {k}/{h}\,dx + {k}/{D}\,xdx = {kC^*}/{N}\,dt \ldots\ldots\ldots \text{(A.10)}$$

To get the solution, the above equation must be integrated with following boundary condition:

At $t = 0,\ x = x_i$ (i.e., x_i is the thickness of the pre-existing oxide layer and oxidation starts with the diffusion of oxidants through the oxide layer to be consumed at the silicon-oxide interface)

$$\Rightarrow \int_{x_i}^{x} \left(1 + k/h + k/D\, x\right) dx = \int_0^t \left(kC^*/N\right) dt$$

$$\Rightarrow \left[x + k/h\, x + k/D \frac{x^2}{2} \right]_{x_i}^{x} = \left[\frac{kC^*}{N} t \right]_0^t$$

$$\Rightarrow x^2 + 2D\left(1/k + 1/h\right)x = 2DC^*/N\, t + x_i^{\,2} + 2D\left(1/k + 1/h\right)x_i$$

$$\text{Let, } 2D\left(1/k + 1/h\right) \equiv A \text{ and } 2DC^*/N \equiv B$$

$$\Rightarrow x^2 + Ax = Bt + x_i^{\,2} + Ax_i \ldots\ldots\ldots \text{(A.11)}$$

$$\Rightarrow \frac{x^2 - x_i^{\,2}}{B} + \frac{x - x_i}{B/A} = t \ldots\ldots\ldots \text{(A.12)}$$

where, $B = \dfrac{2DC^*}{N}$ is the parabolic rate constant and $\dfrac{B}{A} = \dfrac{C^*}{N\left(1/k + 1/h\right)} \cong \dfrac{C^* k}{N}$ is the linear rate constant.

$$\Rightarrow x^2 + Ax = B\left(t + \frac{x_i^{\,2} + Ax_i}{B} \right)$$

$$\Rightarrow x^2 + Ax = B\left(t + \tau\right) \ldots\ldots\ldots \text{(A.13)}$$

letting $\dfrac{x_i^{\,2} + Ax_i}{B} \equiv \tau$, which is the shift in time coordinate in oxidation kinetics due to the pre-existing oxide layer.

Now, taking only the positive solution (since there is no possibility of having negative oxide layer thickness) of the above quadratic equation we can write the oxide thickness as a function of oxidation time as:

$$\Rightarrow x = \frac{-A + \sqrt{A^2 + 4B(t+\tau)}}{2} = -\frac{A}{2} + \frac{\sqrt{A^2 + 4B(t+\tau)}}{2}$$

$$= -\frac{A}{2} + \sqrt{\frac{A^2 + 4B(t+\tau)}{4}} = \sqrt{\left(\frac{A^2}{4} + B(t+\tau)\right)} - \frac{A}{2}$$

$$= \sqrt{\left(\frac{A^2}{4}\left(1 + \frac{4B(t+\tau)}{A^2}\right)\right)} - \frac{A}{2} = \frac{A}{2}\sqrt{\left(1 + \frac{4B(t+\tau)}{A^2}\right)} - \frac{A}{2}$$

$$= \frac{A}{2}\left[\sqrt{\left(\frac{A^2 + 4B(t+\tau)}{4B}\frac{4B}{A^2}\right)} - 1\right] = \frac{A}{2}\left[\sqrt{\left(\frac{\frac{A^2}{4B} + (t+\tau)}{A^2/4B}\right)} - 1\right] = \frac{A}{2}\left[\sqrt{\left(1 + \frac{t+\tau}{A^2/4B}\right)} - 1\right]$$

$$\Rightarrow x = \frac{A}{2}\left\{\sqrt{\left(1 + \frac{t+\tau}{A^2/4B}\right)} - 1\right\} \ldots\ldots\ldots \text{(A.14)}$$

Now, lets consider two limiting cases:

During the early stages of oxidation with smaller oxidation time, i.e., $t << A^2/4B$ where $kx/D << 1$ (the situation is schematically illustrated with Figure A2(*a*)) the Equation (A.14) reduces to;

$$\Rightarrow x \cong \frac{B}{A}(t+\tau) \ldots\ldots\ldots \text{(A.15)}$$

So, the general relation between oxide thickness, x, and oxidation time, t, reduces to a linear relation. The combined constant B/A can thereby be referred as *linear* rate constant.

For longer oxidation times, i.e., $t >> A^2/4B$ and also $t >> \tau$, where $kx/D >> 1$, (the situation is schematically illustrated with Figure A2 (*b*)),

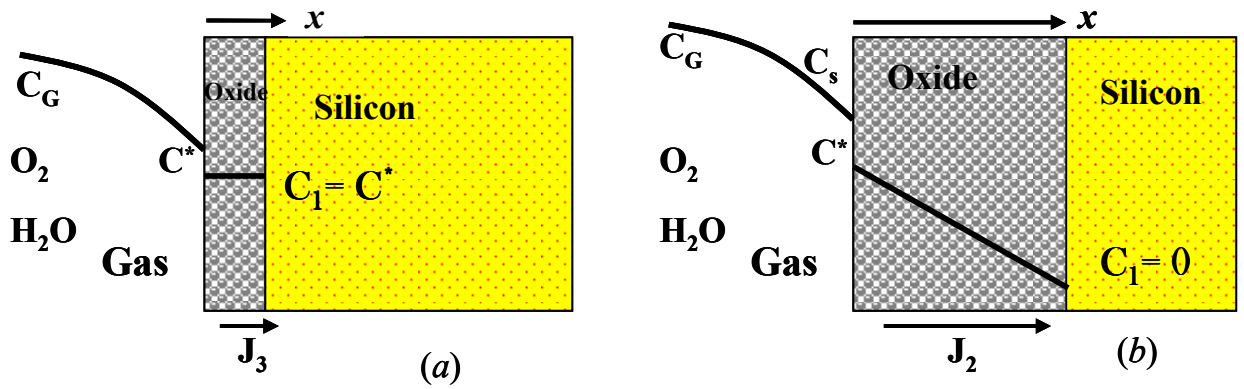

Fig. A2: Oxidation model illustrating two extreme cases; (*a*) linear (*b*) parabolic.

$$\Rightarrow x \cong \frac{A}{2}\left(\frac{t}{A^2/4B}\right)^{1/2}$$

$$\Rightarrow x^2 \cong Bt \ldots\ldots\ldots \text{(A.16)}$$

So, the general relation between oxide thickness, x, and oxidation time, t, reduces to a parabolic relation. The constant B can thereby be referred as *parabolic* rate constant.

Reference

Deal, B.E., Grove, A. S., J. Appl. Phys. **36** (1965) 3770

Fick, A., *Phil. Mag.* **10** (1855) 30